MAGNETIC RESONANCE ELASTOGRAPHY AND NONLINEAR INVERSION PROBLEM IN THE AGING BRAIN

BY

AARON THOMAS ANDERSON

DISSERTATION

Submitted in partial fulfillment of the requirements
for the degree of Doctor of Philosophy in Theoretical and Applied Mechanics
in the Graduate College of the
University of Illinois at Urbana-Champaign, 2018

Urbana, Illinois

Doctoral Committee:

Professor John G. Georgiadis, Chair & Director of Research
Associate Professor Elijah E.W. Van Houten, Université de Sherbrooke
Professor M. Taher A. Saif
Professor Michael Insana

Abstract

The history of medical imaging has centered on finding correlations between contrast in an image and diagnosis of a disease, but there is a shift in medical imaging from contrast towards quantitative measurements as disease biomarkers. Magnetic resonance elastography (MRE) is a non-invasive imaging technique created, and being developed, based on modeling of mechanical properties of biological tissue. For example, the combination of state-of-the-art MR imaging and finite element based nonlinear inversion (NLI) for estimation of viscoelastic material properties have shown NLI-MRE's impressive ability to capture subtle correlations between memory performance and stiffness in grey matter regions. These discoveries are made possible by the rapid and extensive development of the underlying methods for the MR displacement imaging and the mechanical property estimation within the last few years.

Within the MRE field, there are a number of open questions about the true *in vivo* material property values and how inaccurate current MRE methods are from actual values. The work in this dissertation attempts to address these fundamental questions through a comprehensive study of estimation parameters for NLI, optimizing for un-biased parameters, and proposing quality metrics for evaluating the confidence of final estimates. Additionally, the issue of model-data-mismatch for the isotropic material model assumption when reconstructing anisotropic tissue was investigated by subjecting the *in vivo* tissue to distinctly different excitation patterns, which elucidated the necessity of incorporating an anisotropic material model into NLI. Finally, the improvements in inversion techniques and new multi-excitation experiments were implemented in an *in vivo* study of aged human subjects to investigate how age affects anisotropic properties of the brain. MRE shows promise for being more sen-

sitive to the normal effects of aging than the more widely utilized MR imaging techniques, specifically diffusion tensor imaging (DTI). Since DTI models the diffusion of free water in the tissue and MRE models material properties, MRE and DTI will likely be incorporated for a more comprehensive description than either alone. Thorough characterization of the MRE processes and improvements in methods will benefit future opportunities for applying MRE in the new frontier of quantitative imaging.

For my parents, you gave me the foundation for becoming a lifelong learner.

For my son, you motivate me to use this knowledge to help others.

For my wife, without your love and support none of this would have been possible.

Acknowledgments

Growing up in a small town in Northern Wisconsin, my childhood was a literal expression of the proverb "it takes a village to raise a child." My graduate school development was a similar experience except the "village" crossed international boundaries. My area of research was truly an interdisciplinary effort because multiple people were involved throughout the entire process of hypothesis, experimental design, method development, analysis, and interpretation; thus, it required a wide-range of people and expertise.

The primary "community leaders" of my "academic village" were my advisors, Dr. John Georgiadis and Dr. Elijah Van Houten (Université de Sherbrooke). First, I would like to thank Professor Georgiadis for providing the opportunity to study and develop the field of MR Elastography. From our first meeting and every meeting since, Professor Georgiadis has had an inquisitive and infectious interest in understanding the form and function of the human body in terms of mechanics, physiology, history, and philosophy. Second, thank you to Professor Elijah Van Houten, who was gracious enough to include me in the development of the nonlinear inversion method used in MRE. Our meetings were always equal parts discussion on current results and looking forward to new areas of research.

In a less official, but no less important role, I cannot thank Dr. Curtis Johnson enough for his early introduction and guidance into MR imaging, elastography, and the community of MRE. I have benefited greatly from discussions about the small details of improving MRE experiments up through the philosophical directions of the field.

Thank you to Dr. Bradley Sutton and the members, past and present, of the Magnetic Resonance Functional Imaging Lab (MRFIL) who have been an integral part of the "MR"

in MRE. Every member has helped with running experiments and been extremely patient with my, often novice and simple, MR questions, including: Dr. Joseph Holtrop, Dr. Giang Chau Ngo, Alex Cerjanic, Meltem Uyanik, Dr. Xi Peng, and Natalie Aw. With a special thank you to Alex Cerjanic, who provides both encouragement and healthy doses of reality to my sometimes naively optimistic ideas.

The always helpful and professional staff of the Biomedical Imaging Center (BIC), at the Beckman Institute for Advanced Science and Technology, have been invaluable with developing MRE experimental protocols and executing studies, including: Dr. Tracey Wszalek, Shelly Yambert, Tracy Henigman, Nancy Dodge, Holly Tracy, and Dr. Ryan Larsen.

Other members of my international village include: Dr. Neal Cohen, Dr. Hillary Schwarb, Lela DiMonte, Noel Naughton (University of Illinois at Urbana-Champaign), Dr. Keith Paulsen, Dr. Matthew McGarry, Ligin Solamen (Dartmouth College), Nicolas Gallo, Dr. Boris Gutman (Illinois Institute of Technology), Dr. Graham Huesmann (Carle Foundation Hospital), Dr. Assimina Pelegri, Daniel Sullivan (Rutgers University), and Dr. Lucy Hiscox (University of Edinburgh).

To my doctoral committee members, Dr. John Georgiadis, Dr. Elijah Van Houten, Dr. Taher Saif, and Dr. Michael Insana, I appreciate your time and constructive feedback on this research.

Thank you to my funding sources who have made my research possible, including a teaching assistantship from the MechSE department and research assistantship from NSF grant CMMI-1437113. Significant computational resources were provided by Blue Waters sustained-petascale computing project (supported by NSF awards OCI-0725070 and ACI-1238993, and the state of Illinois), and the supercomputer Mammouth parallèle 2 from the Université de Sherbrooke, managed by Calcul Québec and Compute Canada (supported by Canada Foundation for Innovation, NanoQuébec, RMGA and the Fonds de recherche du Québec - Nature et technologies).

Table of Contents

List of Tables

List of Figures

List of Abbreviations

AP	Anterior-Posterior excitation
BCs	Boundary Conditions
CC	Corpus Callosum
CG	Conjugate Gradient
CR	Corona Radiata
DTI	Diffusion Tensor Imaging
FOV	Field Of View
GM	Grey Matter (brain)
HPC	High-Performance Computing
LR	Left-Right excitation
MPRAGE	T1-weighted MR image
MRE	Magnetic Resonance Elastography
MRI	Magnetic Resonance Imaging
NLI	Nonlinear Inversion
OSS-SNR	Octahedral Shear Strain Signal-to-Noise Ratio
ROI	Region of Interest
SLF	Superior Longitudinal Fasciculus
SS	Simple Shear
WM	White Matter (brain)

List of Symbols

μ	Lamé's second material modulus
G^*	Complex equivalent of μ
G'	Storage modulus ($\Re\{G^*\}$)
G''	Loss modulus ($\Im\{G^*\}$)
λ	Lamé's first material modulus
L_s	Shear wavelength
L_L	Longitudinal wavelength
μ_{stiff}	Dynamic stiffness
N_{CG}	Conjugate Gradient iterations
N_g	Global NLI iterations
ϕ	Cost function for NLI
ρ	Material density
$\mathbf{u}_c$	Forward finite-element calculated displacement
$\mathbf{u}_m$	MRI measured displacement
ξ	Damping ratio
$\varepsilon_{\parallel/\perp}$	DTI-based strain ratio

Chapter 1

Introduction

1.1 Background and Significance

Mechanical Properties as Biomarkers In medical practice, palpation is a technique physicians use on a daily basis when assessing the physical health of a patient as a potential indicator of disease, known as "biomarkers" [1]. The most widely accepted definition of a "biomarker" is "a characteristic that is objectively measured and evaluated as an indicator of normal biological processes, pathogenic processes, or pharmacologic responses to a therapeutic intervention" [1, 2]. Biomarkers are not the root cause of the ailment or disease but rather an observable signal from the disease. Not coincidentally, the goal when inventing and developing magnetic resonance elastography (MRE) by physicians and researchers at Mayo Clinic was to quantify and identify clinically useful biomarkers [3, 4]. The seemingly simple but pioneering work of a controlled external palpation to quantify the stiffness of a patient's tissue has gone on to become a clinical standard for staging some important hepatic diseases. For example, non-alcoholic fatty liver disease (NAFLD) causes excess fat deposits at the cellular level, which in turn changes the macroscale stiffness of the tissue [5]. Hepatic MRE replaced focal invasive biopsies with spatial maps and opened a larger area of research into mechanical biomarkers in other organs as a promising sensitive and specific diagnostic technique. For example, MRE has the capability to capture a number of diseases affecting the microstructure of the human brain, including: multiple sclerosis, normal- and low-pressure hydrocephalus, Alzheimers disease, and cancer [6–12].

In an organ like the human brain, the composition and behavior of the tissue is more

complex than the liver due to its hierarchical microstructure and heterogeneous mechanical, chemical, and electrical characteristics of the cellular constituents. Comprising 50% of the brain, the highly-ordered white matter (WM) regions are composed of myelinated axons embedded in a support matrix of glial cells (oligodendrocytes and astrocytes) and extracellular space (macromolecules and interstitial fluid). For MRE to probe the brain WM, one has to interpret the MRE metrics in terms of the interaction between axons and glial matrix as well as their intrinsic properties. The macroscopic effective properties of the tissue, on the voxel-size length scale available to MRE, are then influenced by the integrity of the axons (e.g. demyelination or inflammation) and the mechanical connection and intrinsic properties of the supporting cells. The challenge in MRE, if one hopes to discern subtle differences from neurodegenerative diseases, is contingent on both improved MR imaging, higher resolution and signal-to-noise ratio (SNR), and accurate and reliable material property reconstructions from the nonlinear inversion (NLI) estimation.

Aims of Proposed Research Many studies have shown NLI-MRE mechanical properties of the brain are sensitive to subtle differences in healthy individuals' sub-cortical grey matter [13], performance on memory tasks [14, 15], fitness intervention in subjects with Multiple Sclerosis (MS) [16] and in diseases, including: hydrocephalus, epilepsy, and tumors [8]. All of the aforementioned stiffness biomarkers were made possible through increased coverage and spatial resolution of MR imaging, and development of more robust and accurate material property estimation algorithms. The greatest opportunity for utilizing higher-resolution MRE imaging will come from characterizing the tissue's response to external stimulation and material models well matched to the underlying microstructure of the human brain. Although there are groups implementing anisotropic models ranging from transversely isotropic models [17–21] to fully orthotropic [22, 23], all of them rely on significant modeling assumptions, smoothing of displacement fields, and/or directional filtering of displacement fields to simplify the analysis. The overarching aim of this research project is to take advantage of

the proven finite-element heterogeneous, isotropic nonlinear inversion (NLI) to probe healthy aging while looking for opportunities for improved understanding of the algorithm's behavior with a view towards areas for possible improvement.

This project is driven by two aims. First, improving the overall accuracy and reliability of the NLI-MRE framework through a systematic characterization of the effects of inversion parameters on reconstructed material properties. We seek to develop convergence thresholds for ensuring the quality of final statistics. Additionally, a multi-excitation MRE experiment on a healthy subject has shown the potential cost of missing the complex material behavior and the opportunity for anisotropic models to capture new biomarkers. Second, we explore the behavior of NLI derived MRE metrics by employing two excitation directions under the hypothesis that the brain is described by a transversely isotropic model. The isotropic NLI-MRE framework has shown the ability to capture subtle differences in healthy humans, so we apply this approach to identify differences between young and old in healthy human brains. Taken together, these aims will help characterize the mechanical properties of the brain in a robust, repeatable, and quantitative way by systematic quantification of sources of error towards improved sensitivity and specificity, while decreasing overall experimental variance.

1.1.1 Material Property Reconstruction

Each of the individual displacement fields from MRE imaging were reconstructed into full brain material property maps using, as mentioned above, the finite element based nonlinear inversion algorithm (NLI) [24–27]. NLI is based on an *a priori* model for mechanical tissue behavior, which in this case is a heterogeneous, isotropic, viscoelastic material model. This is governed by Navier's equation of the form

$$\nabla \cdot (\mu(\nabla \tilde{\mathbf{u}} + \nabla \tilde{\mathbf{u}}^T)) + \nabla(\lambda \nabla \cdot \tilde{\mathbf{u}}) = \rho \frac{\partial^2 \tilde{\mathbf{u}}}{\partial t^2}, \tag{1.1}$$

where $\tilde{\mathbf{u}}$ is the 3D displacement field, λ and μ are Lamé's material constants, ρ is the density, and ∇ is the gradient operator. Given the tissue under investigation is highly-saturated, the density is assumed to be imperceptibly near water to fix the value at 1000 kg/m^3, and the Poisson's ratio is assumed to be very close to 0.5, with a value of lambda chosen for reasonable stability at $\lambda = 1.6489 \times 10^6$ Pa [28]. The complex displacement field is assumed to be at a steady-state of the form $\tilde{\mathbf{u}}(x, y, z, t) = \mathbf{u}(x, y, z) \exp(i\omega t)$ (where $\mathbf{u}(x, y, z)$ is complex), and the governing equation, Eq. (1.1), then simplifies to

$$\nabla \cdot (\mu(\nabla \mathbf{u} + \nabla \mathbf{u}^T)) + \nabla(\lambda \nabla \cdot \mathbf{u}) = -\rho\omega^2 \mathbf{u}. \tag{1.2}$$

For the nearly incompressible problem where $\nabla \cdot u \to 0$ and $\lambda \to \infty$ the second term on LHS becomes singular. The problem becomes numerically unstable due to $\lambda \gg \mu$. A remedy is to introduce pressure (p) as a Lagrange multiplier and the system of equations becomes

$$\begin{cases} \nabla \cdot \mu \nabla u + \nabla \left(\mu \nabla \cdot u - p\right) = -\omega^2 \rho u & \text{in } \Omega, \\ K \operatorname{tr}(\varepsilon) = -p & \text{in } \Omega, \\ u = u_0 & \text{on } \Gamma_u, \\ n \cdot \sigma_E = f_0 & \text{on } \Gamma_\sigma \end{cases} \tag{1.3}$$

where Ω is the entire region and Γ is the boundary of the region. NLI employs a finite element spatial discretization to compute an expected displacement field ($\mathbf{u}_c$) from an estimate of the material properties ($\theta = [G', G'']$). This is then compared to the measured displacement field ($\mathbf{u}_m$), and the material property estimation is iteratively updated in order to minimize a mean-squared error cost function

$$\phi = \sum_{\Omega} ||\mathbf{u}_c(\theta) - \mathbf{u}_m||^2 \tag{1.4}$$

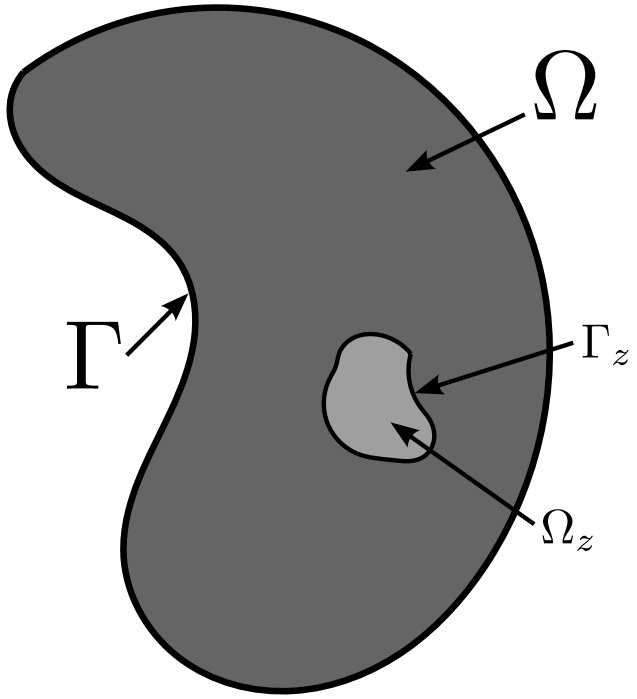

Figure 1.1: Schematic of the subzone (Ω_z, light grey) as a subset of the entire domain with Dirichlet boundary conditions (Γ_z) from the measured displacement field.

where the summation is over the physical domain of interest, Ω. To reduce the overall computational costs, minimization of Eq. (1.4) is reformatted in parallel as sub-domains, known as "subzones", of the full physical domain, Ω, shown schematically in Figure 1.1.

As noted above, the NLI algorithm estimates the shear modulus (μ, complex number) with two of the assumptions being fixed: density (1000 kg/m^3) and lambda modulus ($\lambda = 1.6489 \times 10^6$ Pa). The density is commonly left to be at or near water because the tissue is well hydrated, a major reason MRI is so applicable, and any deviation away is not discernible. Comparing the shear and bulk moduli can be understood by looking at the two waves present in the system: shear and longitudinal waves. The shear wavelength is defined as

$$L_s = \frac{1}{f}\sqrt{\frac{\Re\{\mu\}}{\rho}} \tag{1.5}$$

and the longitudinal wavelength as

$$L_L = \frac{1}{f}\sqrt{\frac{\lambda + 2\mu}{\rho}}, \tag{1.6}$$

where f is the frequency of applied excitation. For tissue, the longitudinal wavelength will be much, much longer than the shear wavelength. Relative to the domain of the human brain, the width/length of the brain is about $2{-}3\times$ L_s whereas the longitudinal wave is about $25\times$ longer. There is some evidence it is still worth the effort of reconstructing the complex bulk modulus as a way to account for the compressive damping of the system, not just viscoelastic damping [26, 29]. The NLI framework does have the capability to assume both μ and λ are unknown, and it will reconstruct material maps for each, real- or complex-valued.

Subzone Decomposition of Domain

The decomposition of the full brain estimation problem into smaller, more tractable problems started out as a practical computational necessity given the hardware but had the side benefit of reducing the dependence on, inherently noisy, MR measured displacement data [24]. The number of nodes within a typical human brain subject, assuming 2 mm isotropic voxel resolution, is on the order of $200,000$ nodes. Although there have been significant computational hardware advances in the last fifteen years, the forward finite element problem on this scale is still quite large, in terms of memory and computation time. Current high performance computing (HPC) systems are capable of computing a full-domain finite element (FE) forward solution (on the order of 1-2 days on state-of-the-art HPC); however, the NLI algorithms require forward and adjoint calculations to be run hundreds of times before convergence is reached. The decomposition of the full problem into small sub-problems, or "subzones," comes with the benefit of decreased dependence on measured data for two reasons, compared with other estimation methods for MRE: the forward finite element calculation only uses the measured displacement for Dirichlet boundary conditions,

and the cost function, Eq. 1.4, indirectly influences new property estimates. In contrast, direct algebraic methods, common in the field of MRE, use all of the measured displacement fields directly in estimating the material properties, thus these methods are directly dependent on high-quality measured data. The methods either require computing the curl of the field (i.e. remove divergence), which amplifies the noise, and/or heavily filtering the data from any source of noise, which smooths property maps.

The major assumption underlying the method of domain decomposition is the sum of minimizing the error at the subzone-level is equivalent to minimizing the error across the whole domain:

$$\min_{\theta}(\phi) = \min_{\theta_z}\left(\sum_{z=1}^{Q}\phi_z\right) \implies \sum_{z=1}^{Q}\min_{\theta_z}(\phi_z), \tag{1.7}$$

where Q is the set of subzones and ϕ_z is the cost function error. The result of the reconstruction is a spatial map of the complex shear modulus μ.

Conjugate Gradient Estimation

All of the material property estimation occurs at the subzone-level and the estimator framework has the flexibility to use one or a combination of methods. NLI initially used the Gauss-Newton method (GN) and has since incorporated nonlinear conjugate gradient (CG) and quasi-Newton (QN) methods. See the Tan et al. overview and evaluation of the material models (viscoelastic and poroelastic) and estimation methods available within the NLI framework for full details [30]. For background to work here, the CG method is the estimator chosen in this work, and for most NLI-MRE studies, because it has a super-linear convergence rate and relatively low memory requirement compared with the other methods. The nonlinear CG method is based on the steepest descent method and differs from the standard, linear CG method because the cost function, Eq. (1.4), is nonlinearly dependent on the parameters (μ or θ) [31]. The initial direction of maximum decrease in error is determined

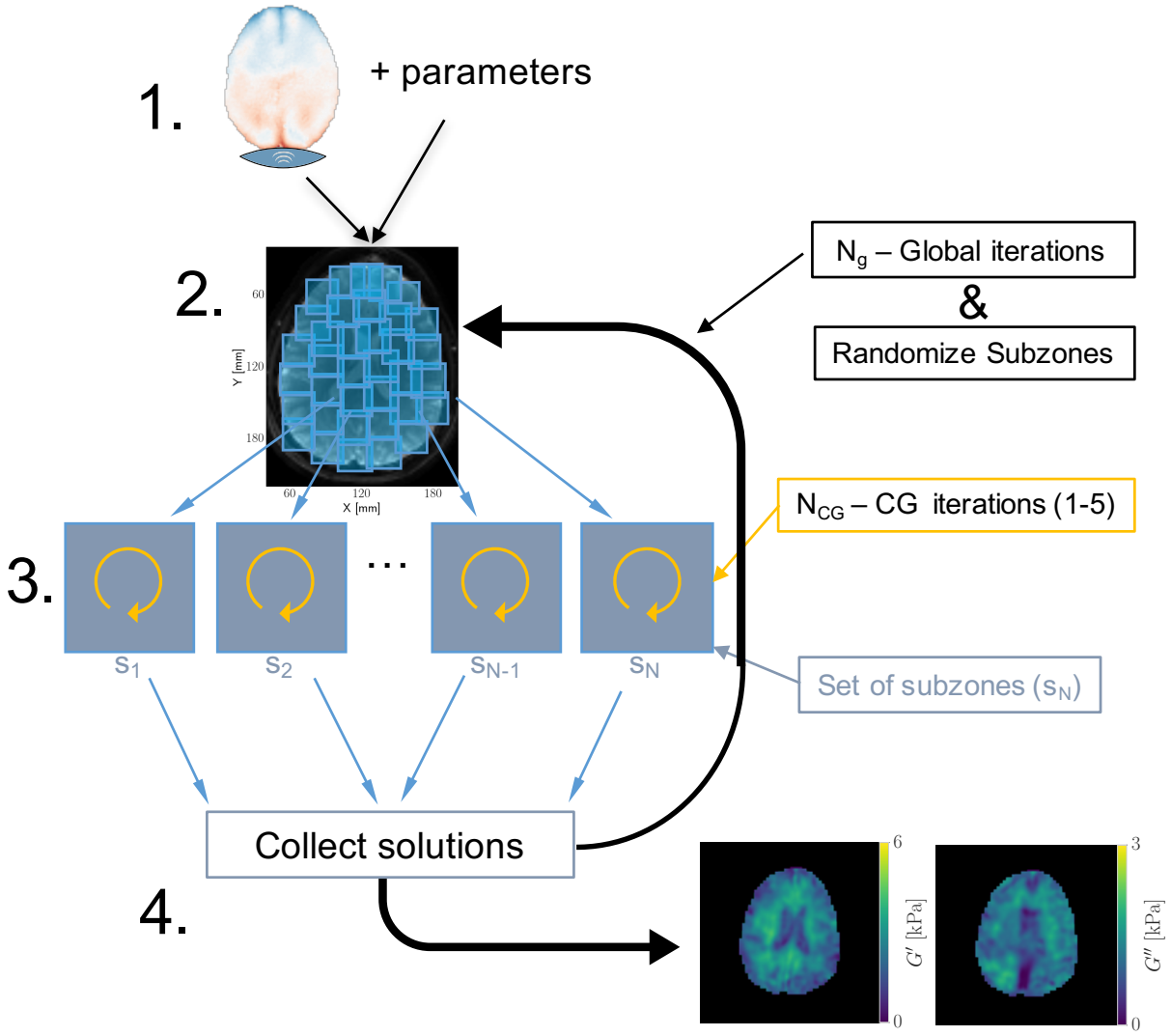

Figure 1.2: Flowchart of the NLI process: Step 1. use displacement field and parameters to setup NLI; Step 2. creates subzones from the full domain; Step 3. perform CG iterations for updating the material estimates; Step 4. combine all the estimates from the subzones back into the full domain; the process is repeated (global iteration) until convergence is reached.

from the line search along the direction of steepest descent ($\boldsymbol{p}$):

$$\boldsymbol{p}_k = -\boldsymbol{g}_k + \beta_k \boldsymbol{p}_{k-1} \tag{1.8}$$

where $\boldsymbol{g}_k$ is the gradient vector and β_k is the Polak-Ribère formula. The gradient vector ($\boldsymbol{g}_k$) is calculated by taking the derivative of the cost function with respect to the material properties (θ). Historically, the number of CG iterations starts with only one (1) per global iteration for the first ten (10) and then increases to two (2) CG iterations per global iteration. Chapter 2 is an investigation into the sensitivity of NLI parameters, including the optimal number of CG iterations. Admittedly, this is a very small number of CG iterations, but the regular re-subzone of the domain, at each global iteration, acts as a regularization against the ill effects of subzone-specific solutions.

1.1.2 Viscoelastic Material Properties & Derived Measures

Viscoelastic materials are inherently frequency dependent and this behavior is captured in the shear modulus via real and imaginary parts:

$$\mu(f) = G^*(f) = G'(f) + iG''(f), \tag{1.9}$$

where G' and G'' are known as the storage and loss modulus, respectively. The temporal dependence means viscoelastic materials are known to exhibit both creep and relaxation with respect to duration of applied load and frequency of applied excitation. Although some MRE researchers incorporate frequency as a parameter into their material estimations models [32–34] and even within NLI [35], the majority of development in clinical liver applications and brain research uses a single frequency. Using only one frequency decreases the total amount of imaging down to approximately ten minutes, which has allowed it to be incorporated into research and translational clinical studies more easily. Repeated experiments of single

frequency NLI-MRE have shown repeatability of material property estimates (G', G'', and derived quantities) under 10% across brain regions [36, 37]. Additionally, single frequency NLI-MRE has proven it's sensitivity across normal populations, diseases, and interventions [13–16, 38–41]. Equation (1.9) reduces to a single frequency of 50 Hz (assumed throughout this work):

$$\mu(f = 50 \text{ Hz}) = \mu = G' + iG''. \tag{1.10}$$

The choice of applied excitation at 50 Hz is based on compromise between patient discomfort at low frequencies ($\sim$25 Hz) and strong amplitude attenuation in soft tissue for frequencies approaching 100 Hz. The choice is not entirely quantified but there is currently no evidence, at for least single-frequency MRE, to deviate from the chosen value.

Using the real and imaginary parts of the shear modulus, there are two computed parameters of interest to MRE researchers: damping ratio

$$\xi = \frac{1}{2}\left(\frac{\mu_i}{\mu_r} - \frac{\rho_i}{\rho_r}\right), \tag{1.11}$$

and shear stiffness

$$\mu_{stiff} = \frac{2|\mu|^2}{\mu_r + |\mu|}. \tag{1.12}$$

For the case where the density (ρ) is strictly real-valued (assumed throughout work), the damping ratio reduces to the commonly known loss tangent ($\tan\delta$), differing by a factor of (1/2):

$$\xi = \frac{1}{2}\frac{G''}{G'} \sim \frac{1}{2}(\tan\delta) \equiv \frac{1}{2}\left(\frac{E''}{E'}\right), \tag{1.13}$$

where E represents the elastic modulus. For reference, the loss tangent for the harmonic loading of a linear viscoelastic material like human tissue is ~ 0.6, and corresponds to the phase shift of the stress experienced by the material lagging the applied strain [42]. This produces an elliptical loading diagram known as a Lissajous figure with positive slope and loss tangent determines the ellipticity. The (dynamic) shear stiffness (μ_{stiff}) is a common

term which relates to the wave speed in an attenuating material ($\rho = 1000$ kg/m^3) [4, 43].

1.2 Applicability of MRE for Human Brain

1.2.1 Mechanics of the Brain

The biological response of single cells can alter the mechanical properties and result in macroscopic changes "visible" to a range of quantitative imaging techniques ranging in scale from single cells using optical coherence tomography (OCT), thin tissue sections using ultrasound elastography (UE), and full organs using magnetic resonance elastography (MRE). All of the imaging techniques share the common attributes of being non-invasive, quantitative, and typically, use either a viscoelastic or poroelastic model. Each of the attributes are important for capturing both normal function and disease-causing dysfunction. The applicability of each is dependent on the tissue of interest and the physiological process under observation. For characterizing the human brain, of interest to this work, MR imaging is uniquely suited because the brain is inaccessible due to the skull and MR imaging has the technical advantage of volumetric information.

1.2.2 Stiffness Biomarkers

The human brain is one of the softest tissues in the human body and the most biologically sensitive to both external and internal stimuli. Complex tissue properties and the wide range of potential pathologies makes the brain of interest to both the scientific and medical communities. Basic science is interested in the mechanical biomarkers associated with a range of cellular processes from normal development, repair, and variation up through specific disease effects [44]. These differences may remain cellular and diffuse (e.g. normal aging) to more collective behavior of large scale phenomenon (e.g. tumors) [45–47], or acute traumatic damage [48, 49]. The mechanical properties of single cells are governed by its function as

well as affected by its environment [50–56]. There is a large body of evidence to suggest the brain's white matter becomes more anisotropic in structure with age until about 30-35 years old, then declines with age [57–60]. The anisotropy has been hypothesized to come from continual neurogenesis starting at birth through adolescence and into adulthood which all help to promote tissue health [61]; however, the newest research suggests there is little evidence for neurogenesis beyond the first year of life [62]. Clearly there is a need for improvements in measuring this phenomenon, especially *in vivo*, with known sensitivity to important cellular properties.

Beyond the neuronal-level differences, there are more prescient issues related to overall variation within a subject, within a group, and across the progression of a disease. For example, since brain tissue is soft, it is inherently susceptible to global pressure changes causing more or less compression, be it from normal variation of intracranial pressure (ICP) [63] or a disease like hydrocephalus [64]. A pressure applied to the tissue is known to cause the soft tissue to appear stiffer than the uncompressed state, known as "strain-stiffening" [65]. Looking to use this artifact as a biomarker, MRE applied to an animal model shows potential as a surrogate to measuring ICP non-invasively, which is currently either not possible or extremely invasive [63]. Applying artificial compression, potentially via the Valsalva maneuver, may even be able to elucidate an otherwise missed biomarker where glioma cells become more stiff under compression than neighboring normal tissue [55, 66]. MRE inversion methods are being developed and tuned to capture pressure changes as a biomarker [67]. How sensitive MRE is to pressure and other normal physiological variation (e.g. blood pressure, circadian rhythm, hydration) remains an open question.

Excitation Transmission and Propagation

Although elastographic imaging techniques can claim a certain capability at "*in vivo* rheometry," each technique has factors providing more information than bench top rheometers but also inherent practical issues hindering its performance. For MRE, the application of an

external shear source and its transmission through brain tissue affects the measurement and material modeling [68–70]. More specifically for the human brain, the excitation is applied to the skull and relies on the efficient transmission of shear energy from the skull through layers of meninges to the brain tissue. A study by Badachhape et al. used accelerometers with the MRE experiment and found the shear wave "significantly attenuates and delays transmission of motion from skull to brain" [71]. Integrity of the meninges is critical to ensuring sufficient applied strain and thus a successful MRE experiment. Once the shear wave has entered the brain, it must travel through a highly heterogeneous tissue with discontinuities and, for WM, high degrees of anisotropy. In the human brain, heterogeneity arises from the structure (i.e. overall shape, folds, distinct hemispheres), fluid and solid components, distinct regions, and grey and white matter. The WM is of particular importance because well-ordered anisotropic materials affect the direction and polarization of the wave, known as waveguiding. Waveguiding is important for understanding damage associated with traumatic brain injuries (TBI), and it has been leveraged as a way to characterize tissue material properties in MRE [20–23, 72–74].

1.3 Overview of Dissertation

Our group and collaborators have shown, using NLI-MRE, the mechanical properties of the brain are sensitive to performance differences on memory tasks in healthy individuals [14] and subtle differences in subcortical grey matter [13,15,75], and in diseases, including: hydrocephalus, epilepsy, and cancer [8]. All of the aforementioned stiffness biomarkers have been able to be captured because of increased coverage and spatial resolution of MR imaging, and improvements in modeling and algorithmic development within NLI. The work presented here furthers the specificity and sensitivity of the NLI-MRE process through the following areas: characterization of NLI parameters on material property estimates, develop convergence criteria for iterative MRE estimations, understand NLI's interpretation of anisotropic

white matter properties, and capture material property changes in the human brain by performing a cross-sectional *in vivo* study involving two cohorts, young and old adults.

NLI Parameter Study The "standard" set of parameters used in NLI has been quantitative and empirically determined over multiple studies [13, 14, 27, 37, 38], but there has not been a rigorous study characterizing repeatability and accuracy for a wide range of parameters. This study focuses on the two parameters expected to dominate the overall behavior of the inversion: size of subzones and number of CG iterations used to update material properties at the subzone level. This, primarily computational, study utilized a heterogeneous, isotropic agar phantom and eight repeated MRE experiments on a single subject. The outcomes of this work are to quantify the effect of parameter choice on reconstructed material properties towards "gold standard" parameters for future studies, which could be tuned to the tissue of interest (i.e. physical phantoms, animal models, or human brains).

Convergence Criteria Given the matrix of parameters, CG iterations and subzone sizes, in the previous section, it is important and necessary to define convergence criteria for the point-wise material property estimations. Two convergence criteria are proposed: (*i*) percent variation with global iteration relative to the mean and (*ii*) stiffness variation threshold with global iteration. Iteration-based criteria for material estimation convergence will provide a metric for future NLI studies by setting *a priori* thresholds for NLI reconstructions. The outcomes from this work will directly affect the quality of subsequent work proposed here and other studies utilizing iterative estimations, not just NLI-MRE.

Multi-Excitation MRE The goal of this work is to capture the effect of the isotropic material model assumption when reconstructing anisotropic tissue under distinctly different external excitations. In order to determine the level of potential discrepancy of an isotropic material estimation within highly anisotropic materials it was necessary to create an experiment where shear strain illuminates the different characteristics of the material. Since

it is not possible to control the shear strain within regions of the human brain, the multi-excitation experiment was created to achieve as close to perpendicular shear as possible by using two passive drivers on the subject's head: one at the posterior of the head and one on the left side. The multi-excitation experiments have shown the isotropic estimation was able to capture anisotropic differences and points to potential benefits of using an anisotropic model to accurately identify anisotropic biomarkers. The multi-excitation experimental data will be used as a guide for future development of anisotropic material model reconstructions and the experimental design will be implemented in the aged human study.

Aging of the Human Brain The NLI-MRE framework has shown the capability to probe both neurodegenerative disease and identify subtle differences within healthy human brains. The goal of running MRE experiments on aged human subjects is to capture macroscopic anisotropic effects of aging, previously observed using diffusion tensor imaging (DTI), which might provide new insight into how the components of tissue microstructure change with age. DTI is a method for measuring the restricted diffusion and correlates with the structural organization of the tissue. Although DTI and MRE imaging techniques both interrogate mechanical structure of the tissue, the ultimate goal for MRE is to identify biomarkers not previously elucidated with DTI. Previous MRE studies have investigated whole brain and regional effects of aging on the human brain with trends in some regions decreasing in stiffness by approximately 1% per year [**?**,76–78]. The softening is hypothesized to come from general degradation of neurons and supporting cells (e.g. glial, oligodendrocytes, astrocytes). Additionally, this study considers an area not previously addressed in MRE studies, specifically how the micro softening has the macro effect of causing changes to wave patterns within the tissue.

Chapter 2

NLI Parameter Study

A number of studies using magnetic resonance elastography (MRE) have shown both the sensitivity and specificity for detecting group differences and subtle changes in the human brain [13–16, 38–41]. Improvements in MR imaging techniques have improved both the signal-to-noise ratio (SNR) and the resolution of measured displacement fields [36, 38, 79]. Previous studies of nonlinear inversion (NLI) have looked at the dependence of the NLI parameters on final material reconstructions but have mostly been limited to a tight parameter range and only within simulations and phantoms [80–82]. One study of NLI has looked across simulation, phantoms, and *in vivo* but was only interested in mesh resolution [27]. The parameters under investigation in this study were guided by the previous studies, but the range of parameters was more physically relevant and includes analytical, simulation, phantom, and *in vivo* human brain experiments. The construction of the phantom is similar to previous studies, a helpful comparison, but the *in vivo* experiments provide the critical extension to previous work necessary for understanding parameter affects on elastograms and statistics.

The algorithm of NLI takes MR displacements as input, computes a finite element forward solution, and an iterative optimization estimates tissue material properties. Each of these three areas could, and should, have entire studies devoted to their effects on the final material property estimations. Since the imaging is state-of-the-art, this study assumes the input displacements are as good as possible and the material formulation, heterogeneous isotropic viscoelasticity, is the most appropriate for the materials and tissues of interest. This study looks to improve the dominant usage of NLI for MRE studies by using the most common

formulation of the algorithm, nonlinear conjugate gradient (CG), and identifying the most sensitive parameters.

The distinguishing features and benefits of NLI for MRE include an iterative estimator, a heterogeneous material formulation, and the decomposition of the full problem into overlapping smaller domains ("subzones"). The subzone formulation makes a large finite element problem more tractable computationally and reduces the direct dependence of estimation on measured displacement fields. Since the initial implementation, advances in computational hardware have allowed for a wider study to investigate the impacts of subzone size on the reconstruction process, not previously afforded [82]. Aside from their role in parallelizing the computational task of reconstruction, the subzone decomposition process has the important benefit of allowing a distribution of measured displacement points within the imaging domain for Dirichlet boundary conditions (BC) used to drive the forward finite element (FE) problem underlying the reconstruction process. Additionally, NLI assumes a continuous domain and smaller domains allow greater flexibility to handle model-data mismatch. The size of the subzone, however, has the drawback of introducing a length scale into the problem which is not inherently part of the domain. The goal of this portion of the study was to find a subzone size which minimizes its effect on the material estimations.

NLI has implemented three different optimization algorithms for material estimation: Gauss-Newton (GN), nonlinear conjugate gradient (CG), and quasi-Newton (QN) [30]. Iterations are computed at the subzone-level, with only a limited number of CG iterations possible before solutions become unstable or begin optimizing for subzone-specific properties. Additionally, the convergence of the estimation is highly dependent on the collective reduction of error across all subzones. The goal of optimizing the CG iteration structure will be to reduce the overall error without making it dependent on the specific subzone. The goal of this portion of the study was to determine the iteration structure which improves accuracy in the most computationally efficient manner.

Although a long list of parameters and experiments could be proposed, the most influential

parts of the NLI process, based on empirical and quantitative information, are expected to be the decomposition of the full problem into subzones and the estimation iteration structure at the subzone-level. This chapter finishes with some suggestions for future studies based on the expected next highest-order of importance. The dependence of property estimations on the parameters is not unique to NLI nor MRE and all measurement techniques are engineering problems under continual improvement [83].

2.1 Methods

The goal of this work is to formalize the NLI-MRE parameters and process to produce both the most accurate and reliable estimates. The experiments are designed to provide the data for the three most common experiments: "*in silico*" analytical solutions, physical heterogeneous phantoms, and *in vivo* human brain. Analytical solutions allow the investigation of singular phenomena, phantoms are the simplest physical experiment, and *in vivo* imaging is the full capabilities and limitations are tested. Fortunately for this study, the MRI displacement acquisition for *in vivo* experiments is state-of-the-art with the highest SNR-efficiency, allowing for clinically relevant imaging times [37].

2.1.1 Experiments

Analytical Wave Solutions

Given the complexities of *in vivo* experiments and the tissue, a simple model problem will allow for isolating a single phenomenon, like domain size, which will inform understanding for the more complex *in vivo* estimations. The simplest case of shear for a material is simple shear, where the strain is confined to one plane and displacement is a function of only the dimension perpendicular to the applied shear. It is a valid solution of the 3D Navier equation (Eq. 1.1) and for the case where the plane opposite the applied shear is fixed, solutions take

the form:

$$\mathbf{u}_x(z) = u_0 \cos(kz) - u_0 \cot(kh) \tag{2.1}$$

where u_0 is the applied displacement and $k^2 = \rho\omega^2/\mu$.

To study the effects of domain size on the forward displacement calculations, the solutions are sub-divided into "subdomains" as a 1D analogy to the subzones used in the full NLI problem. The effect of a truncated domain is explored and similarities are seen with even a simple 1D solution and the larger subzone problem. Full details are in Appendix A, including extended results for $f = 100$ Hz, comparison with NLI finite element forward solution, and NLI inversions of transversely isotropic solutions.

Silicone Phantoms with Inclusions

A phantom was constructed from a mixture of A341 silicone soft gel (Factor II) and PMX-200 silicone fluid (Xiameter) with heterogeneous inclusions of varying stiffness. The background material was a 50-50 mixture and five inclusions of varying size ($8 - 29$ mm) and concentrations ($55 - 70\%$), similar to a phantom used in a previous study [30]. The phantom was constructed from silicone for its similarity in stiffness to brain tissue and stability in properties over time (e.g. months to years). During construction, small test samples were made from the range of concentrations used for the background and inclusions for separate dynamic mechanical analysis (DMA). The DMA testing employed a rotational shear plate experiment on a Q-800 DMA (TA Instruments, New Castle, DE) over a range of frequencies, see a summary of properties for material ratios in Table 2.1 (results only for the MRE actuation frequency of 60 Hz). The silicone material does not allow for variation in G″ and DMA estimation of this property is not sufficiently reliable with the current system to report and compare with NLI-MRE reconstructions.

Table 2.1: Summary of dynamic mechanical analysis (DMA) for the A341 silicone concentrations at 60 Hz (MRE experimental frequency).

Concentrations:	50%	55%	60%	65%	70%
G' kPa	1.21	1.68	2.17	2.81	3.81

Human Brain

A 29-year-old healthy male subject underwent eight separate MRE experiments (described below), leaving the MR scanner each time. Each scan was performed in a Siemens 3T Trio MRI scanner (Siemens Medical Solutions; Erlangen, Germany) at the Beckman Institute for Advanced Study and Technology, with written informed consent for an approved study by the University of Illinois at Urbana-Champaign.

2.1.2 MR Acquisition

Phantom

Each phantom was vibrated with a custom-made piezoelectric actuator connected to a sinusoidal wave signal generator (Agilent Model HP33120A). Phantoms were placed on the actuation plate and then positioned in a Philips 8 channel RF head coil on a 3T Philips Achieva system. MRE motion data was collected over eight dynamic cycles using a spin-echo phase contrast pulse sequence with a motion gradient applied in three directions. Repetition and echo times were 900 ms and 40 ms, respectively. Coronal images were acquired using $2 \times 2 \times 2$ mm^3 voxels with 2 mm slices, with no gap between slices, and FOV $= 128 \times 128 \times 55$ mm.

Human

The specific imaging parameters for MRE include two-shot in-plane spiral readout with SENSE $R = 2$; ten slabs of eight k_z sampling planes with 25% slab overlap; $TR/TE = 1800/73$ ms; four (4) temporal phase offsets; and $FOV = 240 \times 240 \times 120$ mm. External

shear waves were introduced at the anterior of the subject's head using a pneumatic actuator system (Resoundant, Inc., Rochester, MN). Additionally, diffusion tensor imaging (DTI) and high-resolution structural acquisition (MPRAGE) were acquired once on the subject. DTI was acquired using the following parameters: single-shot EPI with GRAPPA $R = 2$; $TR/TE = 8000/95$ ms; 30 non-collinear encoding directions; $b = 1000$ s/mm^2. The DTI was processed using FMRIB Diffusion Toolkit (FDT) to extract the voxel-wise diffusion eigenvectors [84]. MPRAGE is acquired for registration of subject's brain with white matter (WM) atlas, with $0.9 \times 0.9 \times 0.9$ mm^3 isotropic resolution ($TR/TI/TE = 2000/900/2.2$ ms). The registration of MPRAGE with the subject was performed using a combination of FSL's *flirt* and *fnirt* transformations and the MNI WM atlas [38, 85].

2.1.3 NLI Formulation

The practicalities of available computational resources forced the reconstruction to be formulated such that the entire domain is decomposed into smaller subdomains or "subzones" [24]. The main assumption of the subzone method is the minimization of global error is equivalent to the sum of the minimizations across all of the subzones in the full domain, Eq. (1.7):

$$\min_{\theta}(\phi) = \min_{\theta_z}\left(\sum_{z=1}^{Q}\phi_z\right) \Leftrightarrow \sum_{z=1}^{Q}\min_{\theta_z}(\phi)$$

where Q is the number of subzones defining the entire domain, ϕ is the error function, and θ_z is the material properties being estimated [25]. The error function, Eq. (1.4), on the subzone is the squared L2-norm of the difference between the measured MR displacements and the computed displacements, $\mathbf{u}_c(\theta)$, from the finite element forward solution

$$\Phi = \sum_{\Omega} ||\mathbf{u}_c(\theta) - \mathbf{u}_m||^2,$$

where Φ is used to distinguish from NLI definition and θ is the current estimate of material properties (described previously in Ch. 1, Eq. (1.4)). Three different material optimization (error minimization) algorithms, Gauss-Newton (GN), nonlinear conjugate gradient (CG), and quasi-Newton (QN), have been implemented in the NLI framework for updating the properties, θ, but the nonlinear CG method will be the focus of this study since it's the most widely used in NLI-MRE studies. The number of line searches performed (Eq. (1.8)), for updating direction of steepest descent, is one (1) for the first ten (10) global iterations and two (2) for all subsequent global iterations. All estimates, including line searches and CG iterations, are performed only at the subzone-level.

2.1.4 Parameters of Interest

As eluded to in section 2.1.3, the dominant assumption for NLI is the decomposition of the domain into subzones and the material property estimation updates via the conjugate gradient (CG) method at the subzone-level. This study focuses on the physical size of the subzone and number of CG iterations per global iteration. These two parameters are chosen based on both empirical evidence and quantitative information. The reconstruction parameters for all previous NLI-MRE studies have been fixed for stability and repeatability, denoted by "standard" in text and figures [13–16, 38–41]. Further refinement will come in future studies of both material models (e.g. anisotropy, multi-frequency) and additional inversion parameters, including regularization.

Subzone Size The study proposed here looks across a range of subzone sizes based on the expected average shear wavelength of the medium, defined by, Eq. (1.5):

$$L_s = \frac{1}{f}\sqrt{\frac{\Re\{\mu\}}{\rho}}$$

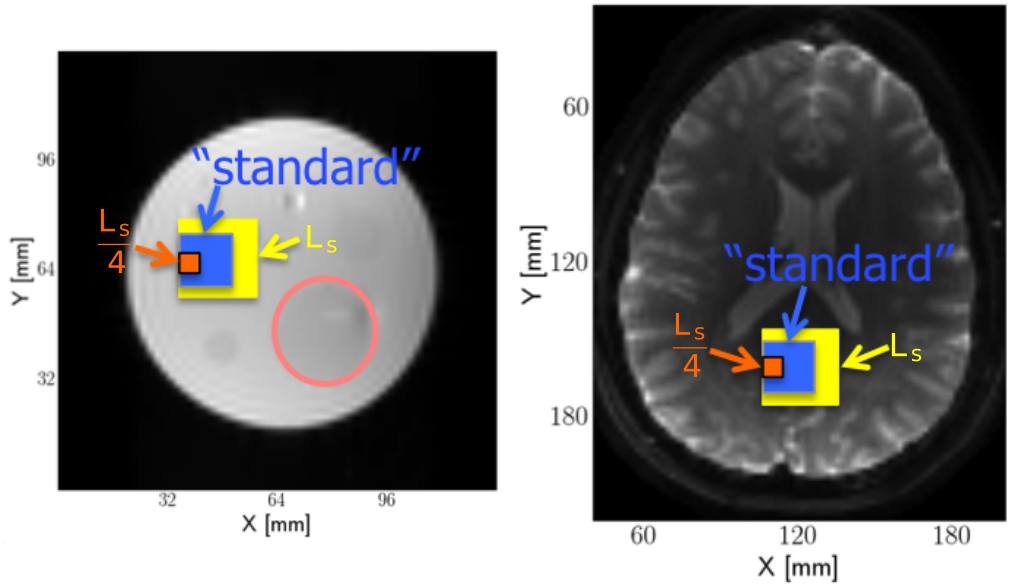

Figure 2.1: A sample of subzone sizes are shown overlaid on T2-contrast images of the phantom (left, near one large inclusion) and human brain (right). The full set of subzones always cover the entire domain, the location of centroids are randomized at each global iteration, and volume-preserving near the edges.

where f is the frequency of actuation, μ is the real shear modulus of the medium, and ρ is the density of the material. The set of subzone edge lengths range from $0.3L_s$ to $1.95L_s$, and, for reference, the "standard" size from previous studies is $0.83L_s$. The average shear wavelength, for use in the study, was determined by using the physical value from the "standard" NLI-MRE parameters (19.56 mm and CG=2), running NLI on all eight human repeats, taking the average of repeats of whole brain averages, and calculating the average shear wavelength, Eq. (1.5). The "standard" factor (0.83) was determined by comparing the previously accepted subzone size relative to the average shear wavelength. The subzone sizes were chosen to ensure sufficient range around the "standard" size and across physical dimensions of features in the phantom and human brain. The 2D projection of the subzone sizes relative to the phantom and human subject are visualized in Figure 2.1.

Conjugate Gradient Iterations As stated in section 2.1.3, the estimation of material properties occurs at the subzone level and is updated using an *a priori* prescribed number

of conjugate gradient (CG) iterations. In previous studies, the "standard" number of CG iterations at the subzone-level is chosen as one (1) for the first ten (10) global iterations and increases to two (2) CG iterations per global iteration until convergence is reached. Although the two (2) CG iteration structure has shown to be effective, it is an open question whether more iterations would improve the quality and stability of the material property estimations and ultimately the statistical power. This study looks at a range of CG iterations from one to five (1-5) iterations for the entire inversion, across the range of subzone sizes. Additionally, the single CG iteration structures were used to investigate a potentially more efficient scheme where the iterations are incrementally increased, CG = $1, 2, 4, 5$, referred to as "cascade." The cascade structure is based on using the fixed iterations global error as a reference for increasing CG iterations for the most efficient error reduction. Evaluating the CG iterations will be based on improving the accuracy of material property estimates by minimizing the error metric and improved convergence.

2.2 Results & Discussion

2.2.1 NLI Reconstructions

The material property reconstructions for the phantom and human subject, across a representative subset of parameter ranges, are shown in Figures 2.2 and 2.3, respectively, for a representative transverse slice. For both $0.3L_s$ and $0.65L_s$ sized subzones, the phantom reconstruction was unstable and increasingly unstable with CG iteration. The human subject reconstructions were stable for small subzones but the contrast was very low; however, the reconstructions for larger subzones, $1.3L_s$, were unstable in regions with discontinuous structures (i.e. *falx cerebri*) due to model-data mismatch. For stable reconstructions of both the phantom and human subject, increasing CG iterations increased the contrast of phantom inclusions and regions of the brain. Qualitatively, the "standard" subzone appears to be a reasonable choice and at least minimal improvement in contrast could be gained from

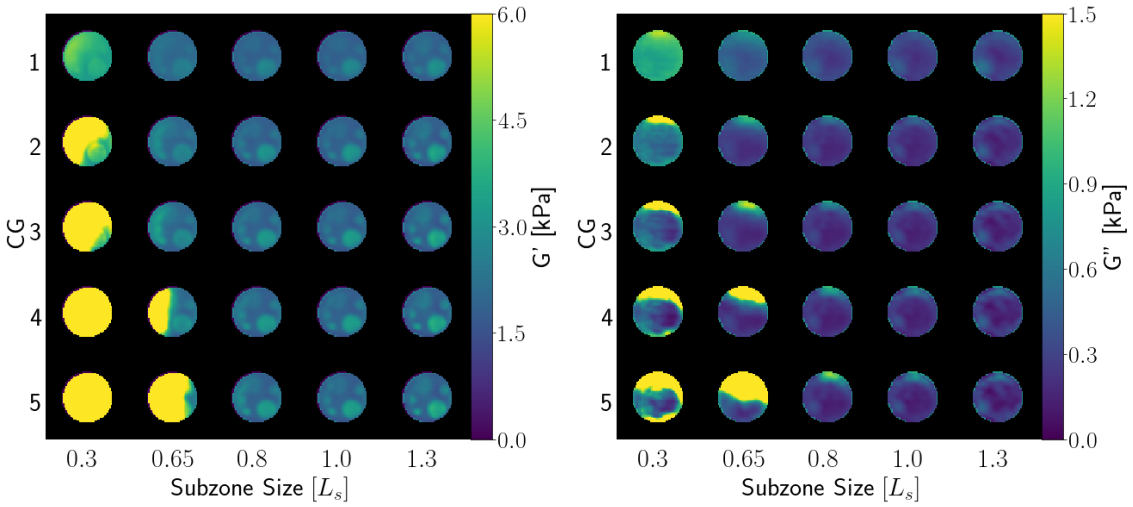

Figure 2.2: The final reconstructed elastograms of the phantom (see Figure 2.1 for T2-contrast) are shown over a subset of the subzone sizes and conjugate gradient (CG) iterations. The global iterations are the same and based on convergence of "standard" inversion parameters. The reconstructions are unstable for subzones near or below $0.8L_s$ and increasing CG iterations tends to increased the relative contrast between background and inclusions.

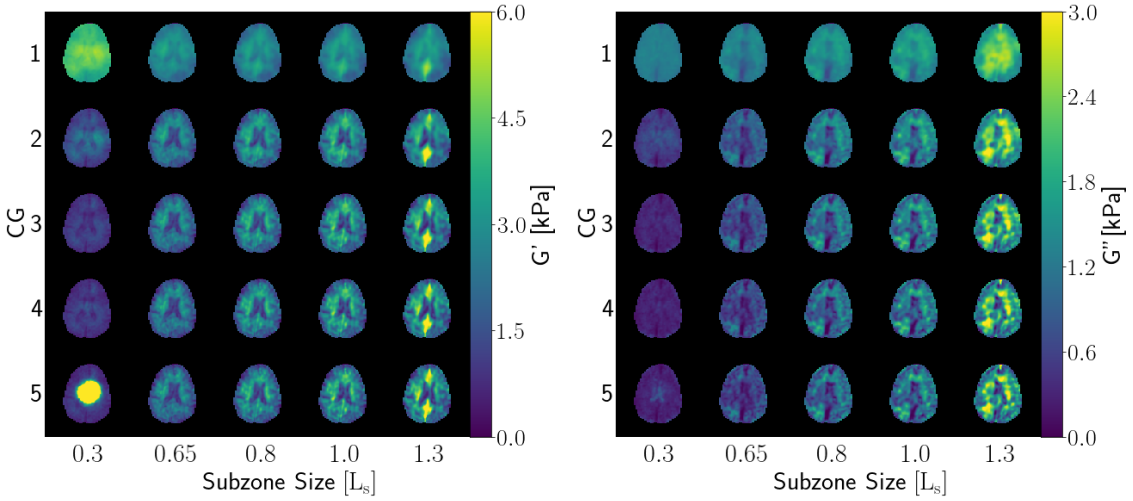

Figure 2.3: The final reconstructed elastograms of the human subject (see Figure 2.1 for structural reference) are shown over a subset of the subzone sizes and conjugate gradient (CG) iterations. The estimates are all at the number of global iterations where "standard" would be considered converged. For $0.3L_s$ sized subzones, the NLI algorithm does not deviate from the initial estimate, except for the unstable CG=5. Conversely, $1.3L_s$ sized subzones become unstable near the *falx cerebri*, likely due to model-data mismatch.

increasing CG iterations.

2.2.2 Phantom Statistics

Figure 2.4 shows the average properties of the background and five (5) inclusions across the range of parameters, with DMA measurements. Both G' and G'' are unstable for very small subzone sizes due to the small amount of displacement/strain information within the domain. One probable source for the instability at very small subzone sizes would be the limited information on shear wavelength available across such a limited domain, leading to non-uniqueness in the property solution. This is a unique feature to NLI, as compared with other MRE inversion techniques, because it assumes heterogeneity but cannot capture it within the limited subzone. Conversely, the reconstructed material properties, G' and G'', are nearly subzone independent for subzone sizes above $0.8L_s$. For the larger subzone, the algorithm can capture the subtle variation in material properties due to the phantom being made of a very uniform and piecewise continuous material that is well modeled by the viscoelastic model used in NLI. The number of CG iterations has a small effect on two stiffer inclusions for G' and no effect on G''. The stability of G'' and nearly identical reconstructed properties throughout are expected because the material was not chosen to have contrast in G''.

2.2.3 Subzone decomposition: A Blessing and a Curse

The subzone was originally implemented for making NLI solvable on available hardware with the added benefit of stabilizing the inverse problem; however, even though current hardware affords any size subzone, Figure 2.3 shows the potential issues with this freedom. The elastograms in Figure 2.3 shows how size can give both unrealistically too little contrast (small subzones) and unstable solutions (large subzone at midline). The midline of the brain contains the *falx cerebri* which is a thin, stiff structure separating the two hemispheres of the

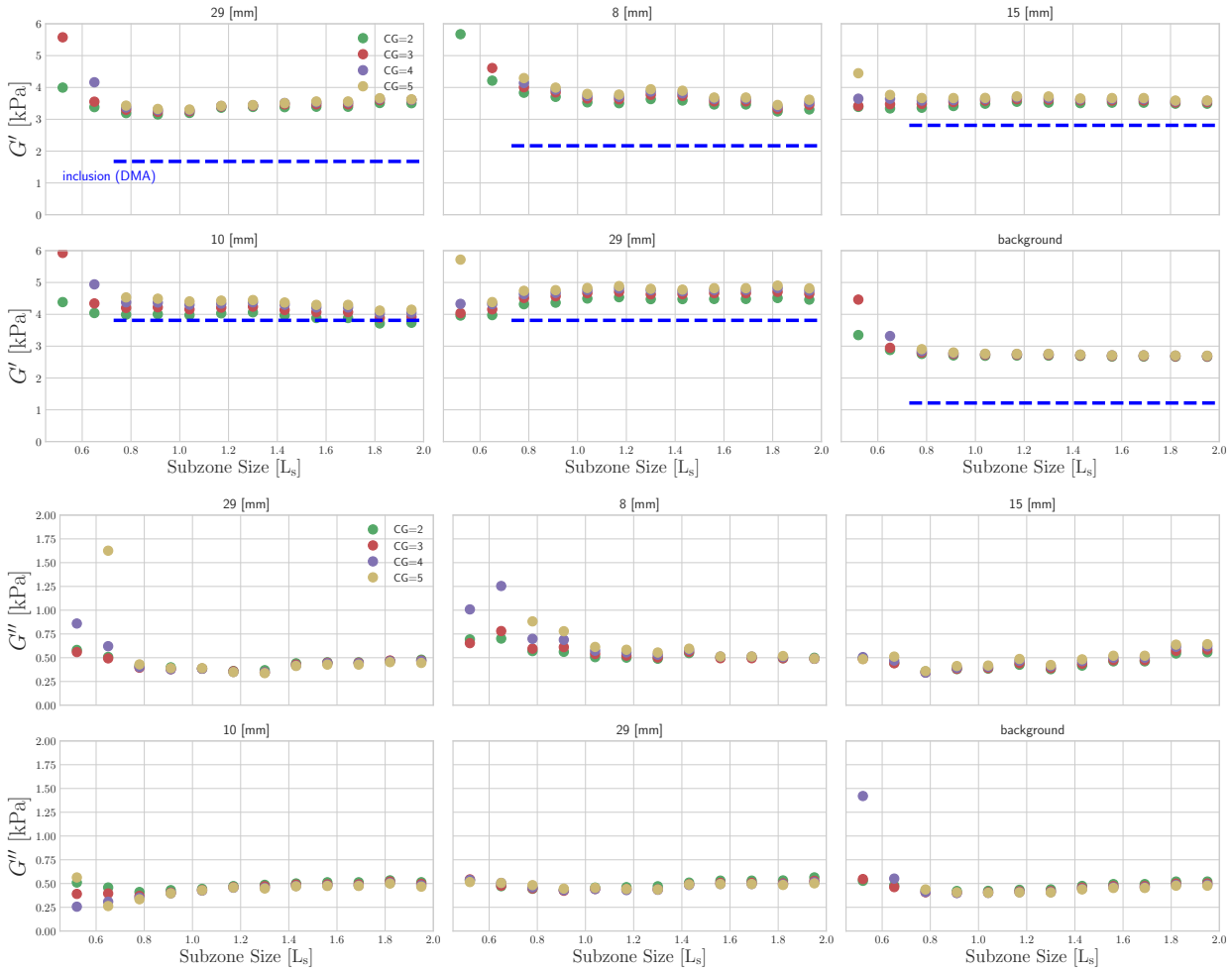

Figure 2.4: Volumetric average within each inclusion and throughout background, of G' and G'' across the range of subzone sizes and CG iterations. The DMA measurements are shown with the dashed blue line for G' (phantom does not have G'' contrast). Subzone sizes above about $0.8L_s$ are subzone size independent for most of the inclusions and background. CG iterations have a minimal effect for the larger subzones.

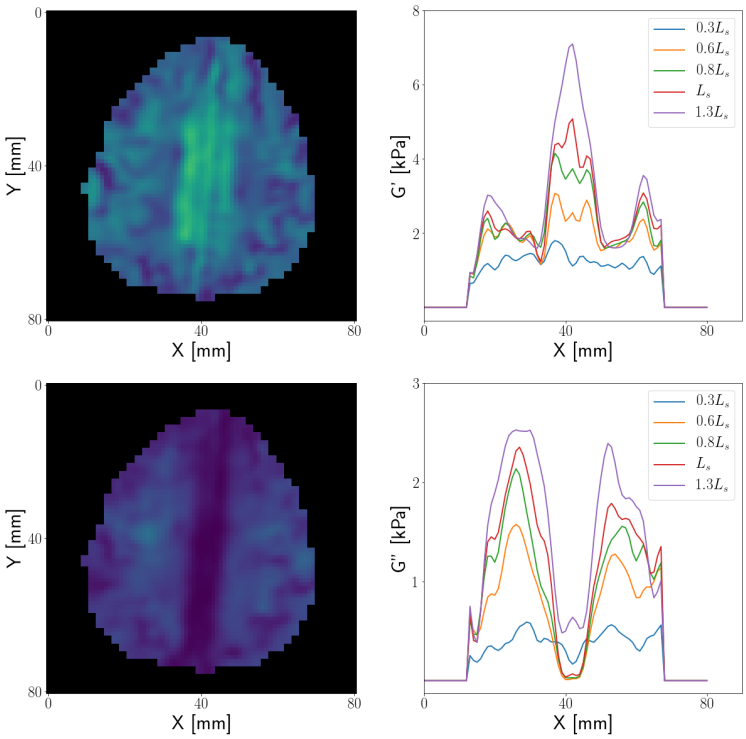

Figure 2.5: The elastograms (right) are a sample superior transverse slice containing the falx cerebri, located in the center and oriented posterior-anterior; left: line plots cutting through the center of slice show the response of NLI to subzone size. Subzone sizes in the middle handle the model-data mismatch better than the largest subzone.

brain made of dura mater. Although the NLI formulation can capture tissue heterogeneity, NLI assumes a continuous medium and, therefore, it is unable to properly model the slip-interface between the two structures. For subzones encapsulating some portion of the structure, NLI attempts to smooth the discontinuity by approximating it as a stiff structure (see the reconstructions for the three middle subzones in Figure 2.5). Surprisingly, NLI does a reasonable job of approximating both the edge of the brain hemispheres and the *falx cerebri* as shown in the line plot through the center of brain in Figure 2.5. NLI encounters problems when the subzones are large enough to encompass a large portion of the discontinuity of the *falx cerebri*, and responds to the sharp increase in stiffness (G') by decreasing the damping (G''), seen in Figure 2.5 for the largest subzone. NLI has safeguards to stop the optimization from suggesting non-realistic values (i.e. negative viscosity) and tries to regularize unrealistic property changes (usually due to noise), but significant model-data mismatch cannot be

avoided.

Explaining the Subzone Effect

Wave Equation One of the simplest time-harmonic elastic deformation situations to consider is a homogeneous plate with shear applied on a single face and fixed on the opposite side, finite in thickness and infinite in the other two dimensions, as described in Section 2.1.1. A single component of shear reduces any parameter effects to the simplest case (besides rigid body motion) without introducing the complexities of higher-dimensionality effects. To investigate the effects of domain size on the forward displacement calculation, a simple shear experiment is proposed. First, the shear deformation in a large, '*global*' domain is calculated using the analytical solution, Eq. (2.1). Next, a series of shear fields are calculated on a set of subdomains of decreasing size. For each of these subdomains initial shear fields, the domain is reduced in a successive fashion by one pixel in each direction until the smallest subdomain contains five (5) points. Additionally, the real and imaginary of the shear modulus are varied (keeping the other fixed) from $0.5G_0$ to $1.5G_0$ to model inaccurate estimates of moduli. An example of the subdomain solutions for the cases where $G'_{subd} = 0.5G'_0$ and $G''_{subd} = 0.5G''_0$ are shown in Figure 2.6. The normalized cost functions for both cases, across entire parameter space, are shown in Figure 2.7. When G' is varied, the cost function is more sensitive to the subdomain size when $G' > G'_0$; conversely, for G'' varying, the cost function is more sensitive for $G'' < G''_0$. The sensitivity of the 1D solution to incorrect values of G^* are understood by computing the linear regression of the cost function to inaccurate values of G' or G'', separating into below and above original value (see Figure 2.8b). Note, the slopes for $G^* > G^*_0$ are shown negative to compare with cases where $G^* < G^*_0$ illustrate their relative differences and mimic reduction of error toward known solution, like NLI's optimization routines.

With regards to the underestimate of G'', Figure 2.8 shows smaller subdomains have a shallower slope of error relative to the inaccuracy of loss modulus ($\mathrm{d}\Phi/\mathrm{d}G''$) than for larger

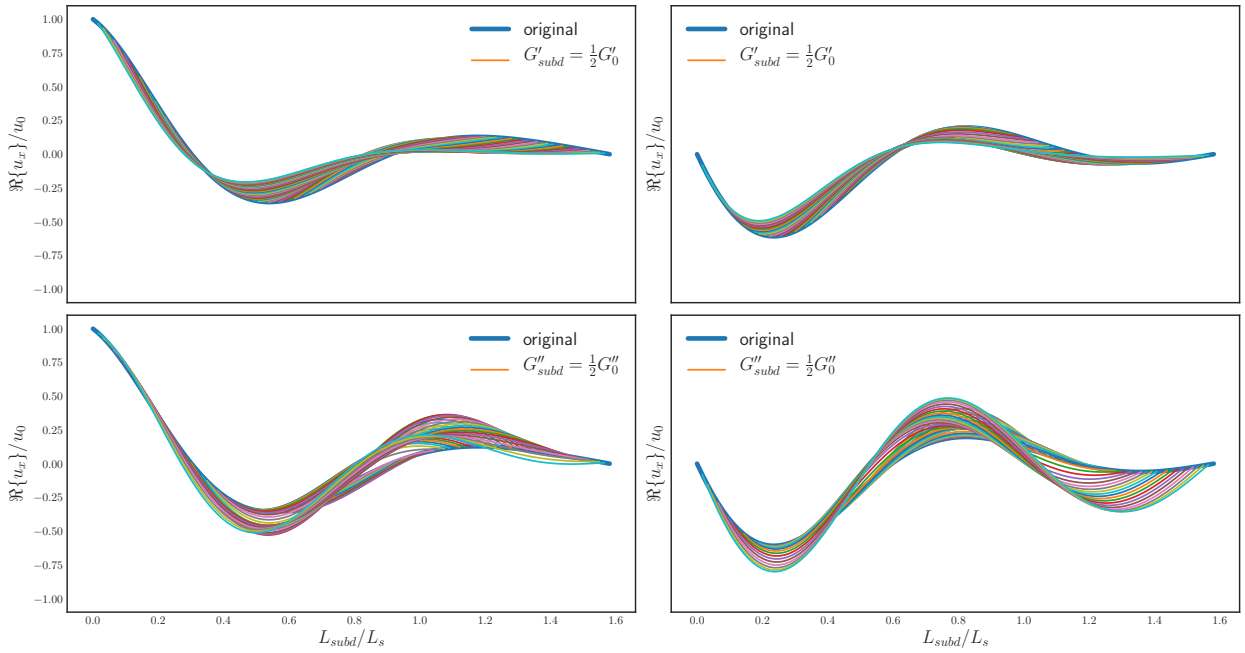

Figure 2.6: A analytical solution (*global*) for 2.1 is computed, using the properties in Table 2.2, and recomputed for "subdomains" of original solution with inaccurate solutions. The storage modulus (G') is the original value and the loss modulus (G'') is set to $0.5G''_0$. All subdomains are centered on the center of the global domain.

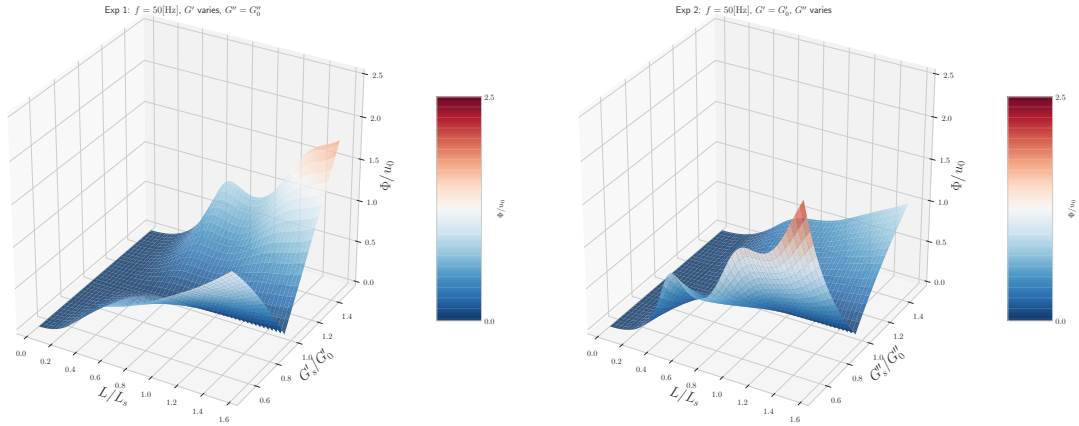

(a) (b)

Figure 2.7: Cost function for the full range of subdomain sizes and varying shear moduli for the two cases: (a) $0.5G'_0 \leq G' \leq 1.5G'_0$ and $G'' = G''_0$; (b) $G' = G'_0$ and $0.5G'_0 \leq G' \leq 1.5G'_0$.

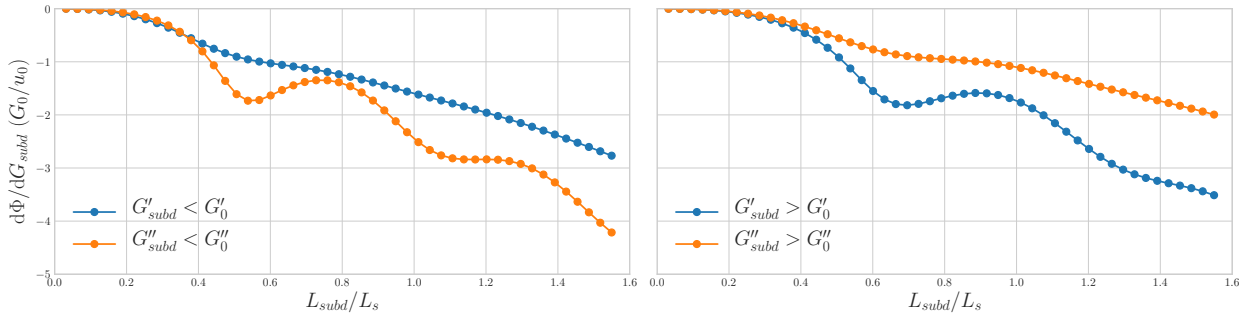

(a)

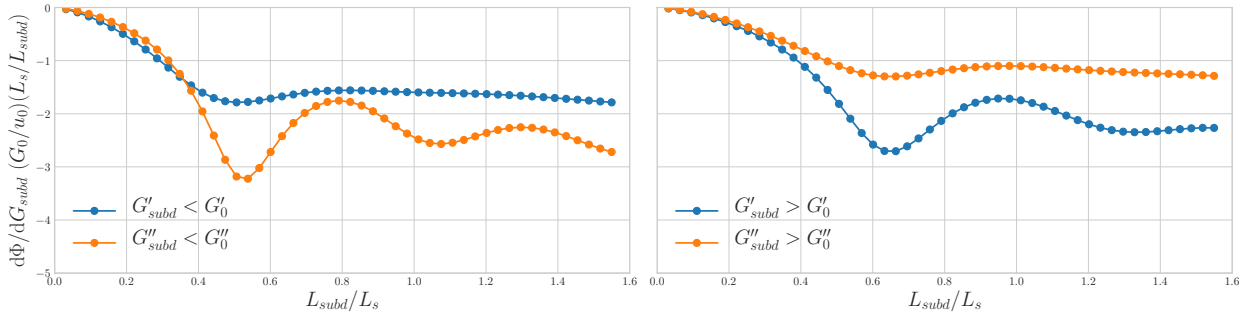

(b) Normalized version of (a) by L_{subd}/L_s

Figure 2.8: For constant domain size from Figure 2.7, the linear regression was computed for $G)subd < G_0$ (left) and $G_{subd} > G_0$ (right; negative for comparison). For small subdomains, the error is relatively insensitive to inaccuracies. For $G_{subd} < G_0$, the cost function is more sensitive to inaccuracies in G'' than G', and the converse is true for $G_{subd} > G_0$.

Table 2.2: Summary of the property values and initial conditions of the simulation experiments.

Experiment	u_0 [m/s]	f [Hz]	ρ [kg/m^3]	μ [Pa]	λ [Pa]
1-D Simple Shear	5x10^{-4}	50	$1000 - i0.1$	$2500 + i2000$	1.6489x10^6

subdomains. For values of $G'' > G''_0$, the slope is shallower across the range of subdomains. The less aggressive slope at smaller subdomains, and by extension subzones, allows for an underestimate of the loss modulus without much difference in the cost function, which governs the update in properties. The NLI algorithm uses an initial estimate of G'' of 1200 Pa which *in vivo* is most likely an underestimate. For the storage modulus (G'), the initial estimate is $\sim$3300 Pa, nearer to the final solution, and inaccuracies are less dependent on the domain size.

The previous experiments were repeated for five (5) randomized trials where the subdomain locations were randomized relative to the original solution. The sensitivities relative to inaccuracies in shear moduli were computed for all cases and shown as composite in Figure 2.9a. The behavior is very similar to "centered" subdomains but highlights the increased variance in sensitivity for nearly all cases near $L_{subd} = 0.5L_s$. This variance may help to explain NLI's inability to accurately estimate shear moduli in this regime for the full domains. For subdomain sizes approaching L_s, the level of variance with different subdomain regions is noticeably decreased, helping explain the relative stability of NLI solutions at subzones near this size. Although this is only a 1D analysis of a 3D problem, it showed the general behavior of both constraining the problem into different size domains and how inaccuracies in material properties drive the sensitivity of the cost function. A subzone should be as large as reasonably possible considering both computational constraints and biological practicalities (e.g. model-data-mismatch of the *falx cerebri*) in order to improve NLI's sensitivity across subzone sizes and locations, relative to measured displacement fields.

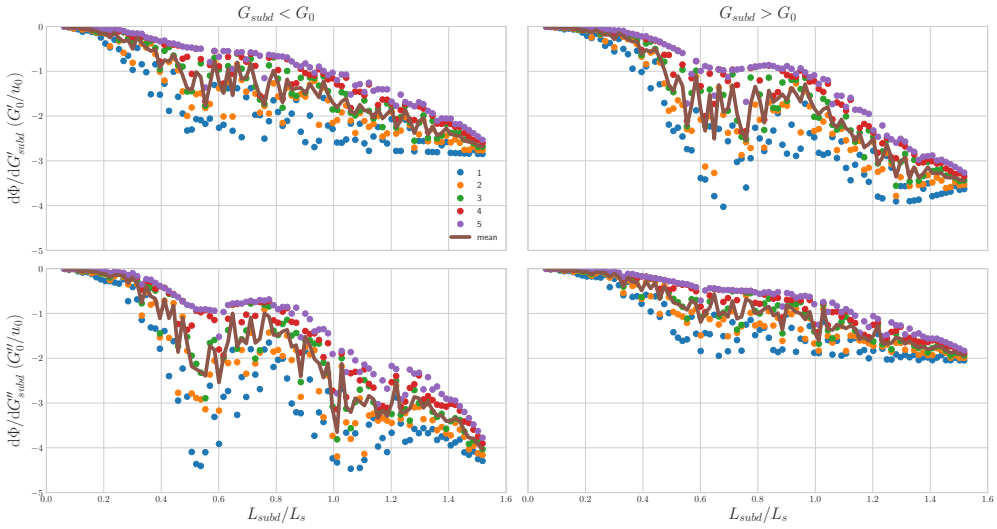

(a)

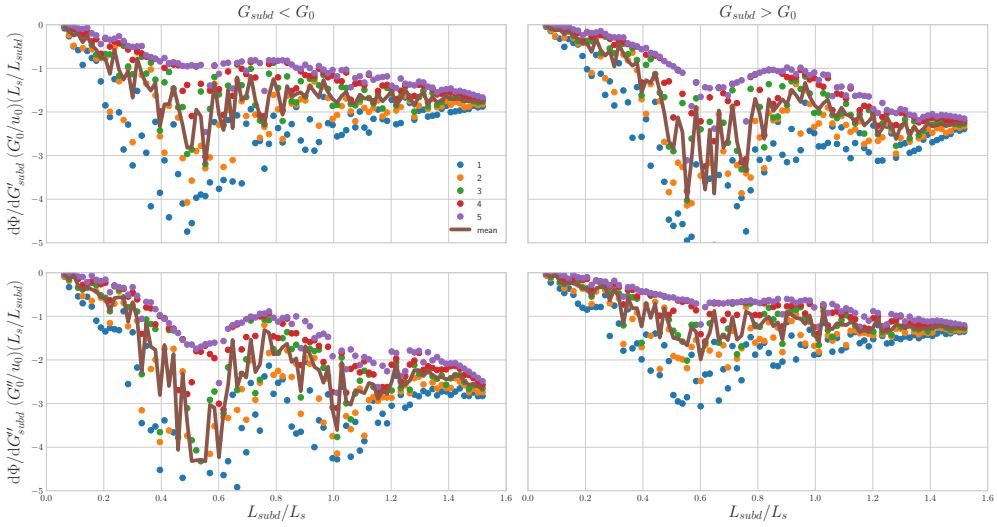

(b) Normalized version of (a) by L_{subd}/L_s

Figure 2.9: The previous 1D subdomain experiment were repeated for five trials of randomized subdomain locations throughout the domain. This illustrates the effect of position of the subdomain, and by analogy subzone, relative to the original, or by analogy measured, wave. There is increased variance for nearly all cases when the subdomain is of order $0.5L_{subd}/L_s$. Trial 1 were locations nearest face of applied shear and trial 5 were locations near fixed face, opposite applied shear.

Finite Element Forward Solutions Boundary conditions (BC) for the NLI forward finite element solution (FWD) are applied similar to the 1D problem, shear applied on one face and fixed at the opposite, but finite in the other two dimensions, instead of infinite, and $u_z = 0$ on the faces perpendicular to the applied shear. The FWD solution is computed for the same property values as the 1D solution and they match within numerical accuracy, see Figure A.2. Additionally, if the material properties are defined as $0.5G_0''$ and $1.5G_0''$, then the solutions also match the analytical solutions. This demonstrates there is no inherent three-dimensional effects to consider for simple shear in a finite domain; however, this does not preclude effects from neither more complicated shear states nor heterogeneity. Finally, defining subdomains (similar to subzones) of the 3D domain does not introduce ill effects for this simplified case, see Figure A.3.

2.2.4 Repeatability of NLI-MRE in Human Brain

The repeatability of NLI for a single subject, across eight repeated experiments, is shown in Figure 2.11 for whole brain, corpus callosum (CC), corona radiata (CR), and superior longitudinal fasciculus (SLF). The normalized standard deviation across repeated experiments of G' and G'' relative to the mean is less than 5% across nearly all subzone sizes for the whole brain. For the SLF, there is larger variability in the reconstructions of the experiments, likely due to it being a large structure spread spatially across the brain. Increasing the number of CG iterations, at the subzone level, has a minimal affect on the variability across experiments. Ultimately for reasonable subzone sizes in the human brain, NLI parameters neither change the stability nor the repeatability of the material property estimations. However, following from the last section on subzone size effects, increasing the subzone size in CR shows a reduction in the normalized standard deviation from near 10% for subzone size of $\sim 0.6L_s$ to at or below 5% for subzone size of $> 1.2L_s$.

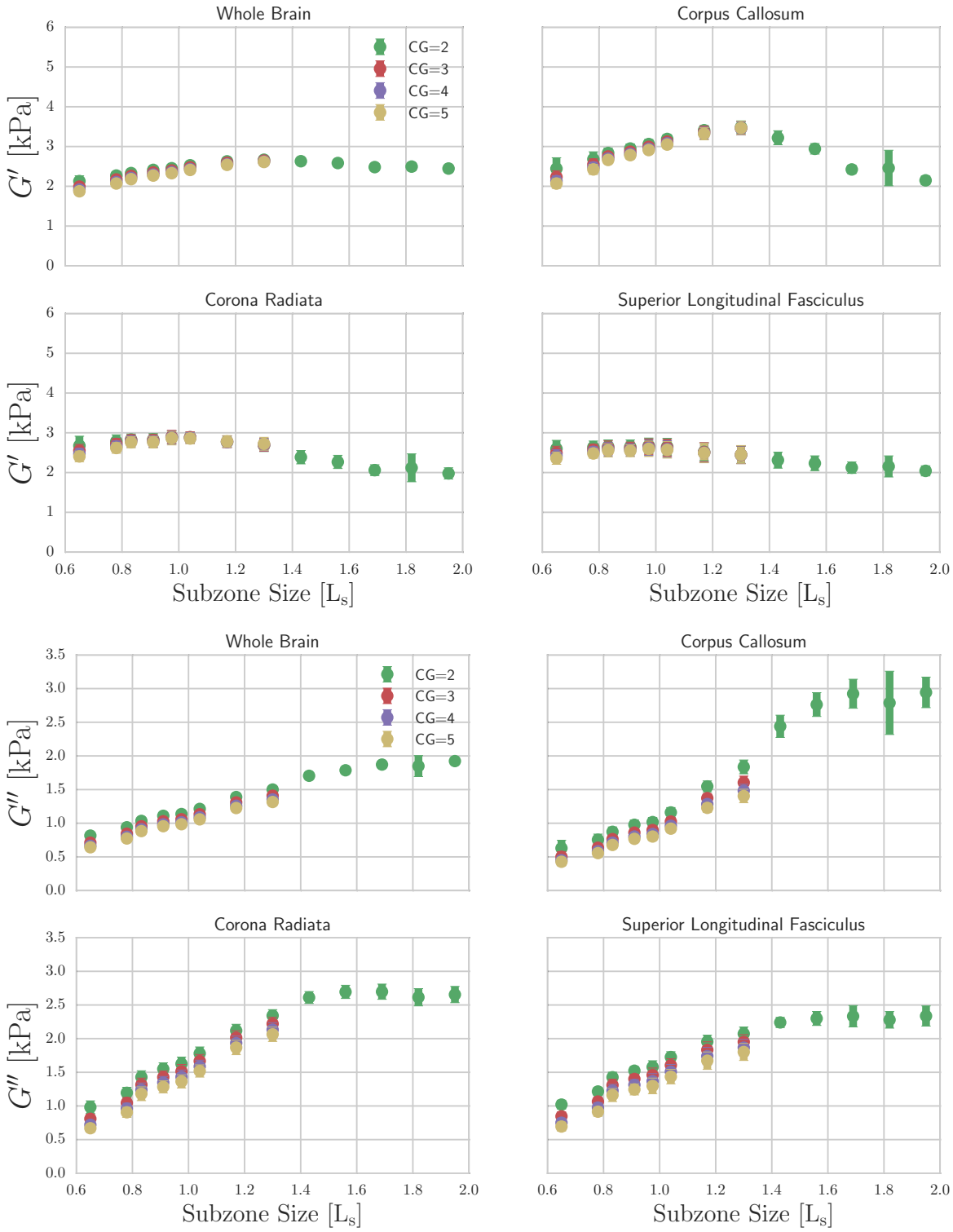

Figure 2.10: Average and standard deviation of G' and G'' across repeats of single subject for the whole brain, corpus callosum (CC), corona radiata (CR), and superior longitudinal fasciculus (SLF). For G', subzone size-independent reconstructions exist for the CR and SLF, but not CC; however, the reconstructed G'' seems to be subzone-independent for sizes larger than for G'.

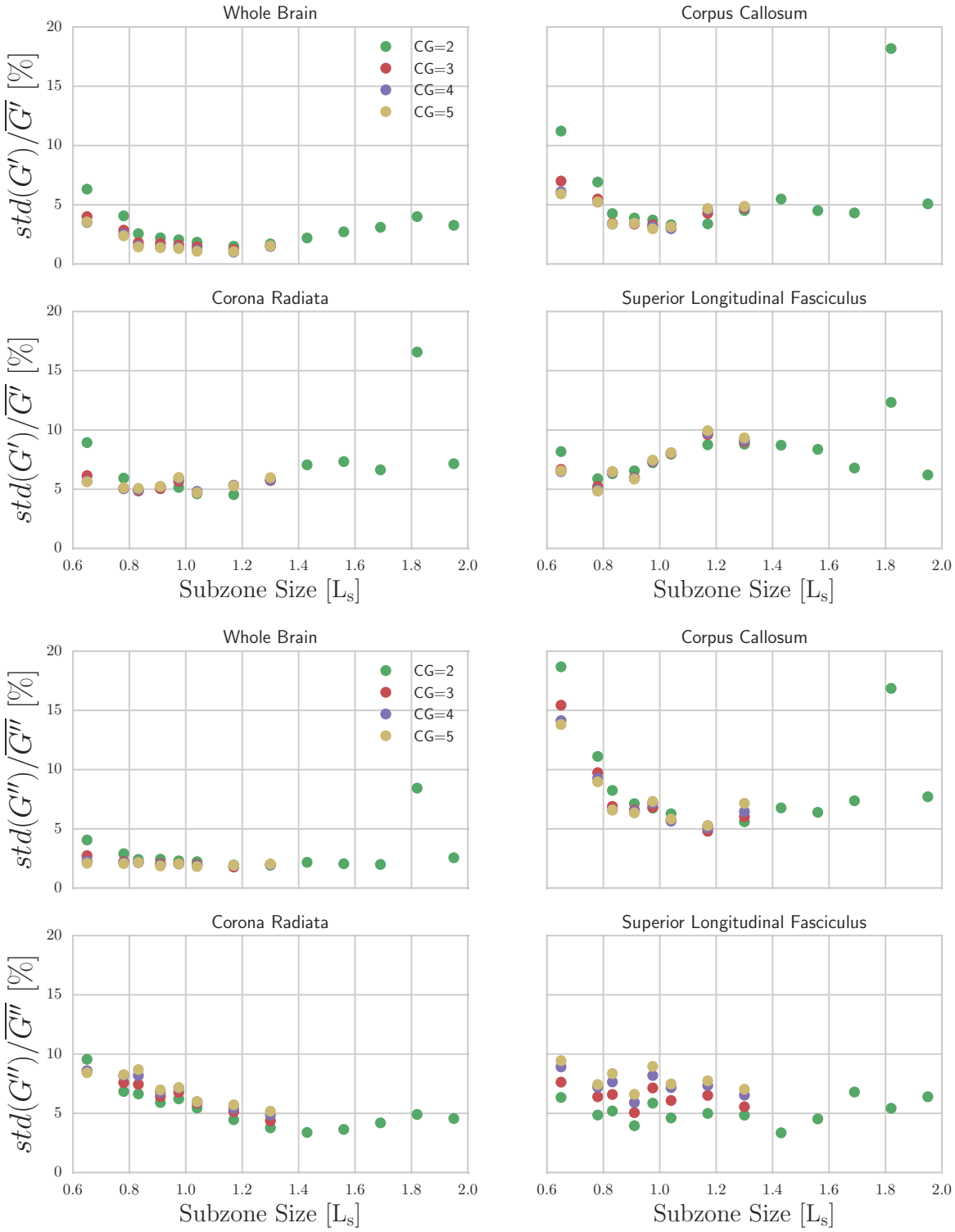

Figure 2.11: Percent standard deviation, relative to average, of G' and G'' across repeats of single subject for the whole brain, corpus callosum (CC), corona radiata (CR), and superior longitudinal fasciculus (SLF). Nearly all reconstructions have a normalized standard deviation of less than 10% across all subzone sizes where $0.8 < L_{subzone}/L_s < 1.8$, for both G' and G''.

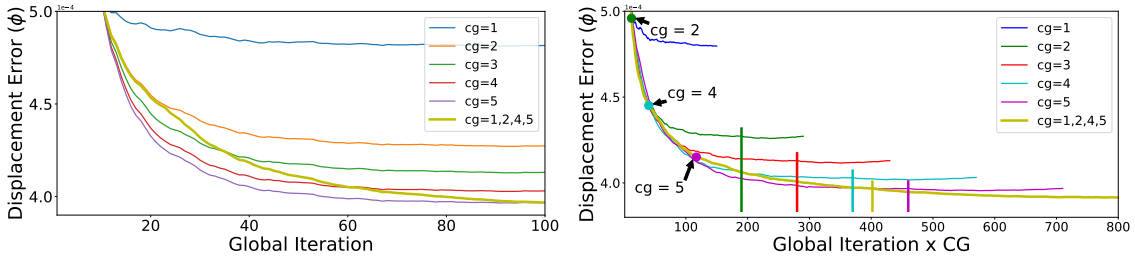

(a) (b)

Figure 2.12: (a) The global cost function, Eq. (1.4), plotted versus the global iteration for the range of CG iterations on the "standard" subzone size. (b) The global cost function versus the total CG material estimations, with the break down of "cascade" iterations structure. Each dot labels the change in number of CG iterations. The color-coded vertical lines represent the equivalent number of total iterations for the respective fixed iteration structure when it was previously considered "converged."

2.2.5 "Cascade" CG Iteration Structure

As mentioned in section 2.1.4, the conjugate gradient (CG) iteration structure starts at one (1) CG iteration per global iteration and increases to a fixed set of CG iterations. Figure 2.12a shows the global error (1.4) of a single subject ("standard" subzone size) versus global iteration for one (1) to five (5) CG iterations. Observed independently, the plateau in error would suggest convergence of the estimations; however, each increase in CG iteration is a decrease in global error, at a converging rate. The increase in CG iteration linearly increases the computation time, but plotting the global error versus the total iterations ([Global Iterations] x [CG Iterations]) shows the relative efficiency of each approach, see Figure 2.12b. If the CG iterations are increased where the fixed CG estimation error rate starts to decrease (changes indicated with color-coded dots), then the smallest error of CG = 5 could be achieved most efficiently, shown in gold in Figure 2.12b. The successive increase in CG iterations with global iterations, matched with cost function values for fixed CG iterations (see Table 2.3), improves both efficiency and material reconstructions. The resultant elastograms, a transverse plane with "standard" subzone size, are shown in Figure 2.13 and show the relative contrast differences. Figure 2.13a shows the comparison at the same global iterations ($N_g = 100$) and Figure 2.13b is significantly more iterations ($N_g =$

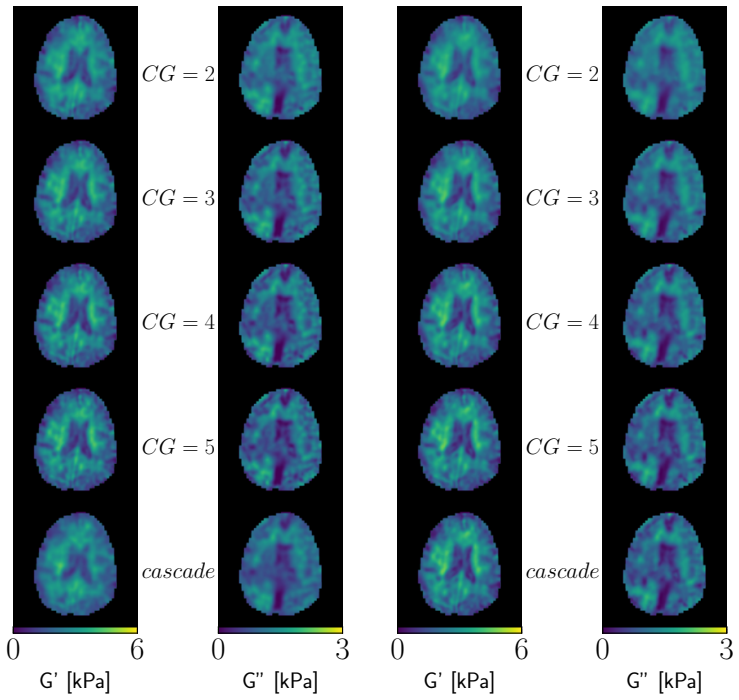

(a) (b)

Figure 2.13: As Figure 2.12 shows, there may exist a more optimal error reduction strategy where CG iterations increase at intervals of global iterations. The bottom row shows the elastograms from the "cascade" CG iteration structure ((a): $N_g = 100$ and (b): $N_g = 500$). The cascade has lower contrast for $N_g = 100$ but nearly identical at $N_g = 500$ and with reduced computational cost and error.

Table 2.3: The "cascade" CG iteration structure for given global iteration, N_g, and line searches (Eq. 1.8).

N_g	N_{CG}	Line Searches
$1-10$	1	1
$11-23$	2	2
$24-42$	4	2
$43-$	5	2

500). The contrast at $N_g = 100$ is lower for cascade than $CG = 5$, even though the global error is the same. It is likely due to the global error still decreasing for the same number of total iterations, as seen in Figure 2.12b. As global iterations increase, the contrast for both cases are nearly identical; however, the cascade structure has achieved it with lower computational cost and smaller global error. Given the enormous parameter space, it is difficult to understand how there can be a decrease in global error simply given a different iteration structure, while using the same estimation algorithm, without doing empirical studies like this one.

2.3 Conclusions

An investigation into the effect of parameters on the NLI-MRE reconstructions improved both specificity and sensitivity, the goal of all method development, but also improved our understanding of the underlying tissue. The subzone size has long been thought to have a minimal effect on the estimation but this study showed the subzone size determines sensitivity to heterogeneity, or lack there of, for very small sizes, and over-sensitivity to model-data mismatch for discontinuous regions (i.e. *falx cerebri*). The 1D analytical analysis provided a useful model of explaining this domain size-based sensitivity and how NLI cannot ever be entirely subzone-independent; however, the subzone effect is mitigated by increasing the amount of randomization by increasing total global iterations. The cost function plateau, previously thought to imply convergence, has shown to miss the potential for improved error

reduction from increasing CG iterations and higher-order fitting with significantly higher global iterations (4-5 times previous estimations). Increasing the number of total estimates, CG and global, has the drawback of increasing the computational cost. This was partially alleviated by optimizing the CG iteration structure by increasing subzone-level estimates with the slope of the cost function (i.e. "cascade"). Further improvements to the NLI framework will come from a dynamic CG iteration structure based on a real-time assessment of cost function convergence. Future studies will seek further improvements in parameter independence of NLI through identification of the next higher order of parameter effects and developing new convergence criteria for the open question of true *in vivo* properties.

Chapter 3

Iterative Estimation Convergence Criteria

3.1 Background & Motivation

As noted in the previous chapter, the cost function governing both the update of material properties and their level of convergence is not sufficient for defining "goodness" of the final estimates. Increasing the number of both CG and global iterations showed an improvement in material contrast. Increasing CG iterations always improved the global cost function value up to a global iteration, then the cost function plateaued indefinitely, see Figure 2.12. This plateau was assumed to be equated with overall convergence of the estimation across the entire domain. Unfortunately, with all single-valued measures of complex, higher-dimension domains, whether it's load capacity of a suspension bridge or gross domestic product of an entire country, the small, regional details are missed in aggregate measures.

Another option would be to look at the material statistics for the entire domain with global iteration, as described in Figure 3.1 for G'. It would also be tempting to assume the flatness of the statistics implies convergence, but it is only slightly more information than the single cost function value. The work in this study looks to identify potential voxel-wise and regional metrics for assessing the "goodness" of estimations towards the open question of true material properties of the tissue. Ultimately, setting up the NLI estimation to be as parameter-independent as possible will ensure it is converging towards the true solution. This, combined with a meaningful convergence criteria, will improve both specificity and confidence in final estimations.

Given that the known true tissue properties are an open question, the convergence criteria

will be based on determining whether or not NLI, or any iterative method, is expected to change values with future global and/or CG iterations. Since it isn't possible to see into the future, one way to determine future updates is by looking backwards with global iteration to determine how much any one voxel has changed with global iteration. Iterative algorithms require changes in estimates in order to continue searching for lower error solutions and without changes, this is not possible. Given the inherent noisiness of the MRI data, there is always going to be some variation but eventually it should be small enough where averaging over a set of the global iterations will remove these variations. This criteria is expected to provide an important missing component in defining "goodness" of reported statistics in future NLI-MRE studies. For reference, all clinical liver MRE reports include a confidence map, which is based on imaging SNR, level of known artifacts, and sufficient area of usage wave propagation; however, it has not been adopted in other applications of MRE [86]. Reasons it has not been directly adopted include: clinical decisions are mostly based on whole-liver averages with wide staging bins, the liver does not have sub-regions of interest, and OSS-SNR has been proposed as an imaging quality metric but does not define convergence of estimates.

3.2 Quality In, Quality Out

Octahedral Shear Strain SNR McGarry, et al. proposed a MR displacement imaging quality measure called octahedral shear strain signal-to-noise ratio (OSS-SNR), which is based on the information necessary for an accurate inversion (i.e. strain) instead of the traditional displacement amplitude measures [31, 87]. Although the displacement amplitude is an important characteristic, the governing equation, Navier equation (Eq. (1.1)), is a differential equation relating stress and strain via material properties. OSS-SNR is a volumetric average, within a region of interest (ROI), of the time-averaged octahedral shear strain for the displacement signal at the known frequency compared with the volumetric average of

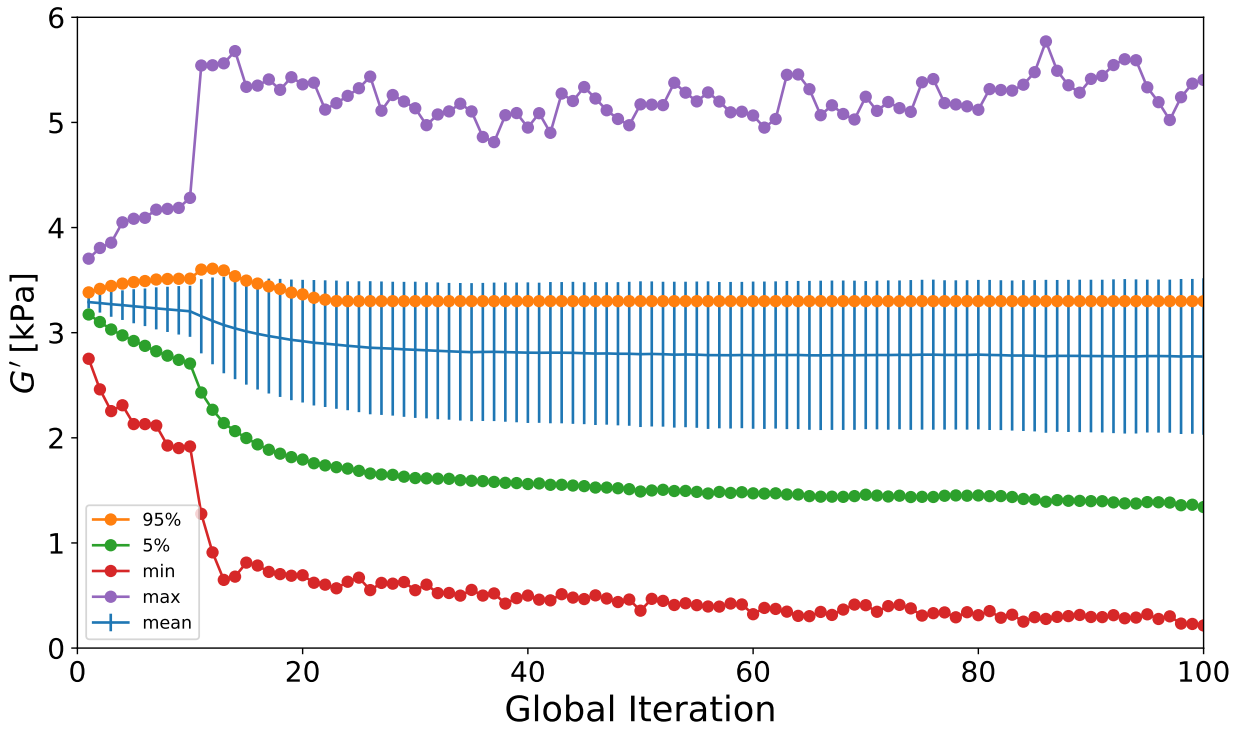

Figure 3.1: Shear modulus (G') statistics with global iteration (N_g) for a typical NLI estimation of a human brain. Properties appear converged for $N_g > 50$.

the expected strain signal from the noise. This is, and has been, an important metric for assessing the "goodness" of data into NLI, even assessing adherence of tumors [88]; however, it does not predict the "goodness" of reconstructed material properties.

The next step, once the input data has been characterized, is to have a similarly quantitative way of assessing NLI's ability to estimate material properties. The goal of a convergence criteria, independent of a known truth, can only ever be relative to it's own performance. This could come in the form of a metric characterizing the numerical methods (i.e. condition of matrices) with CG and/or global iterations. Although these are at a lower level than global metrics (i.e. subzone versus global cost function), these metrics are large relative to the ROIs of interest in the human brain. Instead, metrics at or near the voxel-level are necessary for proper assessment of "goodness."

3.2.1 Proposed Convergence Criteria

Previous studies identifying a set of "standard" NLI parameters have been informed by the reduction of global error, the repeatability of MRE imaging and NLI estimates, and regional contrast-to-noise metrics [27, 37, 38, 80, 82]. Given the formulation for error minimization, it would seem reasonable to assume the material properties have converged, but subtle variation in material properties could have similar error. Repeatability is always important but it does not necessarily imply understanding the quality of any one estimation. Contrast-to-noise metrics are useful in simulation and phantom studies, but they do not have a specific meaning for *in vivo* tissues. These reasons highlight the need for a voxel-wise, or at least regional convergence metric, of displacement error and material properties estimations.

Since MRE studies are interested in comparing regional statistics, the quality of a subject's estimation should be based on the convergence defined within regions of interest. Two material property convergence metrics are defined within regions based on the voxel-wise variation with global iteration for absolute and normalized variation. The "absolute modulus variation" threshold is defined as

$$\sigma_{G,N_g} = \sigma_{G,10} < [\text{Pa}]_{threshold}, \tag{3.1}$$

where N_g is the number global iterations used in the computation ($N_g = 10$ is used throughout). Since the variation of properties within a single human brain region can be upwards of 200%, a "normalized percentage variation" threshold defined as

$$\frac{\sigma_{G,N_g}}{\overline{G}_{N_g}} = \frac{\sigma_{G,10}}{\overline{G}_{10}} < \%_{threshold} \tag{3.2}$$

may be more appropriate. These metrics are inherently relative but are patient specific and the threshold should be reported alongside any regional statistics used in future studies.

3.3 Results & Discussion

3.3.1 Global Convergence

As was observed in Section 2.2.5, the cost function, Eq. (1.4), for the "standard" subzone across CG iterations, had plateaus for fixed CG per subzone but level-step decrease as CG iterations increased, see Figure 2.13. Each CG iteration structure reduces the global error up to a point and then appears to converge, but each successive increase in CG iterations decreases the final global error, at a converging rate. This would naturally imply the need to increase CG iterations but it comes at both a computational cost and a more subzone-specific solution. Additionally, the results for comparing $CG = 5$ with cascade at $N_g = 100$ have shown how equivalent global error can have both different qualitative and quantitative results. Previously, both would have been considered converged because the global error, Eq. (1.4), had plateaued. The differences show how within the plateau of global error the regional error is actually being shifted spatially with the randomization of subzones, where the minimization is being performed. A computationally more efficient iteration structure, "cascade," was proposed and evaluated, but a similar plateau occurs and the "goodness" is still unknown. As outlined in the previous section, two metrics have been proposed, Eq. 3.1 and 3.2, to address the convergence of material property values in the plateau of the global error, both voxel-wise and regionally.

An example of the convergence within the subject ($\%_{threshold} = 5\%$) from Chapter 2 is shown for a set of global iterations (N_g) in Figure 3.2 ("standard" size subzone and $CG = 2$). For the case when NLI was previously assumed to be converged ($N_g \approx 100$), the volume had low spatial convergence throughout the domain. It isn't until global iterations are between 400 and 500 where the spatial convergence may be considered acceptable. Interestingly, neither the fluid-filled ventricles (center of domain) nor the discontinuous *falx cerebri* (located at left-right center, posterior and anterior to ventricles) appear to ever converge. Since NLI utilizes a viscoelastic model, it might be assumed it can estimate both purely elastic and

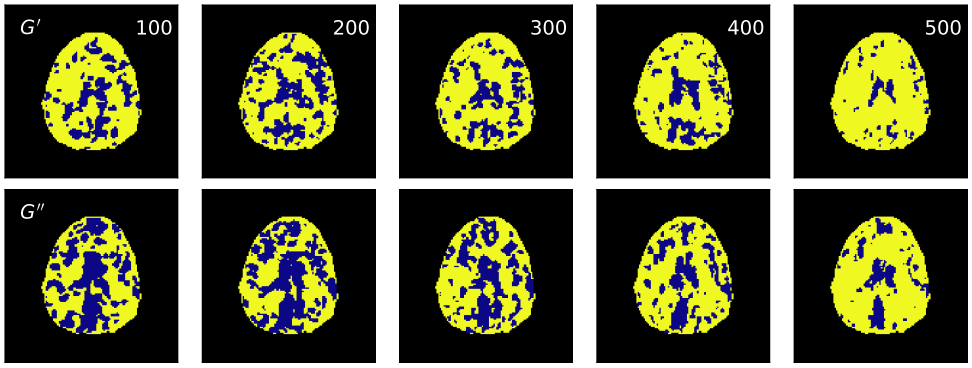

Figure 3.2: A sample slice through center of the brain showing progression of the point-wise convergence, based on new criteria, for the "standard" NLI parameters. All of these convergence maps are within the plateau of the global error.

viscous; however, fluid cannot support shear which is the dominant phenomenon observed for *in vivo* tissue. It is encouraging to see NLI does not converge for these areas of known model-data mismatch. The real power of the voxel-wise convergence criteria will be utilized within specific regions of interest in both this work and future NLI-MRE studies.

3.3.2 Region-Specific Convergence

Studies utilizing MRE are typically looking for significant effects relative to average properties within a particular brain region, however a simple mean assumes all values are equally good. Only values with some level of confidence in the estimation should be included in statistics to ensure proper characterization of tissues and remove bias from erroneous results. Defining a convergence criteria also allows researchers and clinicians to report the level of confidence with the average statistics. A regional convergence, aggregate of point-wise convergence, is shown for the SLF (using "standard" size subzone and $CG = 2$) in Figure 3.3 as a percentage of the volume for both criteria, three thresholds for each. This demonstrates the spatial convergence in an important WM region and how the total global error is thus too crude and regional convergence metrics will help define the quality of estimates within a given ROI. A value of 3% seems overly restrictive and 7% seems nearly converged at the previous usually "converged" $N_g = 100$; therefore, the 5% threshold seems

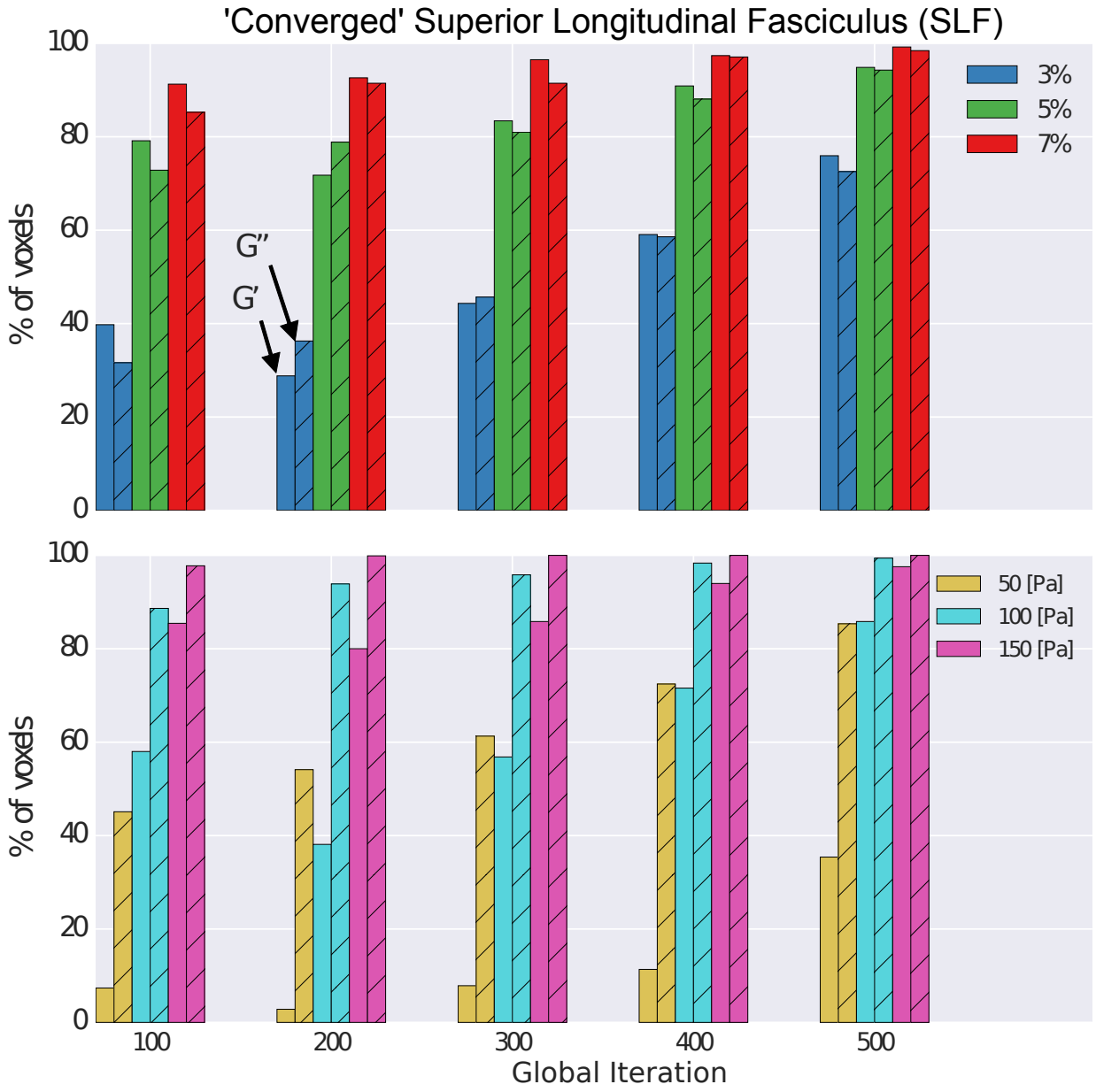

Figure 3.3: Percentage of converged SLF volume for CG iteration ("standard" parameters). The G' values are the left (solid) bar and the G'' values are the right (hashed) bar. The normalized percent variation threshold, Eq. (3.2), has a similar convergence rate for both G' and G'', but more restrictive on G' for the modulus threshold, Eq. (3.1).

to linearly increase with global iteration and equally penalize G' and G''. Conversely, the strict modulus threshold is more restrictive on G', which is always stiffer and 1D wave analysis in Section 2.2.3 showed it is more sensitive than G''. It may be necessary to have a threshold for G' and G'' separately when using a modulus threshold.

The resultant statistics, for a single experiment, are shown in Figure 3.4 (top) and highlight the difference in the reported regional averages and standard deviations. Additionally in Figure 3.4 (bottom), split violin plots show the distribution of property values for the full data and for two data sets of only converged values. At least two interesting observations can be made about these distributions and how averages obfuscate details: distributions are bi-modal and converged distributions have different distribution statistics than the full volume.

3.4 Conclusions

These convergence criteria provide a fast and simple way to avoid the inclusion of poorly developed material property values within the regional statistics used in MRE to assess changes due to physiological conditions such as age or disease. When the proposed convergence criteria is applied across a set of global iterations it is a combined way of determining whether randomization of subzones and further estimations ($N_g \times N_{CG}$) are likely to change with any successive iterations. These are two important characteristics to capture and reduce their effects because, as was demonstrated in the previous study, subzone effects and CG iterations are two primary contributors to NLI estimations. Figure 3.2 shows portions of the brain (e.g. *falx cerebri*) that are poorly characterized by the viscoelastic continuum model, underlying NLI, which are easily excluded from the converged distribution by application of these criteria. Future studies into the convergence of single voxels up to ROIs should include comparisons with the spatial maps of OSS-SNR and implemented into full studies to test the hypothesis of improved statistics (see Chapter 5). Additionally, such convergence

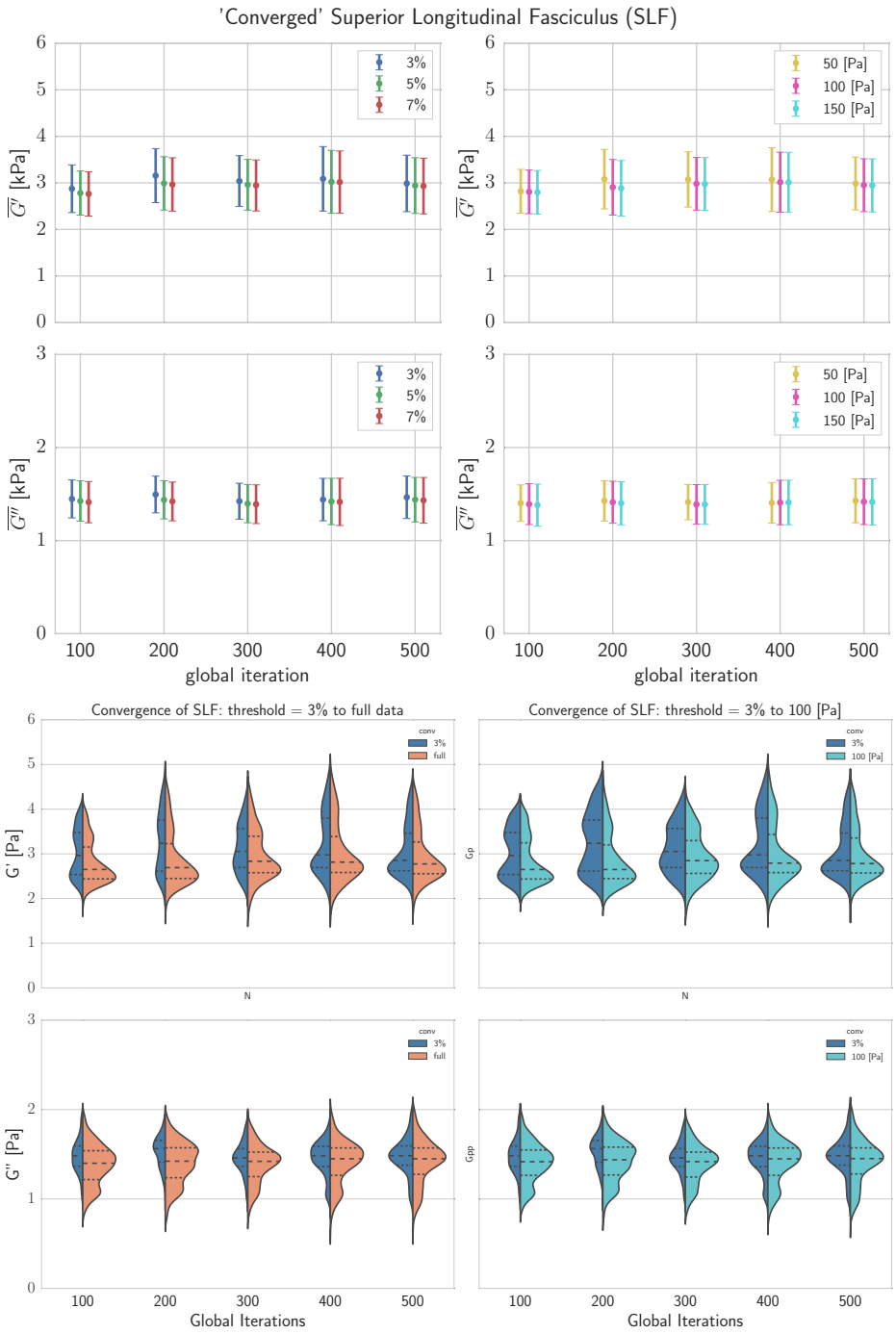

Figure 3.4: Mean and standard deviation of the converged, for both proposed convergence criteria, in the superior longitudinal fasciculus (SLF) at intervals of global iterations. The average moduli for the region does not vary much with iteration (top); however, the distribution of the material properties within the region (bottom) does change with global iterations.

criteria could also be used as effective stopping criteria for the NLI processes, which the algorithm could conditionally iterate until a certain percentage of the imaging volume had successfully converged according to a specified threshold. Finally, when anisotropic models are implemented into NLI, a new convergence criteria will need to be determined based on requirements of sufficient shear strain in each anisotropic plane to ensure accurate and independent material properties [89].

Chapter 4

Multi-Excitation MRE

4.1 Introduction

Neurodegeneration occurring in conditions such as Alzheimer's disease, amyotrophic lateral sclerosis, multiple sclerosis, and normal aging affects macroscale brain tissue characteristics due to microscale tissue changes. The alteration of the neuronal and glial matrix can result in detectable changes in physical material characteristics, including mechanical properties. Magnetic resonance elastography (MRE) is a technique for noninvasively assessing tissue viscoelasticity in vivo [3]. The mechanical contrast afforded by MRE has shown great promise in diagnosing and staging a variety of conditions, most notably chronic liver disease [86, 90], and MRE of the brain has recently revealed softening in a number of neurodegenerative conditions [7, 10, 11, 76, 91, 92].

Despite the success of brain MRE, most common methodological approaches adopt an oversimplified model of the complex tissue behavior that affects the accuracy and precision of the property measures. In particular, MRE typically assumes the material is isotropic, i.e. it does not exhibit direction-dependent properties, despite the fibrous structure of brain tissue, especially white matter (WM). A number of studies on animal brains suggest the necessity of considering anisotropic tissue properties in assessing the brain with MRE [18, 22, 23, 93–95]. For instance, Velardi et al. [96] performed an *ex vivo* axial test of porcine WM and found that when stretched along the fiber direction, stiffness appeared approximately three times greater than when stretched against the fibers. Feng et al. [18] performed shear tests on *ex vivo* lamb brains and found the shear modulus to be approximately 40% greater along

the fiber than against. Similar behavior is expected in human brains given the shared fiber structure.

The adoption of an isotropic material model for brain MRE, despite the evidence supporting tissue anisotropy, is motivated by the need to maintain stability in solving the ill-posed inverse problem. Anisotropic models require additional material parameters to be estimated while enforcing isotropy reduces the burden on the inversion of noisy data. Though recent work has aimed to estimate anisotropic tissue properties with MRE [23, 93–95, 97–100], including specific WM tracts in the brain [22, 38, 74, 76, 101], the effect of WM anisotropy on traditional isotropic inversion schemes has yet to be fully characterized [102].

The present study aims to explore the differences in reconstructed isotropic mechanical properties of the brain in the presence of unique mechanical excitations. We aim to use a multi-excitation MRE setup to generate distinct shear patterns in the brain, and will evaluate our hypothesis that the directionality of shear strain relative to WM fiber orientation influences mechanical property estimation. Local fiber orientation will be determined using diffusion tensor imaging (DTI) in three major WM tracts of interest: corpus callosum (CC), corona radiata (CR), and superior longitudinal fasciculus (SLF).

4.2 Methods

A single 28-year-old healthy male subject participated in this study approved by the University of Illinois at Urbana-Champaign Institutional Review Board after providing written informed consent. The imaging protocol consisted of two MRE scans performed using two separate actuator setups, DTI, and a high-resolution structural acquisition (MPRAGE). All scanning was performed on a Siemens 3T Trio MRI scanner (Siemens Medical Solutions; Erlangen, Germany). Four repeats of the imaging protocol were performed on the same subject. These repeats were collected on different days, spread across four months.

4.2.1 MRE Acquisition

MRE displacement imaging used a 3D multislab, multishot spiral MRE sequence for generating 3D, full vector field complex displacement data at 50 Hz with 2 x 2 x 2 mm^3 isotropic spatial resolution [38]. The specific imaging parameters for MRE include single shot in-plane spiral readout with SENSE $R = 3$; ten slabs of eight k_z sampling planes with 25% slab overlap; $TR/TE = 1800/73$ ms; four (4) temporal phase offsets; and $FOV = 240$ x 240 x 120 mm. Small strains ($\sim 10^{-5}$) in the brain were induced through whole-head vibrations using a pneumatic actuator system (Resoundant, Inc., Rochester, MN). In order to create distinct excitation patterns, two passive drivers are positioned on the patient's head inside of the head coil: a soft pillow-like pad under the posterior of the head (Figure 4.1(a)) and a harder pad on the right side of the head (Figure 4.1(b)). The soft pad is often used for head MRE experiments [**?**, 14] due to its slim profile allowing it to fit comfortably in the standard MRI head coil. Additionally, the position posterior to the head results in good coupling to the skull through the weight of the head. The hard pad was used for the lateral experiment to achieve adequate coupling with the head through contact with both the skull and the side of the head coil. The dimensions of the head coil precluded the use of soft pad for the lateral excitation case. The MRE scan was performed twice with one driver activated for the entire imaging experiment at a time. The actuator driver is switched manually through a connection on the pneumatic tube between scans without altering the head position. As expected, the two excitation directions, referred to as anterior–posterior (AP) and left–right (LR), provide distinct deformation fields in the human brain (see Figure 4.1). In order to ensure optimal contact and sufficiently minimize involuntary movement of the head, foam pads were placed between the head and the MR coil on the subject's left side, and the driver adjacent to the right side of the head and the coil.

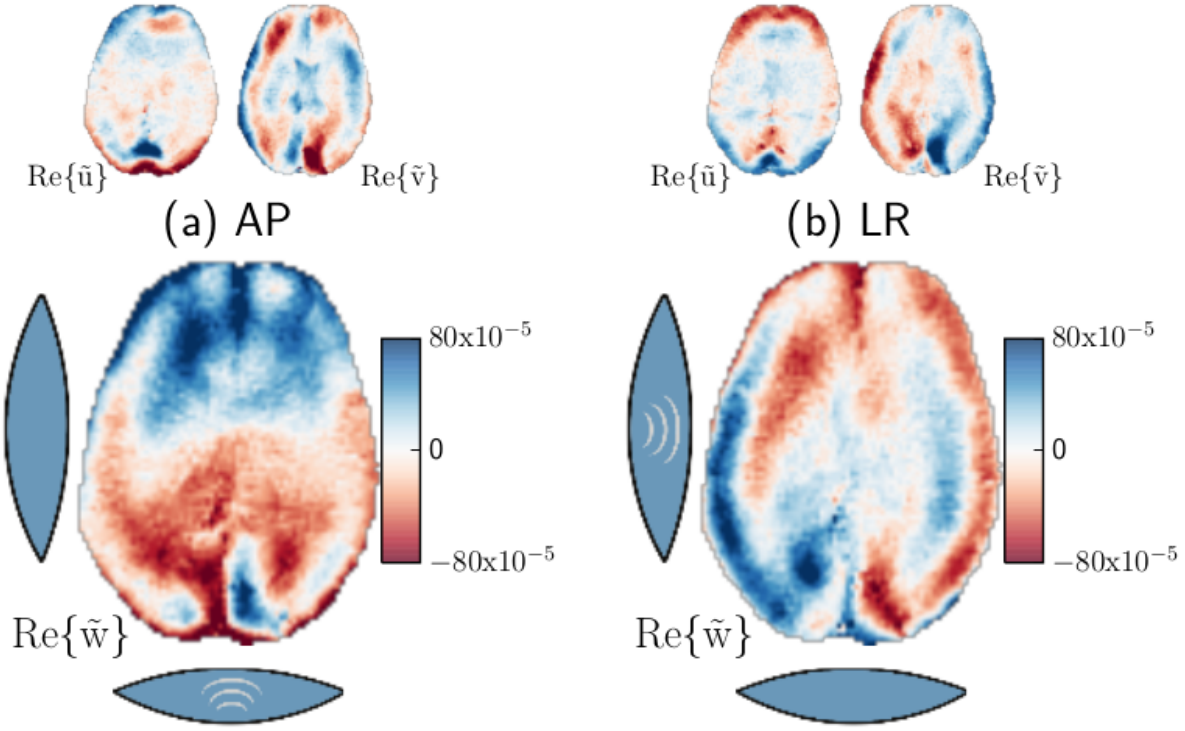

Figure 4.1: The real component of the complex displacement fields ($\tilde{u} = \{\tilde{u}, \tilde{v}, \tilde{w}\}$) generated by excitation from two different actuator setups: (a) anterior–posterior (AP) and (b) left–right (LR). The two excitations produce distinctly different patterns, particularly for the out-of-plane direction. AP excitation results in patterns with left–right symmetry, while the LR excitation exhibits anterior–posterior symmetry, as expected.

4.2.2 Material Property Reconstruction

See section 1.1.1

4.2.3 Other Imaging

DTI data was acquired in the same imaging session in a co-registered fashion with FOV and resolution matched to the MRE data. DTI parameters include: single-shot EPI with GRAPPA $R = 2$; $TR/TE = 8000/95$ ms; 30 non-collinear encoding directions; $b = 1000$ s/mm^2. The diffusion tensor was processed using FMRIB Diffusion Toolkit (FDT) [84] to extract the voxel-wise diffusion eigenvectors. Finally, we acquired a T_1-weighted structural image using an MPRAGE sequence, which resulted in a 0.9 x 0.9 x 0.9 mm^3 isotropic resolution ($TR/TI/TE = 2000/900/2.2$ ms).

4.2.4 Analysis

Computing Strain

First the strain is calculated from MRE displacement fields to investigate the strain at each voxel to better understand how the strain state is related to the reconstructed properties from NLI between the two excitation directions. Isotropic tissue will behave the same under different shear modes; conversely, anisotropic material will respond differently in each independent property direction. The strain is computed from the MRE displacement at each temporal phase offset via

$$\varepsilon_{ij}(x_k, t_n) = \frac{1}{2}\left(u_{i,j} + u_{j,i}\right)(x_k, t_n) \tag{4.1}$$

where x_k is the spatial coordinate and t_n is the time at point n. The strain tensor is symmetric, and thus can be written as

$$\frac{1}{2}\left(u_{i,j}+u_{j,i}\right)(x_k,t_n) = \\ = \begin{bmatrix} u_{11} & \frac{1}{2}\left(u_{12}+u_{21}\right) & \frac{1}{2}\left(u_{13}+u_{31}\right) \\ \frac{1}{2}\left(u_{21}+u_{12}\right) & u_{22} & \frac{1}{2}\left(u_{23}+u_{32}\right) \\ \frac{1}{2}\left(u_{31}+u_{13}\right) & \frac{1}{2}\left(u_{32}+u_{23}\right) & u_{33} \end{bmatrix}(x_k,t_n) = \\ = \begin{bmatrix} \varepsilon_{11} & \varepsilon_{12} & \varepsilon_{13} \\ \varepsilon_{12} & \varepsilon_{22} & \varepsilon_{23} \\ \varepsilon_{13} & \varepsilon_{23} & \varepsilon_{33} \end{bmatrix}(x_k,t_n), \quad (4.2)$$

The root-mean-square (RMS),

$$\varepsilon_{rms,ij}(x_k) = \sqrt{\frac{1}{N_t}\sum_{n=1}^{N_t}\left[\varepsilon_{ij}(x_k,t_n)\right]^2}, \quad (4.3)$$

is computed to obtain a magnitude of the oscillatory shear and normal strains across the temporal phase offsets. Maps of the RMS values for the shear components of the strain tensor are shown in Figure 4.2. It is important to note the strain calculations were performed independent from NLI to reduce bias from the specific NLI formulation.

Fiber-Tract Reference Frame

NLI is formulated with respect to the imaging reference frame, and all inversions in this work are completed in this reference frame. However, we seek to understand how isotropic MRE reconstructions of an expected anisotropic material, and thus we want to compute the strain state relative to the direction of neuronal fiber bundles, which represent the presumed axis of symmetry in a transversely isotropic material [22, 94]. The strain tensor at each voxel, Eq. (4.1), can be transformed from the lab (imaging) reference frame of the MRE images,

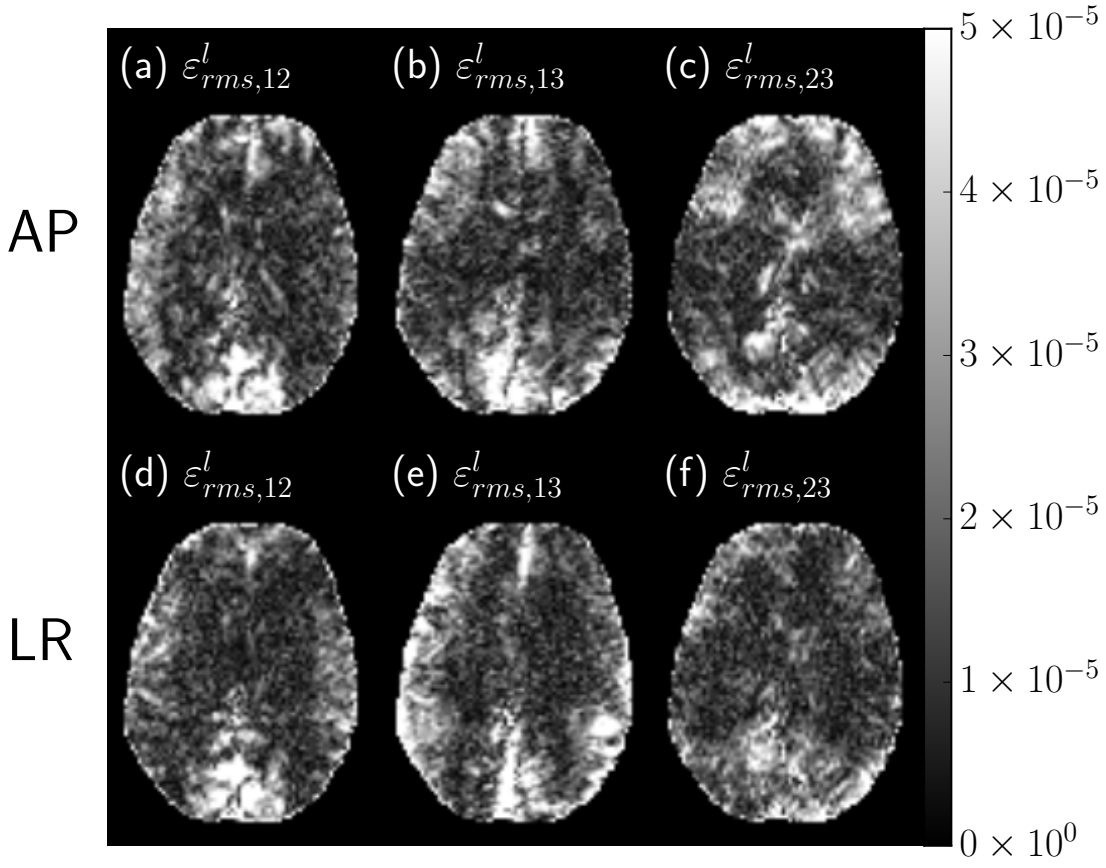

Figure 4.2: The RMS shear strain components of the strain tensor from both the anterior-posterior (AP) and left-right (LR) excitations. There are similar high magnitude regions for each direction but, also, distinct differences where the excitation was applied to the subject's head.

$\hat{x}^l$, into the axonal fiber-tract reference frame, $\hat{x}^f$, by constructing a transformation matrix from the DTI eigenvectors (V_j). The DTI eigenvectors, assumed to be the fiber orientation reference frame in typical DTI, are the local coordinate system of the voxel, where $\hat{x}^f_j = V_j$ and $\hat{x}^f_1$ corresponds to the principal fiber direction, while $\hat{x}^f_2$ and $\hat{x}^f_3$ correspond to the two directions perpendicular to the fiber-tracts. The transformation tensor is constructed via the cosine of the angle between the lab and fiber coordinates:

$$[T] = \cos(\hat{x}^l_i, \hat{x}^f_j). \tag{4.4}$$

The transformation of the strains in the lab coordinates into the fiber-tract's local orientation is then computed for each time point

$$[\varepsilon^f] = [T^T][\varepsilon^l][T] \tag{4.5}$$

and the RMS of strain is calculated in the same fashion as in section 4.2.4. In order to highlight the asymmetry of shear strains relative to fiber-tracts and thus the likely anisotropic response, the shear strains in planes *parallel*, ε^f_{12} and ε^f_{13}, and *perpendicular*, ε^f_{23}, to the dominant fiber direction, $\hat{x}^f_1$, are compared via

$$\varepsilon_{\parallel/\perp} = \frac{\frac{1}{2}(\varepsilon^f_{12} + \varepsilon^f_{13})}{\varepsilon^f_{23}}. \tag{4.6}$$

The spatial, multiple experiment averages of Eq. (4.6) are computed for various regions of the brain in Table 4.3, with $()^*$ indicating statistically significant differences determined by a paired t-test.

Registration

The images from a given scanning session are acquired in a co-registered fashion (both MRE and DTI scans). The DTI acquired during each experiment is used to register these

data for identifying the WM regions of interest through an atlas [103] using the FSL TBSS tool [104]. The WM tracts investigated in this study are the corpus callosum (CC), corona radiata (CR), and superior longitudinal fasciculus (SLF). Additionally, the FAST tool in FSL [105] segmented the MPRAGE to delineate the global WM region from the images for comparison with the individual tract (CC, CR, and SLF) statistics.

4.3 Results

An example of the differences in displacement fields for a subject undergoing two different excitations is shown in Figure 4.1. The displacement fields show a different displacement pattern for each excitation, particularly for the out-of-plane direction. AP excitation results in patterns with left–right symmetry, while the LR excitation exhibits anterior–posterior symmetry, as expected. The uniqueness of patterns is indicative of differentially excited shear modes, which results in distinct strain fields, and the distinct fields are necessary for investigating direction-dependent responses. Displacement fields from both AP (soft pad) and LR (hard pad) excitation were of sufficiently high quality for inversion, with octahedral shear strain-based SNR (OSS-SNR) for all displacement fields greater than 3 [87].

Figure 4.2 shows the RMS strain of the displacement field for the same axial slice as in Figure 4.1. At the posterior of the subject's head, both excitation directions have the strongest strain magnitudes due to the shear source at the skull and falx. However, the strain throughout the brain has voxel-wise spatial variation differing with excitation direction, especially as the shear propagates towards the center. The AP excitation shows the outline of the ventricle region in each of the strain components, which is less visible in LR excitation. The lack of definition in strain patterns for LR at the center may be due to the excitation wave passing across the long side of the ventricles.

Figure 4.3 presents an example of the reconstructed material property maps for the storage (G') and loss (G'') moduli at an axial slice encompassing regions adjacent to the lateral

Table 4.1: Summary of mean and standard deviation for the reconstructed storage modulus, G', across experimental repeats of spatial averages of the whole brain, global WM, and selected WM regions (CC, CR, and SLF); $()^*$ represents $p < 0.05$ for the normalized differences; $\overline{(,)}$ is a two value average.

Measure	Whole Brain	WM	CC	CR	SLF
$\overline{G}'_{AP}$	2.45 (1.1%)	2.68 (1.2%)	2.24 (1.3%)	3.03 (1.6%)	2.85 (1.9%)
$\overline{G}'_{LR}$	2.48 (1.6%)	2.74 (1.7%)	2.81 (4.2%)	3.32 (5.7%)	2.82 (5.2%)
$\frac{(\overline{G}'_{AP}-\overline{G}'_{LR})}{\overline{(G'_{AP},G'_{LR})}}$	-1.2%	-2.2%	-23%*	-11%	1.3%

Table 4.2: Summary of mean and standard deviation for the reconstructed loss modulus, G'', across experimental repeats of spatial averages of the whole brain, global WM, and selected WM regions (CC, CR, and SLF); $()^*$ represents $p < 0.05$ for the normalized differences; $\overline{(,)}$ is a two value average.

Measure	Whole Brain	WM	CC	CR	SLF
$\overline{G}''_{AP}$	1.07 (2.0%)	1.22 (2.3%)	1.04 (4.6%)	1.49 (3.1%)	1.61 (5.3%)
$\overline{G}''_{LR}$	1.08 (1.8%)	1.25 (2.8%)	1.32 (6.9%)	1.84 (7.1%)	1.56 (5.1%)
$\frac{(\overline{G}''_{AP}-\overline{G}''_{LR})}{\overline{(G''_{AP},G''_{LR})}}$	-0.91%	-2.9%	-26%*	-33%*	4.3%

ventricles, the CC, and the CR. Note that the change of excitation orientation results in voxel-wise differences in G' and G'' of up to approximately 2 kPa. Such large differences between the AP and LR excitation appear mostly in areas with high DTI fractional anisotropy (FA): $\overline{FA}_{CC} = 0.70$, $\overline{FA}_{CR} = 0.51$, and $\overline{FA}_{SLF} = 0.50$.

A summary of the mean and standard deviation of reconstructed G' and G'' moduli across the repeated experiments for the entire brain, global WM, CC, CR, and SLF are given in Tables 4.1 and 4.2. Values are reported for each excitation and the relation between the two, with $()^*$ indicating statistically significant differences determined by a paired t-test. The whole brain averages for G' and G'' for both excitation directions are consistent with published values and exhibit very low standard deviations across repeated experiments ($\leq 2\%$), indicating excellent reproducibility, in agreement with other brain MRE studies using NLI [**?**, 106]. Similarly, the global WM region exhibits consistent G' and G'' between excitations and comparable reproducibility.

Additionally, both global regions exhibit comparable and reproducible ratios of shear

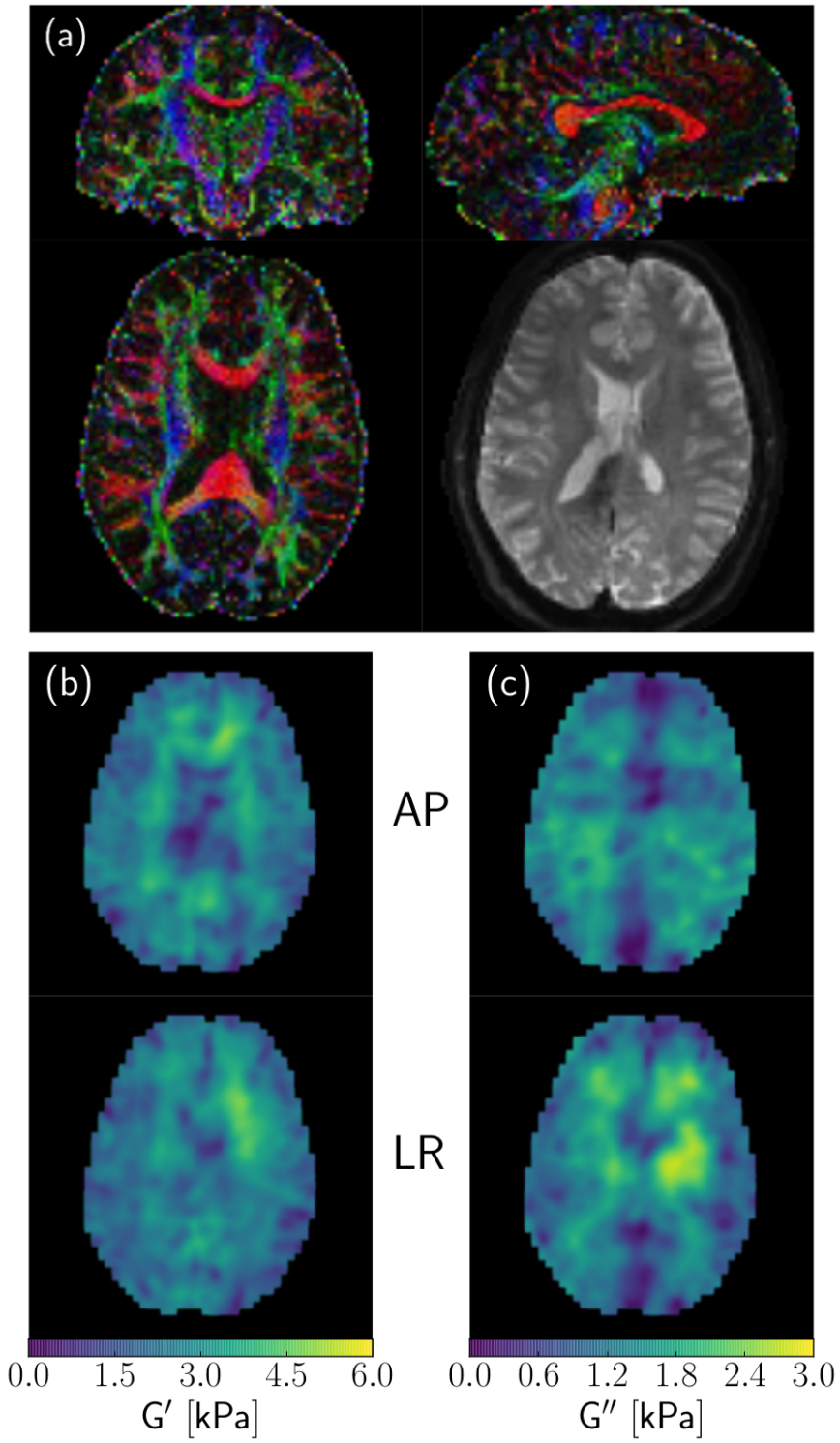

Figure 4.3: (a) Fractional anisotropy (FA, color intensity) from DTI (from top-left) coronal, axial and sagittal, where colors describe the fiber-tract's dominant direction: red indicates left-right, blue indicates inferior-superior, and green indicates anterior-posterior; bottom-right is a sagittal magnitude image from MRE data. The reconstructed (b) G' and (c) G'' material maps for anterior–posterior (AP, top) and left–right (LR, bottom) excitations. Significant differences in reconstructed values are easily identified.

Table 4.3: Summary of mean and standard deviation for the computed fiber-tract shear strain ratio, $\overline{\varepsilon}^f_{\parallel/\perp}$, across experimental repeats of spatial averages of the whole brain, global WM, and selected WM regions (CC, CR, and SLF); $()^*$ represents $p < 0.05$ for the normalized differences; $\overline{(,)}$ is a two value average.

Measure	Whole Brain	WM	CC	CR	SLF
$\overline{\varepsilon}^f_{\parallel/\perp,AP}$	1.61 (0.23%)	1.62 (0.23%)	1.34 (2.3%)	1.62 (1.3%)	1.56 (8.0%)
$\overline{\varepsilon}^f_{\parallel/\perp,LR}$	1.59 (0.54%)	1.56 (0.30%)	1.66 (9.0%)	1.47 (3.3%)	1.44 (6.1%)
$\frac{(\overline{\varepsilon}^f_{\parallel/\perp,AP} - \overline{\varepsilon}^f_{\parallel/\perp,LR})}{\overline{(\varepsilon^f_{\parallel/\perp,AP}, \varepsilon^f_{\parallel/\perp,LR})}}$	1.3%	3.4%	-22.3%*	8.8%*	7.5%

parallel to perpendicular with respect to dominant fiber-tracts direction, $\varepsilon^f_{\parallel/\perp}$ (Eq. (4.6)), as summarized in Table 4.3. This is expected as the global regions do not isolate specific, ordered fiber-tracts.

The spatial mean values for G' and G'' in each WM tract for each experiment are plotted in Figure 4.4 against the spatial mean values for $\varepsilon^f_{\parallel/\perp}$. The CC shows the largest difference between reconstructed G' and G'', 23% and 26% on average, for the two excitation experiments. Both G' and G'' are greater in LR excitation experiments, which corresponds to a greater $\varepsilon^f_{\parallel/\perp}$. The CR similarly exhibits greater G' and G'' in LR excitation; although, in contrast, there is a slight decrease in $\varepsilon^f_{\parallel/\perp}$. The SLF shows no discernible difference in either G' or G'', potentially due to the variability of $\varepsilon^f_{\parallel/\perp}$ in both LR and AP excitations.

4.4 Discussion

The AP and LR excitations each provide distinct deformation states in the human brain, as evidenced by both the displacement fields (Figure 4.1) and the computed RMS shear strain fields (Figure 4.2). The unique strain fields are a necessary start for characterizing how MRE interprets shear strain applied to anisotropic media. The discrepancies (locally over 2kPa) in reconstructed G' and G'' (Figure 4.3) show the inherent limitation of the isotropic assumption used for the NLI material model when investigating anisotropic media.

The mean and standard deviation statistics (Tables 4.1, 4.2, and 4.3) for results in the

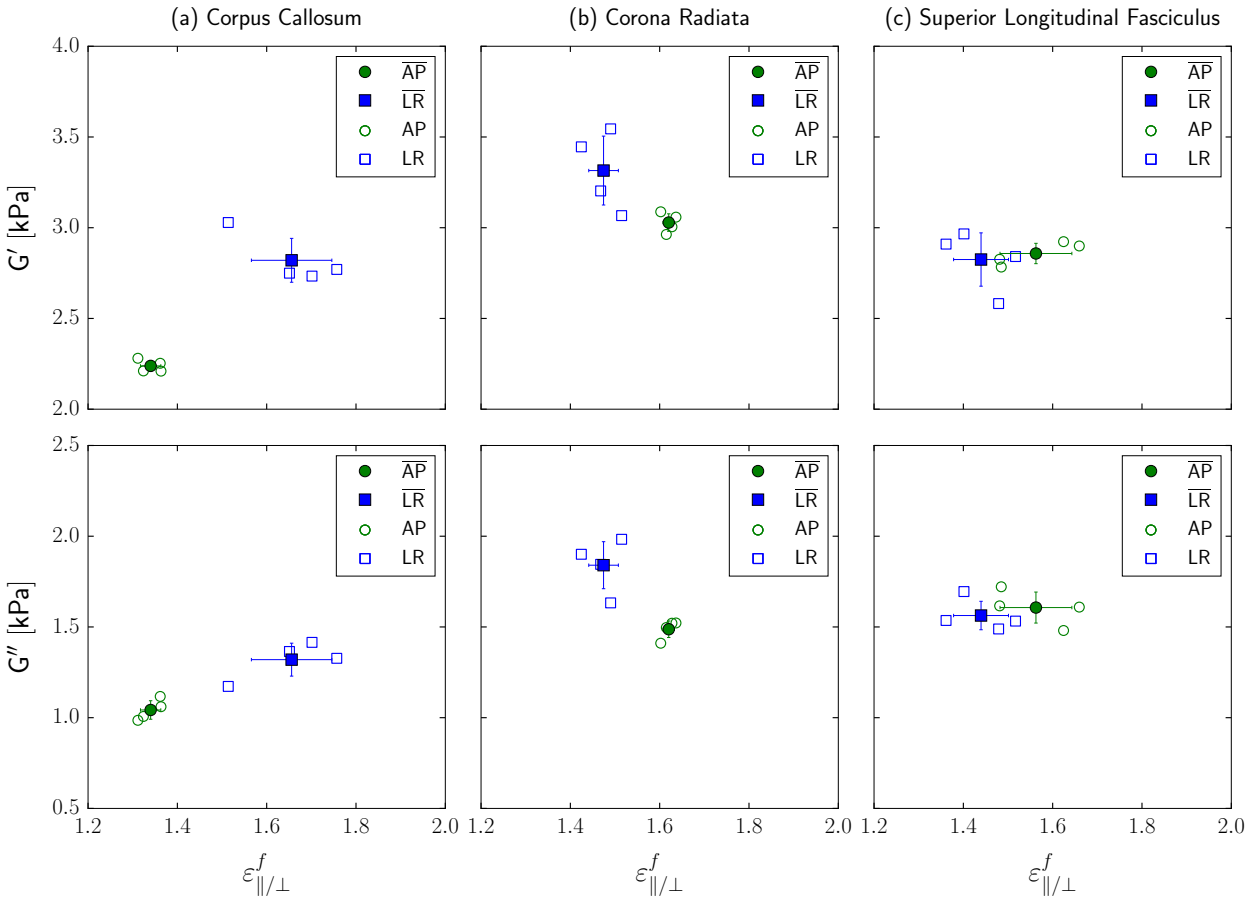

Figure 4.4: Comparison of reconstructed isotropic material properties, G' and G'', with the strain ratio of shear *parallel* to shear *perpendicular* to fibers in the fiber-tract reference frame $\varepsilon^f_{\parallel/\perp}$ (Eq. (4.6)) for (a) corpus callosum, CC, (b) corona radiata, CR, and (c) superior longitudinal fasciculus, SLF. The numerical values of mean and standard deviations across experimental repeats are presented in Tables 4.1, 4.2, and 4.3.

whole brain, global WM, and individual WM regions (CC, CR, and SLF tracts) help provide initial context for the local effect of shear strain mode on the reconstructed material properties. The differences between excitation for global G', G'', and shear strain ($\varepsilon^f_{\parallel/\perp}$) are $< 1.5\%$ across all repeats. The findings for global WM are similar, with non-significant differences of $< 3.5\%$ between excitations.

Significant differences in reconstructed material properties occur in areas of the highest local anisotropy, as well as the greatest difference in shear strain ratio. The $\varepsilon^f_{\parallel/\perp}$ in the CC differed between the two excitations by 22.3% (normalized) and both the reconstructed G' and G'' had over 20% normalized difference, 23% and 26%, respectively. The stark difference in properties in the CC is not surprising, as the CC has a highly aligned, well-ordered fiber structure [107] known to exhibit mechanical anisotropy [96, 108], and the two excitation fields provide sufficiently different strain states expected to illuminate direction-dependent properties in MRE. This is highlighted by Figure 4.4(a), where the CC properties show a linear increase in both G' and G'' with increasing $\varepsilon^f_{\parallel/\perp}$. In other words, the tissue appears stiffer when exposed to strains in planes parallel to the dominant fiber axis. This apparent relationship suggests that as the disparity in axonal shear components changes, the isotropic MRE inversion effectively "sees" a different underlying material.

The relationship between excitation mode and reconstructed MRE properties is less clear in the CR. In this case, we found a much smaller difference in shear strain ratio between excitations (8.8%). This translated in to a small, non-significant difference in G' (11%), but a large, significant difference in G'' (33%). Most interestingly, the apparent relationship between G' and G'' in the CR with $\varepsilon^f_{\parallel/\perp}$ (Figure 4.4(b)) is opposite from that of the CC in that G' and G'' decrease with increasing $\varepsilon^f_{\parallel/\perp}$. How the magnitude and the relationship between MRE properties and strain state in the CR differs from those in the CC may be explained by the more complex fiber structure of the CR. The CR encompasses fibers that fan in the superior-inferior direction as they approach the cortex, and also include populations of crossing fibers. The disparity in fiber structure has been previously used to understand

MRE properties in the CC and CR [38], and may be underpinning the relationships reported here.

We did not observe differences in G' and G'' for the SLF, even though the SLF is also a large, well-ordered WM tract. We believe that the lack of significant differences in MRE properties between excitation is due to the strain fields themselves not being significantly different. The values for $\varepsilon^f_{\parallel/\perp}$ in the SLF exhibited higher standard deviations across repeats, even though the AP excitation had shown high reproducibility in other measures. This, in turn, resulted in poorer reproducibility of G' and G'' measures in the SLF that likely contributed to the lack of detectable significant difference. This suggests the strain fields towards the periphery of the brain generated by both excitation directions are very sensitive to the excitation mode, but that they are associated with consistent shear modes in the deeper WM regions.

The scenario of applying unique shear modes to characterize anisotropic material is similar to applying any type of mechanical tests with forcing in different directions, and has previously been used in MRE experiments on phantoms to characterize anisotropic effects [19–21, 109]. In these works, the shear direction is carefully controlled and applied either along or against the known directions of material symmetry. In the brain, such control over shear direction is not feasible due to poor mechanical transmission through the skull, and also because the material anisotropy is itself spatially varying. In this work, we use two distinct excitation directions and achieved success in generating shear modes sensitive to material anisotropy in two large WM tracts, the CC and the CR, and not in another, the SLF. Future works could incorporate more excitation modes to better capture the behavior of all WM regions in the brain and studies to identify commonalities in WM behavior across a population.

Anisotropic MRE inversion schemes may benefit from adopting a multi-excitation approach. Previous anisotropic methods have aimed to reconstruct direction-dependent mechanical properties from a single deformation field through the incorporation of prior knowl-

edge of material symmetry [22, 23, 93, 94, 97]. While the results from these methods appear promising [74, 95, 110], they may suffer in characterizing the heterogeneous anisotropy of the human brain if the excited shear mode is not judiciously chosen to account for material symmetries and sensitive to the material complex properties. By incorporating multiple excitation fields with sensitivities, anisotropic inversions may be stabilized during the reconstruction of multiple material constants. For example, two studies performed controlled actuation on numerical phantoms [21], physical phantoms, and *ex vivo* tissue [20]. Both studies are important to anisotropic MRE because they show how a three parameter incompressible transversely isotropic material model can capture more information than the typical transversely isotropic model, including fiber stretch. The work in this study, in contrast, did not take into account the polarization of shear waves, but, as we move to higher order models, we should be careful to consider the potential effects of fiber stretching.

Finally, it is important to consider the implications of our findings on the interpretation of MRE results in WM tracts from traditional, single-frequency experiments. While we report that excitation mode and the amount of shear strain parallel and perpendicular to the plane containing the dominant fiber direction can result in significant differences in estimated mechanical properties, we also note that results from the AP excitation alone are very repeatable. AP excitation is the most common type of excitation used in brain MRE, generally achieved through pneumatic actuation of a soft pillow [7, 111] or a head rocker driven by remote electromechanical actuation [**?**, 38, 112]. LR excitation from a bite bar [113–115], lateral pneumatic actuation [116], or scanner table vibration [117] is less commonly employed. In this case, we can expect that the use of AP excitation will result in highly repeatable measurements of WM tracts, as has been reported previously [**?**, 38], and that these measurements should be considered less sensitive to the excitation mode.

4.5 Conclusions

Material testing of animal brains has shown the mechanical anisotropy of brain tissue is significant and the human brain is expected to exhibit similar anisotropic properties. However, MRE methods have typically adopted an isotropic material model for considering the brain, thus ignoring direction-dependent material properties expected to be present in WM. In this study, we performed multi-excitation MRE experiments and observed distinct differences in reconstructed isotropic material properties of well-ordered WM tracts due to excitation of unique shear modes. The differences arise from the anisotropic medium being sheared in different directions and the isotropic reconstruction "seeing" different properties depending on whether the material is sheared in planes parallel or perpendicular to the fibers. Through the use of both AP and LR excitations, we observed differences in reconstructed MRE properties, G' and G'', of up to 33% in WM tracts, while finding no difference in global properties. These findings have implications for future experiments and methodological developments targeting the reconstruction of anisotropic mechanical properties of WM, and may provide additional contrast for elucidating microstructural processes of neurodegeneration.

Chapter 5

Aging Human Brain Mechanics

5.1 Motivation

The aging process, post-development, affects human brains in a number different ways and, unfortunately, is often associated with the onset of neurodegenerative diseases. The focus of this work is on the changes in mechanical properties of the brain during healthy aging. MRE has shown significant promise in its sensitivity to both changes within healthy brains and identifying biomarkers in diseased brains. This study builds on previous MRE aging research [**?**, 76, 78] and adds higher-resolution, full-coverage MRE imaging, and the ability to identify tissue anisotropy, or lack thereof, utilizing the multi-excitation (ME-MRE) experimental protocol. ME-MRE is important for capturing relative anisotropy measures, which are known to exist in most WM regions. The regions considered in this study are corpus callosum (CC), corona radiata (CR), and superior longitudinal fasciculus (SLF). Bayly and colleagues have seen strongly anisotropic material properties in *ex vivo* and *in vivo* WM in animal brain sections [118,119]. WM regions are important for understanding healthy aging in at least two ways: (*i*) these are the regions where both the microinfarcts and neurodegeneration appear with age (WM hyperintensities), so improved biomarkers will allow for differential diagnosis and the development of baseline characteristics for early diagnosis of neuro-pathologies; (*ii*) the functional organization of WM changes with age in a more protected way relative to cortical grey matter. The long-distance connectivity decreases but the local connectivity increases [120] and "high-performing" older adults tend to have more bilaterialization, via CC [121].

Previous studies using MRE have shown the mechanical properties of the healthy aging human brain change with age [**?**, 78], but not all areas by the same amount [76]. DTI literature has shown diffusion anisotropy measures tend to peak around the age of 30-35 years old and decrease with age [57–60]. This study is unique in both higher resolution, full brain MRE imaging, necessary for regional comparisons, and capturing age related changes in anisotropy, expected from DTI, using an isotropic material estimation via the multi-excitation experiment [122]. During an overlapping time period, another aging study focusing on grey matter was performed by Hiscox and colleagues using similar imaging sequences and NLI inversion, but it did not perform the multi-excitation protocol [75]. The Hiscox et al. study is an important reference for this work in it's overall trends in both standard structural (MPRAGE) information and material properties with age (NLI-MRE). The present study focuses on white matter and on the relative anisotropy differences within the entire cohort and across two age groups.

The multi-excitation experiment protocol allows for illumination of the tissue from distinctly different directions; however, the pad lateral to the head is designed for liver MRE, requires extra padding, and the resulting excitation fields are sensitive to placement. All of these factors make it more difficult to get reliable measurements for single subjects. The first multi-excitation experiments (Chapter 4) were based on repeated imaging of a single subject knowledgeable with the MRE process, thus increasing quality of the results (i.e. proper pad placement and OSS-SNR). If multi-excitation is used in future studies, then it will be necessary to characterize and standardize the protocol, or even create specialized hardware, for more robust experimental results. The ultimate goal of the ME-MRE approach is to extract sufficient information from a single standard, AP-excitation MRE experiment for wider applicability in clinical workflows.

5.2 Imaging & NLI Estimation

The experiment from a previous study [122] (Chapter 4) was repeated with thirteen (13) young and twelve (12) older adult male subjects, with acceptable results from young for AP = 9, LR = 8, AP & LR = 7 (24-32 years old); and older subjects for AP = 7, LR = 5, AP & LR = 4 (55-75 years old).

5.2.1 MR Imaging

The MRE displacement imaging employed a 3D multislab, multishot spiral MRE sequence for generating 3D, full vector field complex displacement data at 50 Hz with $2 \times 2 \times 2$ mm^3 isotropic spatial resolution [37]. The multi-excitation experiment includes anterior-posterior (AP) excitation MRE (applied at posterior of the head, near the occipital region of the skull) and left-right (LR) excitation MRE (applied on right side near temple). Additionally, matched field-of-view and resolution (relative to MRE) diffusion tensor imaging (DTI) and T1-weighted MPRAGE structural image at $0.9 \times 0.9 \times 0.9$ mm^3 isotropic resolution (TR/TI/TE = 2000/900/2.2 ms) were acquired. MPRAGE is used to register the subjects to the MNI JHU white matter (WM) atlas for regional-level analysis [123].

5.2.2 NLI Material Property Estimation

The NLI material estimation framework, used throughout this dissertation work, was applied for each subject and each excitation direction independently. NLI has the capability to combine multiple displacement fields for estimation by minimizing the displacement error across both fields; however, this is implemented primarily for multi-frequency estimations [35] and has not shown to be a direct way to improve understanding for multi-excitation. The NLI parameter study (Ch. 2) and convergence criteria (Ch. 3) provided specific justifications for inversion parameters and tools for determining "goodness" of estimations. Chapter 2 guided our understanding of parameter (in)dependence for a single subject and looks to examine the

applicability across a larger population. Chapter 3 demonstrated two convergence criteria that can be used to remove poor quality material property values from regional averages to improve the quality of comparisons.

The NLI estimation was performed on the cohort for two different procedures: first, termed "Classic" signifying parameters used in previous studies, and the second, termed "Converged Cascade" signifying the "cascade" CG iteration structure (outlined in Table 2.3) with a convergence criteria applied at the end. The subzone size was kept at the previous size for both cases, side-length of $0.84L_s$ ("standard" size) from Ch. 2, because it is expected to minimally affect estimations and allowed for running NLI to much higher global iterations ($N_g = 400$) than larger subzones would permit. For convergence criteria, the "normalized percent variation" convergence threshold (Eq. 3.2) was used on the last ten (10) iterations with a value of $\%_{threshold} = 5\%$. Comparisons between the two cases will be shown for all of the results for a clear comparison of potential benefits from the changes.

5.3 Analysis

5.3.1 Strain in DTI-frame

The measured displacement for the two excitations (AP and LR) were used to compute the strain fields inside the subject and transformed into the local DTI-frame, as presented in Section 4.2.4. The analysis is repeated in this study as an extension beyond the single-subject study and as the initial examination of the hypothesis that increasing age decreases mechanical WM anisotropy.

5.3.2 *in vivo* Simple Shear

Using the DTI information and the MR measured displacement fields, assuming the tensors indicate dominant macroscale behavior, it is straight forward to identify voxels consisting of

nearly independent shear either in axial or transverse orientations. These voxels represent regions where the strain is as close to the benchtop experiments one would ideally want to perform to characterize an anisotropic medium. As a way to understand the disparity in the applied strain field, and subsequently observed in the estimated moduli, the relative shear in each voxel and each experiment, is compared against a threshold:

$$\frac{\varepsilon_{\parallel}}{\varepsilon_{\perp}} > \varepsilon_{SS} \quad \text{or} \quad \frac{\varepsilon_{\parallel}}{\varepsilon_{\perp}} < \frac{1}{\varepsilon_{SS}} \tag{5.1}$$

where ε_{SS} is the pre-defined threshold for identifying these cases of simple shear. A threshold of $\varepsilon_{SS} = 5$ seems both a reasonable disparity and provided a useful sample of voxels. Identifying simple shear at a voxel level affords the opportunity to observe two phenomena: waveguiding and material property bounds. The waveguide effect within well-ordered fiber bundles is well known [22, 23] and multi-excitation experiments can indicate if this effect occurs regardless of excitation or only in particular excitation cases. Additionally, isotropic reconstructions of an anisotropic tissue experiencing only a specific simple shear condition are expected to provide bounds for the axial and transverse shear moduli of the anisotropic material, given axial or transverse simple shear conditions, respectively.

5.3.3 Analytical Solution for Transversely Isotropic Material

The 1D simple shear wave equation analysis in Section 2.1.1 was used to help explain how domain size, and by extension subzone-size, affected NLI estimations (Chapter 2). The analytical solutions is reused here to help understand how NLI handles the anisotropic tissue as heterogeneously isotropic material by creating a transversely isotropic analytical displacement solution. The solution is created by defining material properties in two orthogonal shear planes and computing the relative contribution of the two displacement fields based on the angle of applied shear. The angle of applied shear starts along the "softer" moduli ($G = 2 + i1$ [kPa]) for $\theta = 0$ and rotated until only applied to "stiffer" moduli

	CC	CR	SLF
$\overline{\Delta \text{FA}}$	-0.59	-0.17	-0.30
$\overline{\Delta \text{RD}}$	0.3	-0.08	-1.0^{**}

Table 5.1: Summary of the average changes with age for DTI metrics: FA and RD. All values are average relative changes per year. Fractional anisotropy (FA): [10^{-3}] and radial diffusivity (RD): [10^{-3}mm^2/s].

($G = 3 + i1.5$ [kPa]) for $\theta = 90$. The plane parallel and opposite to the applied shear is kept "fixed" ($\vec{u} = \vec{0}$), similar to a linear shear rheometer. The domain is a cubic with 1[mm^3] resolution and amplitude of applied displacement of $u_0 = 5 \times 10^{-4}$. The displacement field is used as the input to NLI, analogous to "measured" MRI displacement, and a single-subzone estimation is performed. The goal is to observe the large scale estimation of the anisotropic tissue in NLI towards gaining a better understanding of estimations of anisotropic tissues *in vivo*. The reported values are averages across the domain with CG iteration and angle (θ). Further details, the "shear-free" case, and example elastograms are show in Appendix A.

5.4 Results & Discussion

5.4.1 Aging Trends in DTI and MRE Metrics

The aging literature has been dominated by DTI-focused studies of WM tissue structure [57–60, 121]. The goal with this study is to build on previous literature, by finding common trends in DTI and observe MRE trends within the same regions. The small cohort here indicates good agreement with the established DTI literature, see Table 5.1 and Figure 5.1.

Specifically, the average decrease in FA for CC and increase for RD in CC match quite well with Davis et al. [57]: $\Delta FA_{CC} \approx (0.04 - 0.05)$ and $\Delta RD_{CC} \approx 0.05$ [10^{-3}mm^2/s]. The DTI statistics were from across the set of subjects with a suitable MRE experiment, either AP- or LR-excitation. From the perspective of MRE, it is important to both find common trends, where mutual data brings increased confidence, and test where MRE metrics are

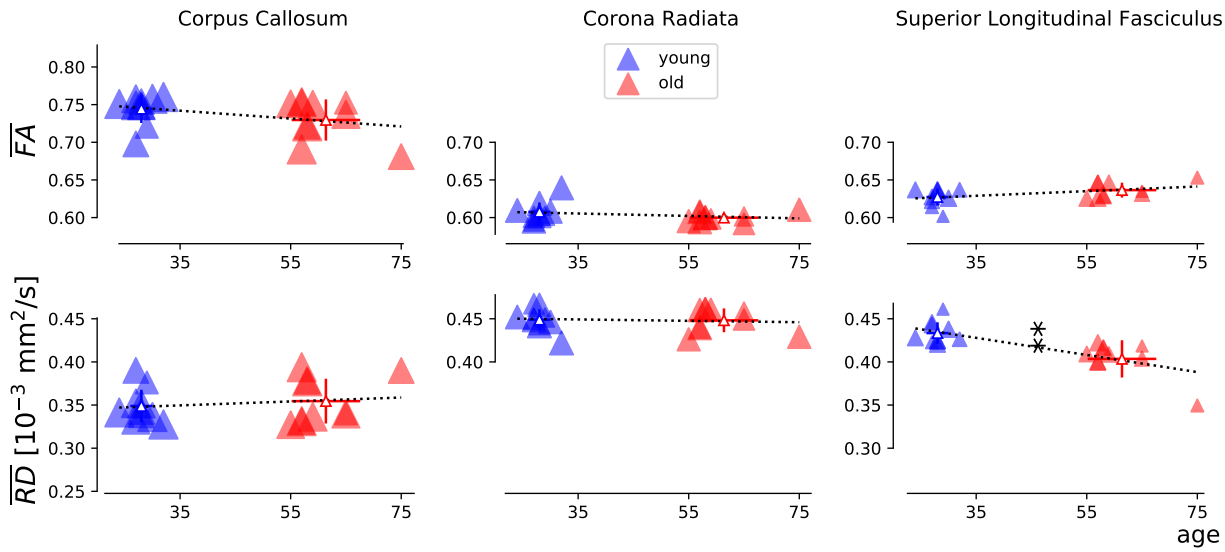

Figure 5.1: Regional white matter (WM) averages of DTI measures, fractional anisotropy (FA) and radial diffusivity (RD), typically most sensitive to aging changes in the human brain. RD_{SLF} is the only significant group-wise difference (** = $p < 0.05$). Size of points indicates relative number of points used in the statistic.

more sensitive to aging.

Overall, normal aging is a diffuse process which alters the brain, globally and within WM and GM regions, leading to a decrease in storage modulus (G') and an increase in loss modulus (G''), as observed in the elastograms in Figure 5.2. For standard AP-excitation NLI estimations, G' shows an overall slight decrease with age for the selected white matter (WM) regions (CC, CR, and SLF), see Figure 5.3. Additionally, G'' shows little change with age for CC and CR but increases for SLF. The average change in properties with age for "Classic" NLI-MRE are summarized in Table 5.2. The rates of decrease are lower than previously reported for other brain regions ([78] = -7.5 Pa/year and [76] = -11 Pa/year), but it is likely caused by the split in a "stiff" and "soft" group within the young subjects, see Figure 5.3. The only study reporting G'' values shows a decrease with age [**?**]. The LR-excitation, in contrast, is more sensitive to changes with age than AP-excitation. The average changes are significant for G' and μ_{stiff}. There seems to be more subject variation, young and old, for G' than G'' for all of the regions. G' decreases with age for all three regions, but it decreases

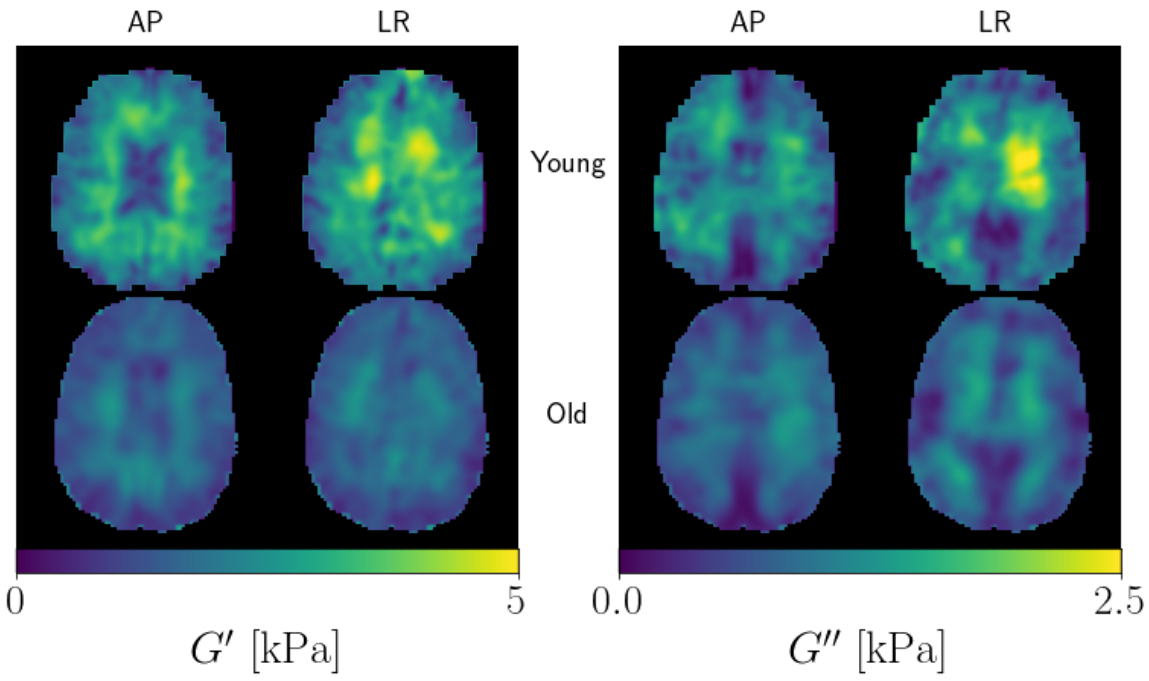

(a) "Classic"

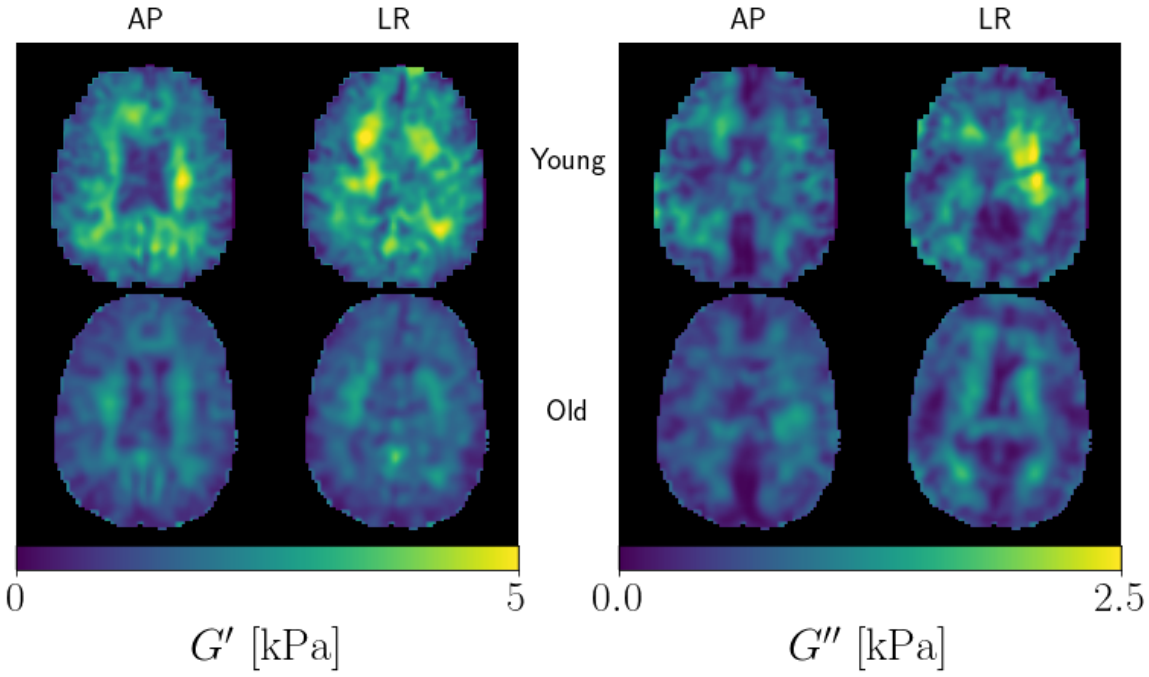

(b) "Cascade" (no convergence criteria applied)

Figure 5.2: Example material property reconstructions of a young and old subject for both AP and LR excitations and both NLI estimations. It is easy to see the young subject, overall, has higher G' and G'', and qualitatively, the AP and LR maps are most different at the interior of the brain. The "Converged Cascade" shows a higher contrast as compared with "Classic" elastograms.

		CC	CR	SLF
$\overline{\Delta G'}$ [Pa]	AP	-2.2	-1.1	-1.2
	LR	-23^{**}	-23^{*}	-19^{**}
$\overline{\Delta G''}$ [Pa]	AP	-1.2	0.18	3.5
	LR	-5.8	-7.3	-4.1
$\overline{\Delta \xi}$ [10^{-3}]	AP	-0.14	0.47	3.0^{*}
	LR	2.3	2.6	3.0
$\overline{\Delta \mu_{stiff}}$ [Pa]	AP	-2.7	-0.47	-0.56
	LR	-23^{**}	-24^{*}	-18^{*}

Table 5.2: "Classic": Summary of the average changes with age for G', G'', ξ, and μ_{stiff}. All values are from linear regressions of the entire cohort. For G', G'', and μ_{stiff}, the LR excitation appears to be more sensitive to changes with age and a paired t-test shows significant differences between age groups ($* = p < 0.10$ and $** = p < 0.05$).

slower than other MRE aging studies. G'' shows nearly no change with age in CC and CR but increases for SLF. G'' is a less reported value and only one study shows a whole-brain decrease with age. Figures 5.3 and 5.4 show the full data for AP-excitations, both "Classic" and "Converged Cascade" for the selected WM regions. Similarly, the full LR-excitation data are shown in Figures 5.5 and 5.6.

The "Converged Cascade" NLI-MRE estimations have both higher contrast in elastograms (Figure 5.3b) and average material property trends are more sensitive to age, as summarized in Table 5.3. Additionally, the average damping ratio (ξ) for LR-excitation with age becomes significant across all three WM regions (CC, CR, and SLF). This is an important finding because the goal of the NLI parameter study (Chapter 2) and defining convergence criteria (Chapter 3) was to potentially improve significance of results or find significance not previously observed. Whether or not this is a "more true" representation of the tissue is an area for future research.

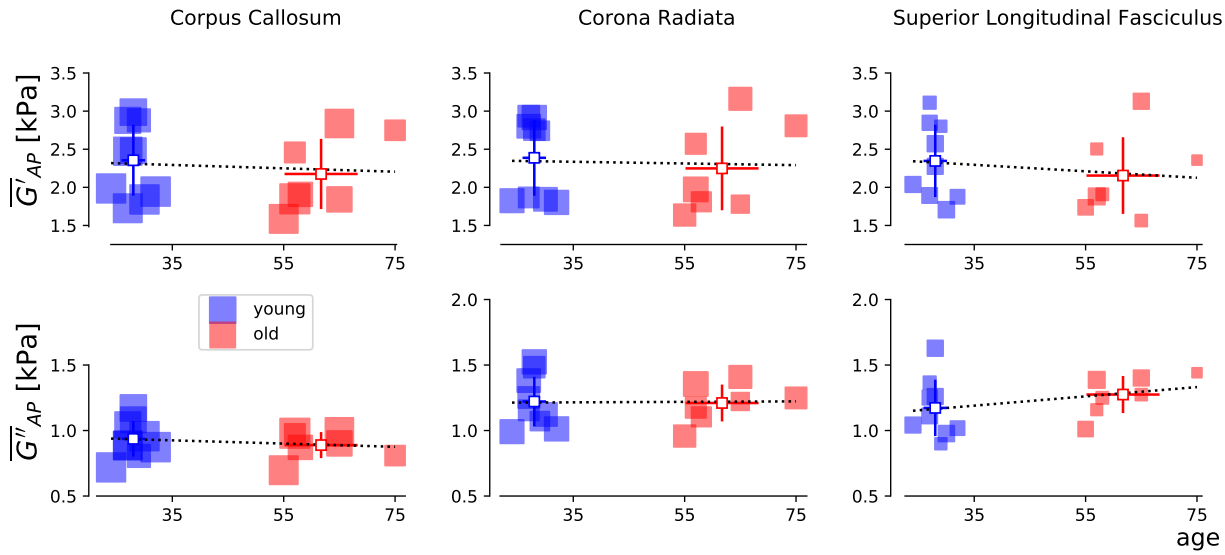

(a) "Classic"

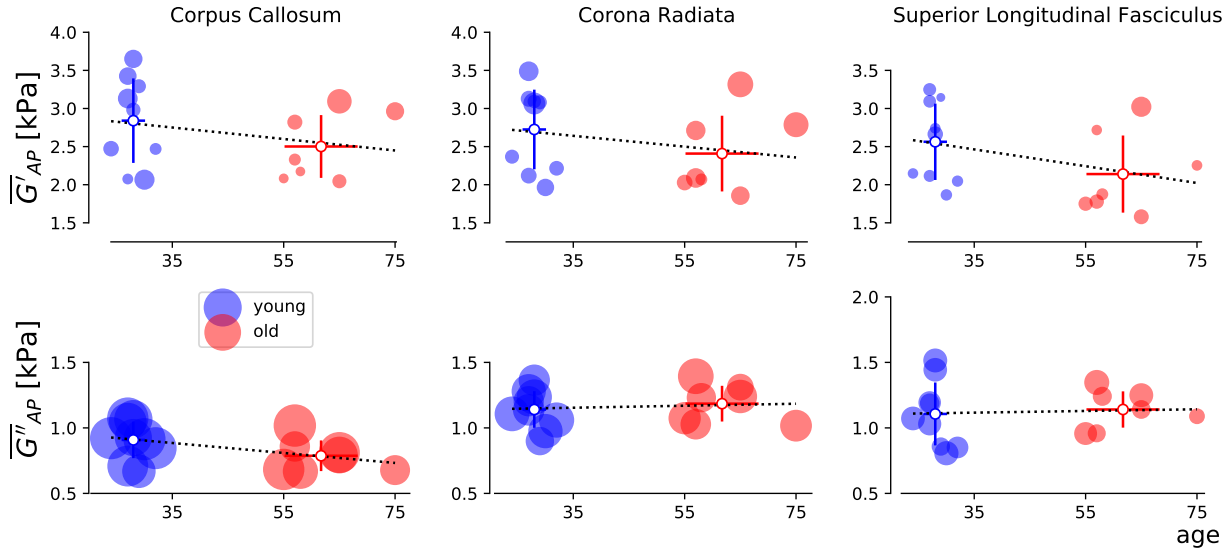

(b) "Converged Cascade"

Figure 5.3: Regional white matter (WM) averages for the standard AP excitation experiments: (a) "Classic" and (b) "Converged Cascade." Neither G' nor G'' are able to significantly separate with age. Size of points indicates relative number of points used in the statistic, where "Classic" are scaled down by 2 relative to "Converged Cascade."

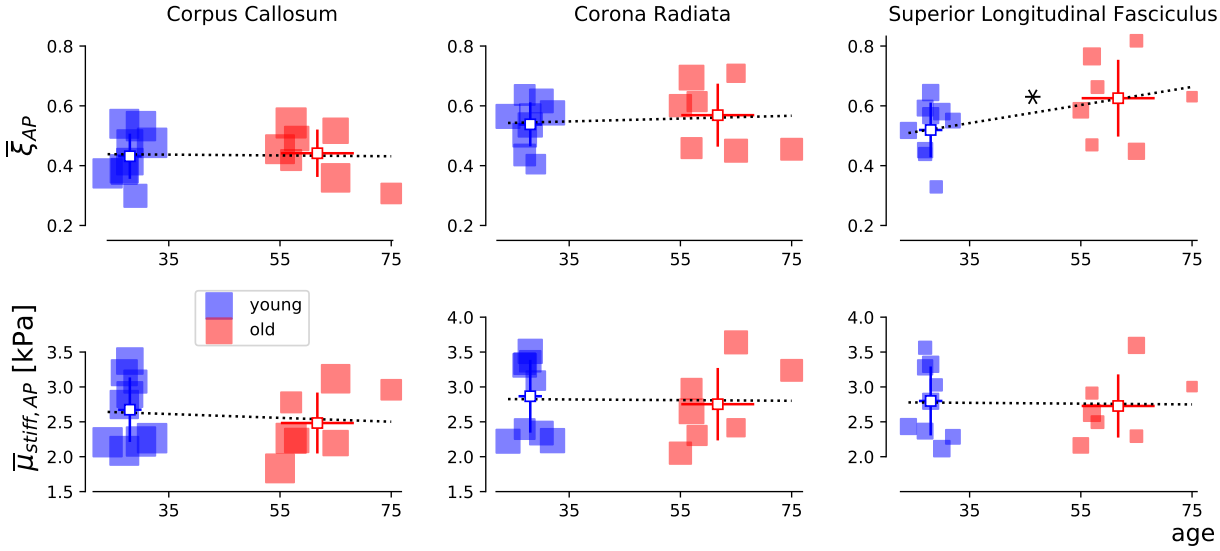

(a) "Classic"

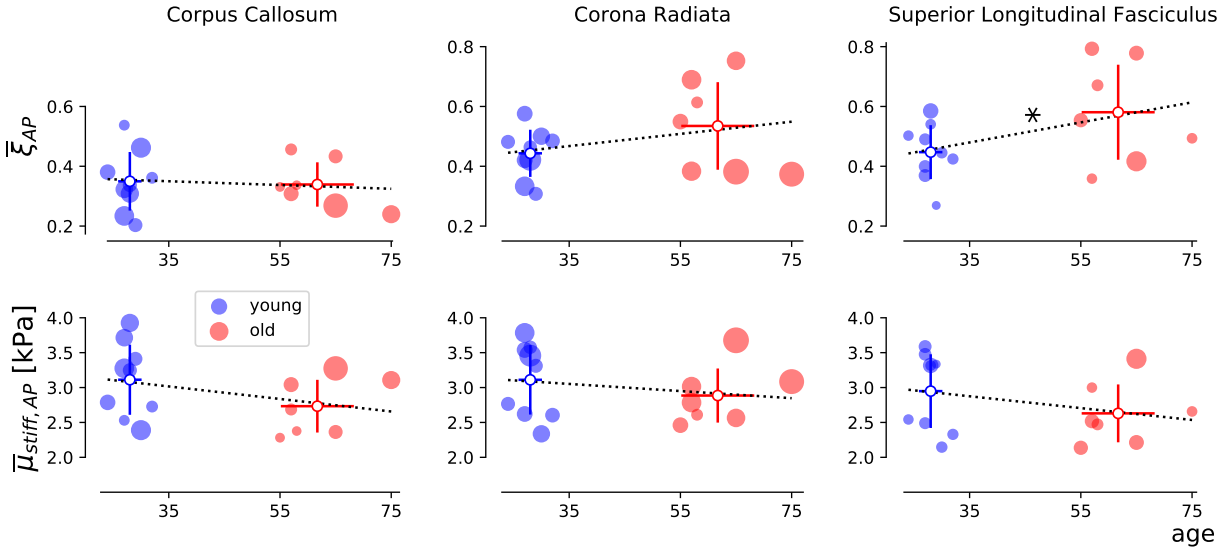

(b) "Converged Cascade"

Figure 5.4: WM regional averages for two derived material parameters, damping ratio ξ (Eq. (1.13)) and shear stiffness μ_{stiff} (Eq. (1.12)), for LR experiments: (a) "Classic" and (b) "Converged Cascade." The damping ratio is the most sensitive (within the selected regions) to age differences in the SLF. "Converged Cascade" has similar effect on sensitivity as individual moduli. Size of points indicates relative number of points used in the statistic, where "Classic" are scaled down by 2 relative to "Converged Cascade." ($* = p < 0.10$)

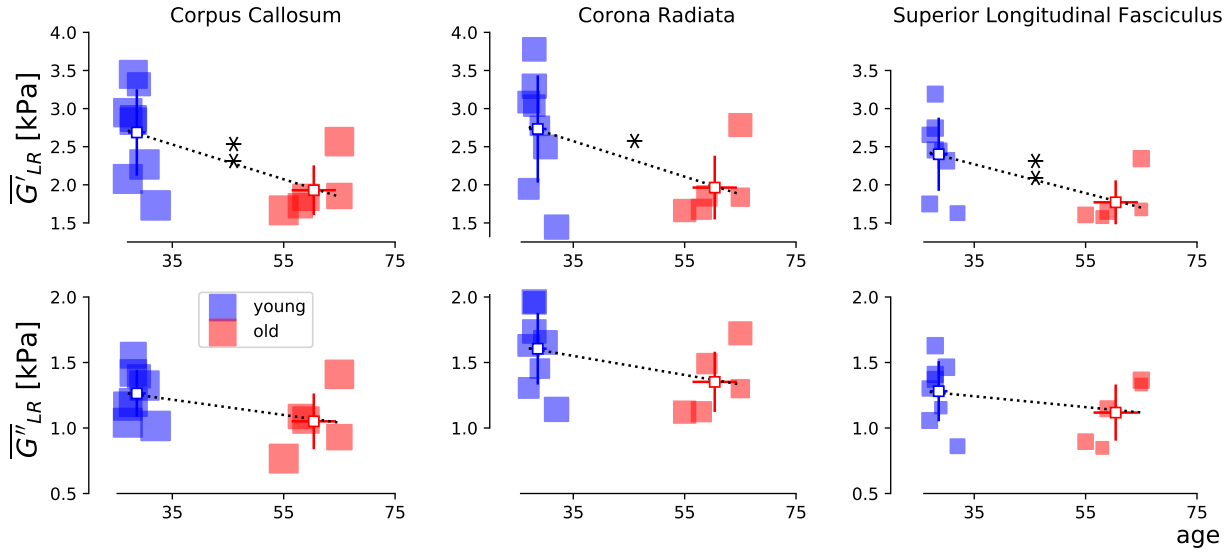

(a) "Classic"

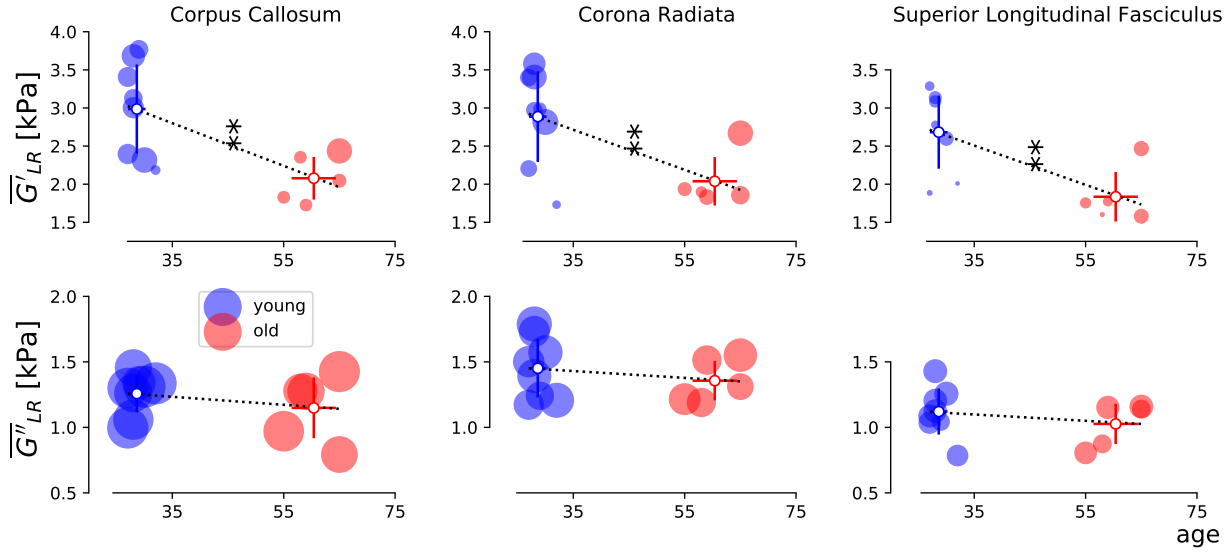

(b) "Converged Cascade"

Figure 5.5: Regional white matter (WM) averages for the LR excitation experiments: (a) "Classic" and (b) "Converged Cascade." The shear modulus (G') is significantly correlated with age in all three WM regions and "Converged Cascade" improved statistical significance in CR. Size of points indicates relative number of points used in the statistic, where "Classic" are scaled down by 2 relative to "Converged Cascade." ($* = p < 0.10$ and $** = p < 0.05$)

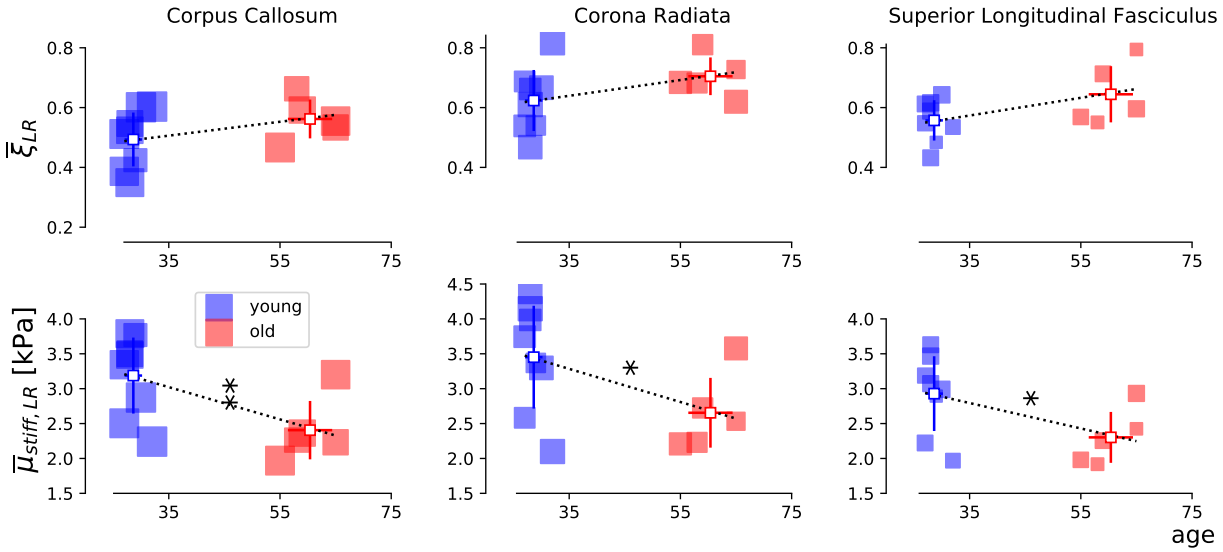

(a) "Classic"

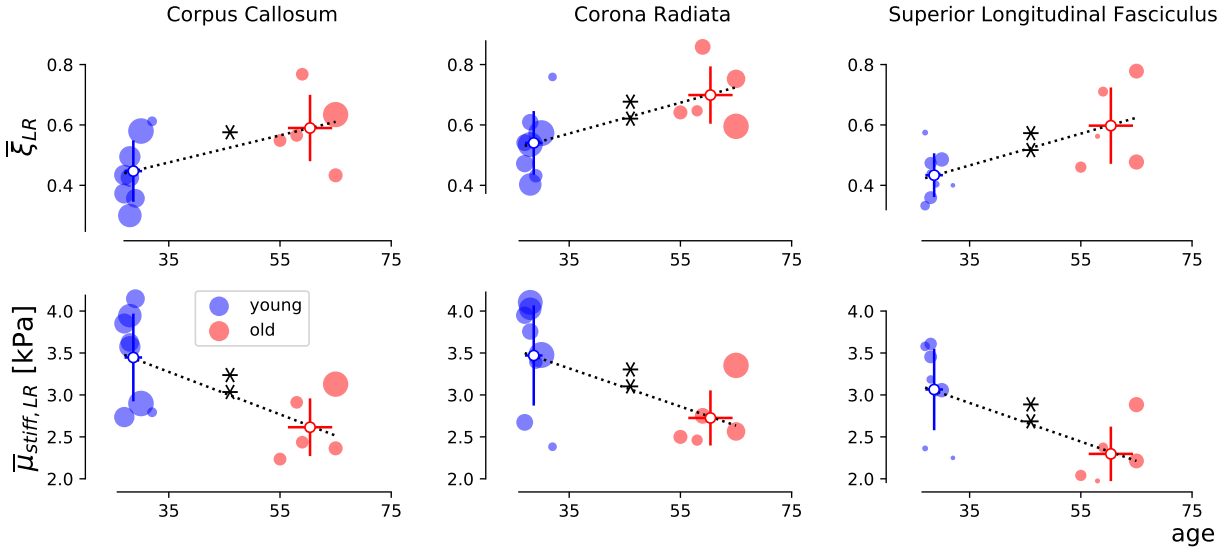

(b) "Converged Cascade"

Figure 5.6: WM regional averages for two derived material parameters, damping ratio ξ (Eq. (1.13)) and shear stiffness μ_{stiff} (Eq. (1.12)), for LR experiments: (a) "Classic" and (b) "Converged Cascade." These measures tend to be more sensitive than G_{LR} individually and their AP-excitation counterparts. "Converged Cascade" either keeps or improves statistical significance. Size of points indicates relative number of points used in the statistic, where "Classic" are scaled down by 2 relative to "Converged Cascade." (* = $p < 0.10$ and ** = $p < 0.05$)

		CC	CR	SLF
$\overline{\Delta G'}$ [Pa]	AP	-7.5	-7.1	-11
	LR	-28^{**}	-26^{**}	-26^{**}
$\overline{\Delta G''}$ [Pa]	AP	-3.8	0.76	0.64
	LR	-3.1	-2.6	-2.4
$\overline{\Delta\xi}$ $[10^{-3}]$	AP	-0.63	2.0	3.4^{*}
	LR	4.5^{*}	5.1^{**}	5.3^{**}
$\overline{\Delta\mu_{stiff}}$ [Pa]	AP	-9.0	-5.1	-8.5
	LR	-25^{**}	-23^{*}	-23^{*}

Table 5.3: "Converged Cascade": Summary of the average changes with age for G', G'', ξ, and μ_{stiff}. All values are from linear regressions of the entire cohort. Three of the four measures show statistically significant differences in all three WM regions for the LR excitation ($^{*} = p < 0.10$ and $^{**} = p < 0.05$)

5.4.2 Measuring Level of Anisotropy with Age

The question proposed in the first multi-excitation experiment (ME-MRE, Chapter 4) and this study is "how does the wave propagation direction influence the isotropic material estimations *in vivo*?" The added benefit from the previous study was ME-MRE's capability to reveal excitation-dependent properties in certain WM regions, which presumably reflect material anisotropy. The difference in material property estimates from the AP and LR estimations was quantified by the voxel-wise analysis of the average strain asymmetry, Eq. (4.6):

$$\varepsilon_{\parallel/\perp} = \frac{\frac{1}{2}(\varepsilon^f_{12} + \varepsilon^f_{13})}{\varepsilon^f_{23}}$$

where the strains are in the DTI-based fiber reference frame ($\{\}^f$) [122]. In Figure 5.7, significantly different DTI-strain ratios, for the two excitations, in CC for the young group and in CR for the old group were observed, based on a two-sided t-test. In other words, Figure 5.7 shows, within the CC, there is a general trend of increased levels of anisotropic strain (DTI-Strain ratio) as well as increased effects of anisotropy on material values (G' and G'' increase with strain ratio) within the younger subjects. For Classical NLI-MRE (Figure 5.7a), there were group-level differences in the properties from AP and LR for G'' in CC

and CR for the young only. For Converged Cascade (Figure 5.7b), the old group gained significance in CC for G' ($p < 0.1$) and G'' ($p < 0.05$) and in CR for G'' ($p < 0.1$). The young group kept the significant differences found in Classic NLI-MRE.

As a way to understand the effect of aging on shear wave propagation, and by extension strain, the ratio of DTI-strain ratios with age are shown in Figure 5.8. Moving from left to right in Figure 5.8, there is a general trend of increasing influence of excitation direction with age. This suggests the average strain state experienced by the tissue becomes more dependent on excitation direction and less affected by waveguiding phenomenon. In the extreme case, waveguiding effects would completely dominate the observed strain field, making it invariant with excitation (i.e. ratio of unity in Figure 5.8). Moving away from a unity ratio shows the average dependence on excitation direction and a decrease in the polarization of the wave vector relative to tissue anisotropy. This has the effect of increasing the variation of any one MRE experiment given an isotropic material model but provides a potentially more material dependent strain state for anisotropic inversions. This could cause a problem with anisotropic inversions where there is only enough strain along one of the anisotropic shear planes and the other is missed. The rigorous study by Tweten et al. [89] showed the necessity for sufficient illumination in all material property directions for accurate and robust estimations. Additionally, where waveguiding is the strongest in CC, there is a significant difference between age groups ($p < 0.05$).

Largest Disparities via *in vivo* Simple Shear

The previous section described the overall average relative shear and material property disparity across the entire tissue. The averages are relevant because average values are reported for ROIs in subjects for comparisons within and across groups; however, the variation in isotropic material property values obtained from largely varying anisotropic strain fields is problematic. Ideally when characterizing a generic anisotropic tissue, one would implement experimental protocols for the direct interrogation of the material along dominant

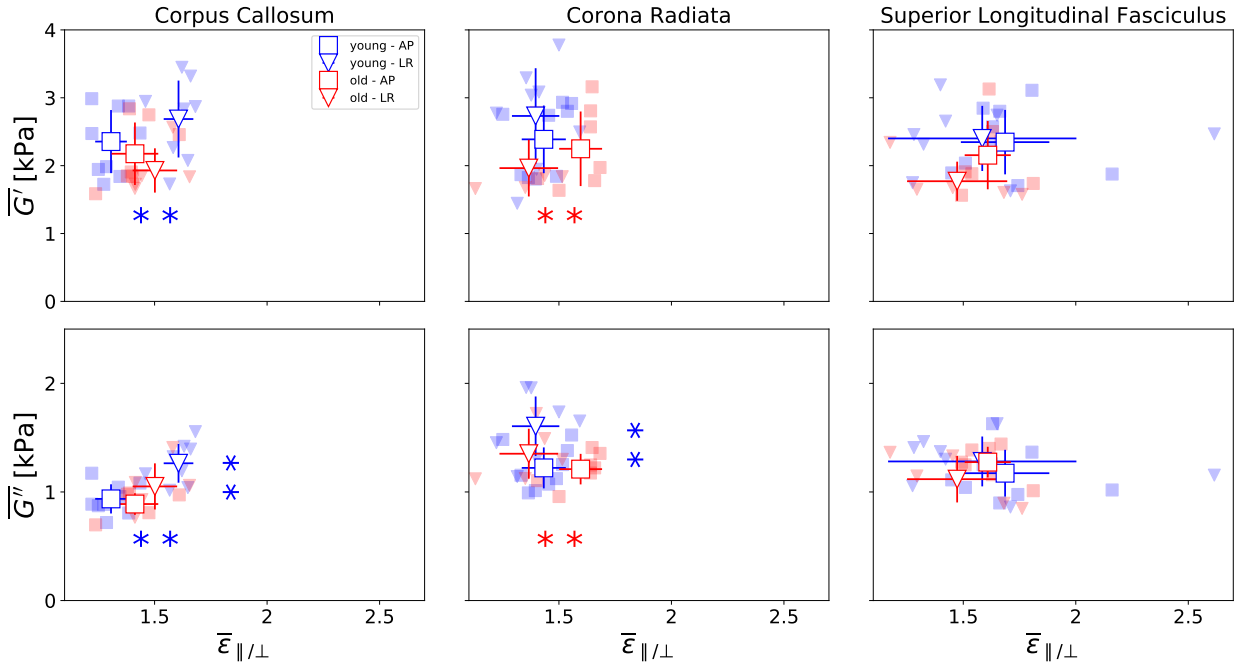

(a) "Classical"

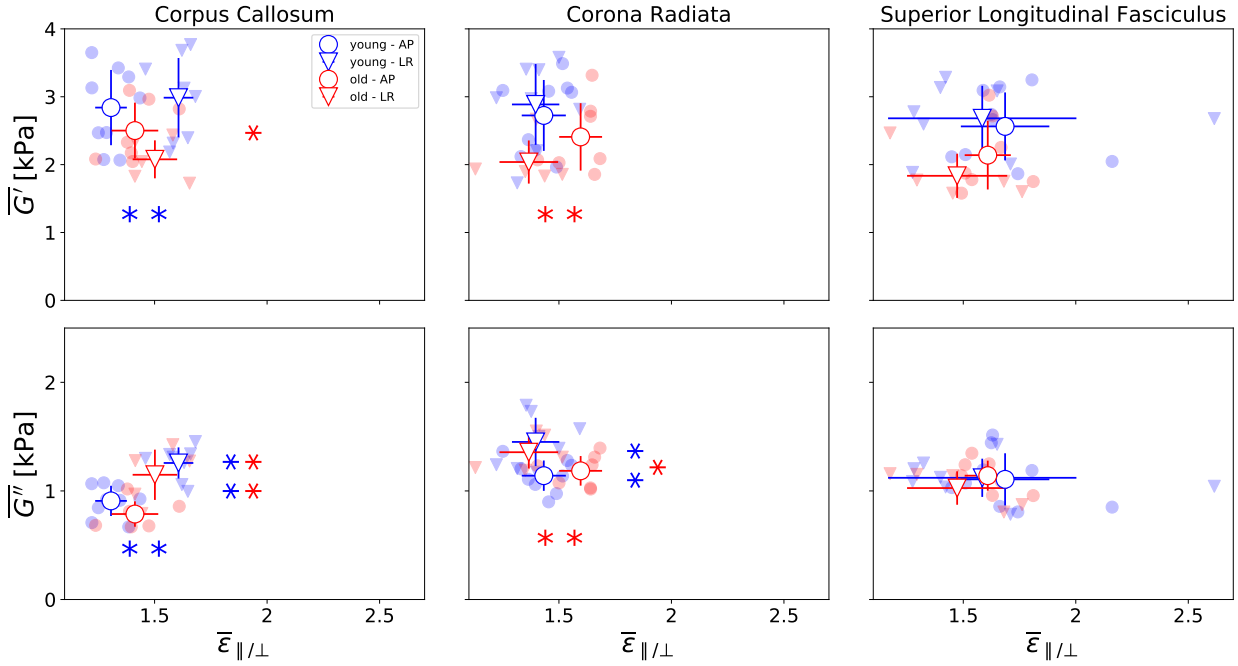

(b) "Converged Cascade"

Figure 5.7: A compilation shear moduli averages from AP and LR excitation experiments relative to the voxel-wise strain asymmetry, a repeat of Figure 4.4 from original multi-excitation study. Distinct strain ratios are observed in the young group for CC and for the old group in CR, similar to the single subject. For the "Classical" estimation, the loss modulus (G'') in the CC and CR were significantly different in the young group. The older group did achieve statistical significance in CC (G' and G'') and G'' for CR for the "Converged Cascade" estimations. ($* = p < 0.10$ and $** = p < 0.05$)

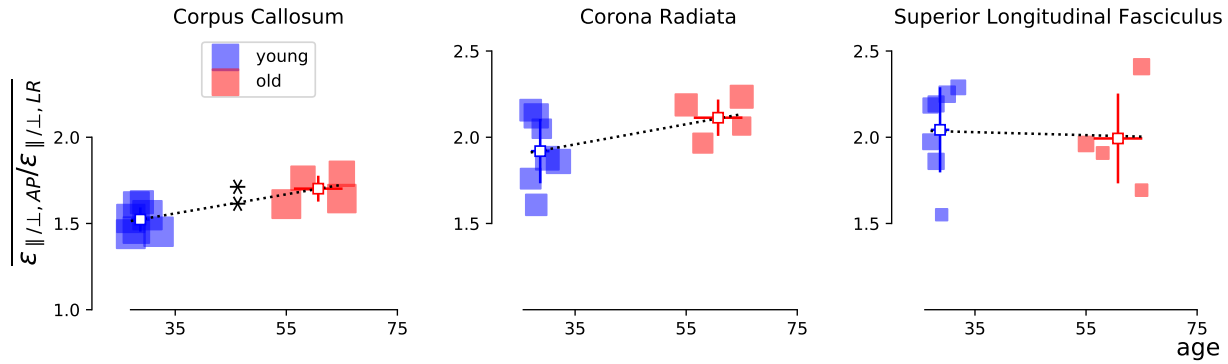

Figure 5.8: Voxel-wise ratio of $\varepsilon_{\parallel/\perp}$ ratio for the two excitations, AP and LR, with age. $\varepsilon_{\parallel/\perp}$ is a measure of strain anisotropy within a voxel containing well-aligned axons, and comparing between distinct excitations attempts to measure whether the strain state is invariant to strain source (unity). Interestingly, the ratio of ratios about 1.5 or greater, never less than unity. The trends for young to old in CC and CR are away from unity. Size of points indicates relative number of points used in the statistic. (** $= p < 0.05$)

anisotropic axes. For MRE, it is difficult to obtain this level of control in a phantom or even within *ex vivo* tissue [18, 20, 118] and impossible *in vivo*. The next best case scenario for *in vivo* is having as distinctly different excitation as possible (i.e. multi-excitation) and selectively identifying areas where the shear state is predominantly along the transverse or perpendicular axes. A simple threshold of relative shear in the DTI-frame, Eq. (5.1), allows for a selection of such voxels for such comparisons.

The isotropic estimates of a well known anisotropic material correlates well with the corresponding simple shear strain states. The range of differences in parallel versus perpendicular shear moduli are up to about 1.3× for G' and nearly 1.5× for G'', see Figure 5.9. These relative ratios are consistent with previous studies [18, 101, 118, 124, 125]. The relationship is most distinct and coherent for the most structurally well-ordered tissue of the CC and CR, compared with the SLF. SLF is both expected to be uniform throughout the ROI in terms of structure, based on DTI measures, and overall size. The simple shear ratios for both damping ratio (ξ) and shear stiffness (μ_{stiff}) tend to be near unity for most WM regions and with age, see Figure 5.10. Even for cases with statistical significance, one of the age groups has a group mean near unity. The number of points used in each calculation is displayed in

the percent of the WM region of the plots and the ratio of parallel ($N_{\parallel}$) to perpendicular ($N_{\perp}$) are summarized in Figure 5.11. Although the relatively small sample size experiences either of the simple shear cases, the trends are relatively consistent with more well-controlled studies. As noted in the last section from the study by Tweten et al. [89], simple shear cases will be problematic for estimating multiple material properties where there is insufficient strain information. There seems to be no difference for simple shear statistics between age groups, including material properties and number of voxels experiencing simple shear. The commonality shared across both WM regions and age is always relatively more parallel than perpendicular simple shear. This is another important observation when looking forward to incorporating an anisotropic model into the NLI estimation framework.

Analytical Transversely Isotropic Model Tissue

The previous section identified cases where the shear was nearly along one shear plane in order to find potential property bounds within the anisotropic tissue. The ratio of the parallel to perpendicular moduli was about $1.3 - 1.5$, consistent with the literature. It is unlikely these are the true ratio of properties given the sampling within the region, lack of control on strain, and model-data mismatch within NLI. The open question is around how NLI estimates a purely transversely isotropic material given an exact displacement solution. Five cases of applying shear to the transversely isotropic material along five angles (θ) relative to the two different moduli, described in Section 5.3.3, and using the heterogeneous, isotropic NLI to estimate the material properties are summarized in Figure 5.12. The shear moduli estimated by NLI (Figure 5.12a) underestimate the cases where the input displacement field is for strictly one of the moduli. The likely cause for this discrepancy is NLI assumes nearly incompressible and analytical solution is perfectly incompressible. For the middle three angles, NLI estimates an average property value that one would expect from an isotropic material model, an average of the two moduli. The damping ratio (ξ) is an interesting parameter to consider because the way the two moduli were chosen ensured a constant

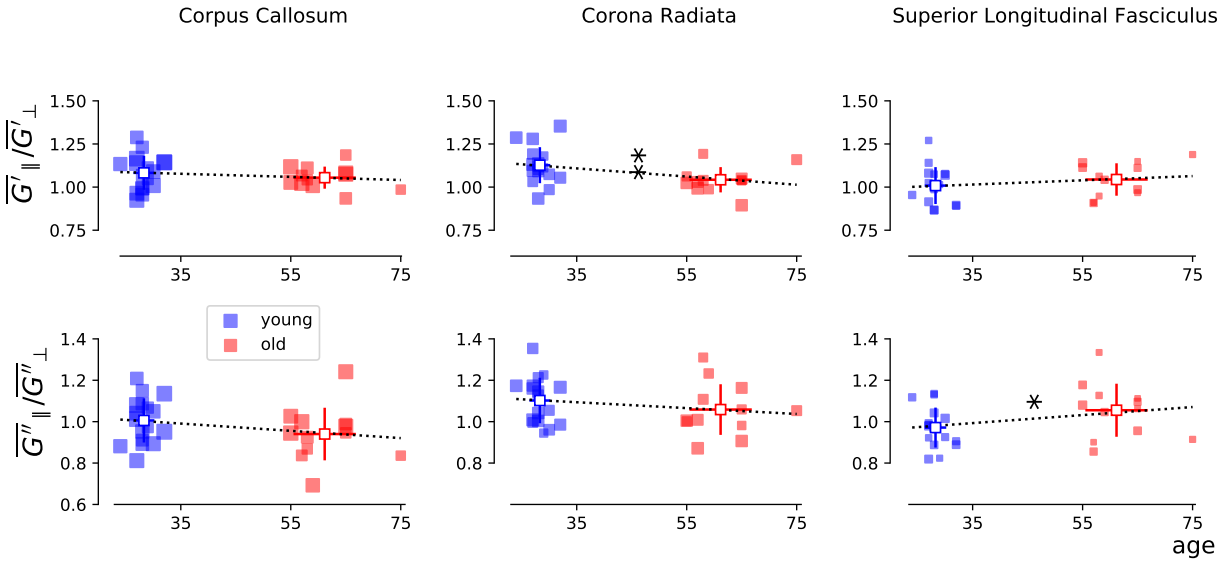

(a) "Classic"

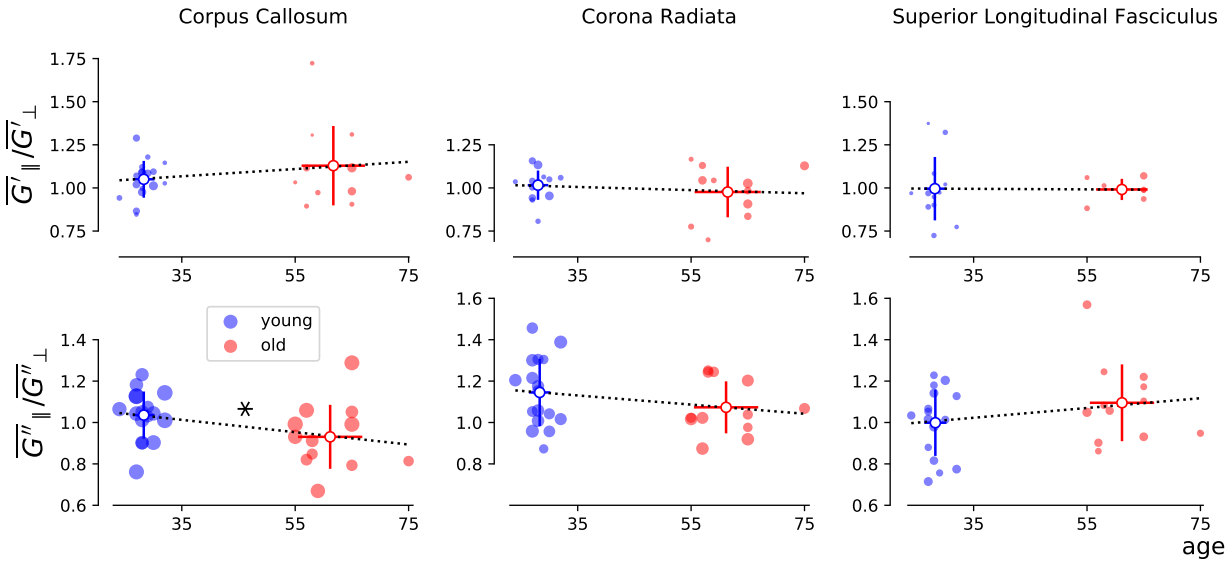

(b) "Converged Cascade"

Figure 5.9: Shear moduli and computed material property ratios for simple shear with age. (a) Significant differences with age for $G'_{\parallel}/G'_{\perp}$ in CR ($p < 0.05$) and G''_{SLF} ($p < 0.10$); (b) significantly different only in $G''_{\parallel}/G''_{\perp}$ CC. Size of points indicates relative number of points used in the statistic.

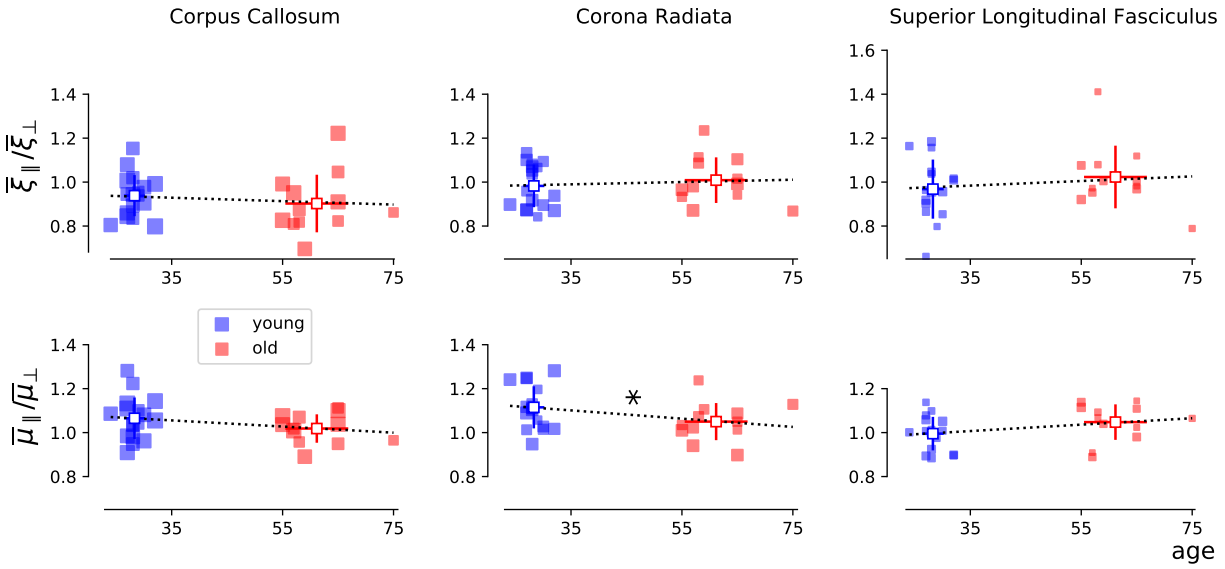

(a) "Classic"

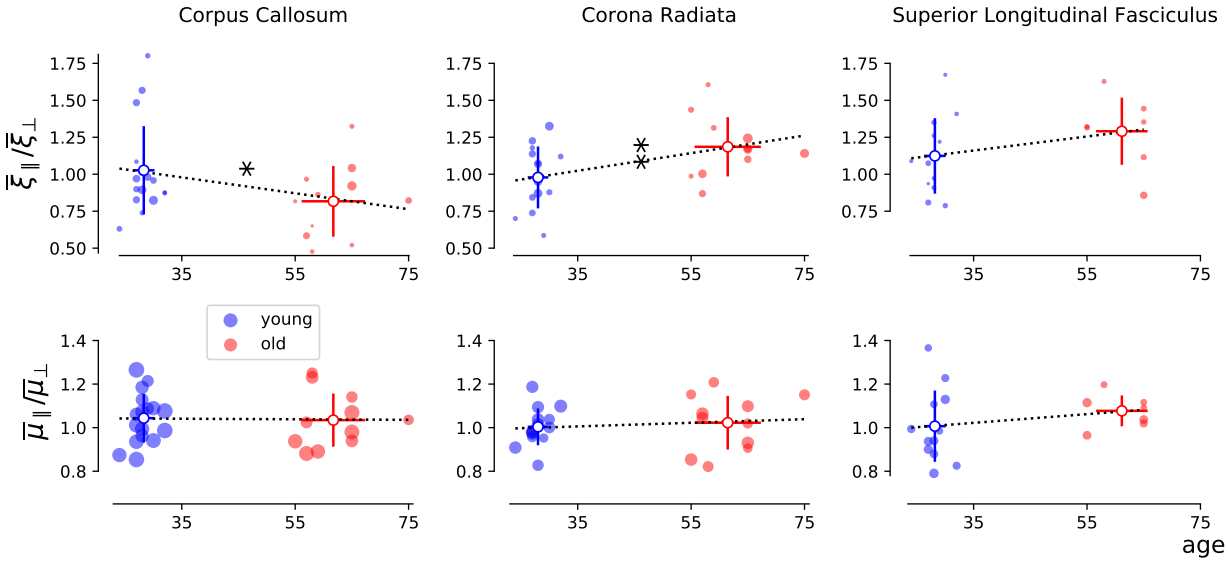

(b) "Converged Cascade"

Figure 5.10: Simple shear ratios for two derived material parameters, damping ratio ξ (Eq. (1.13)) and shear stiffness μ_{stiff} (Eq. (1.12)), for LR and AP experiments: (a) "Classic" and (b) "Converged Cascade." (a) Significant differences with age for $\mu_{\parallel}/\mu\perp_{CR}$ ($p < 0.1$); (b) significantly different in $\mu_{\parallel}/\mu\perp$ for CC ($p < 0.1$) and CR ($p < 0.05$). Size of points indicates relative number of points used in the statistic.

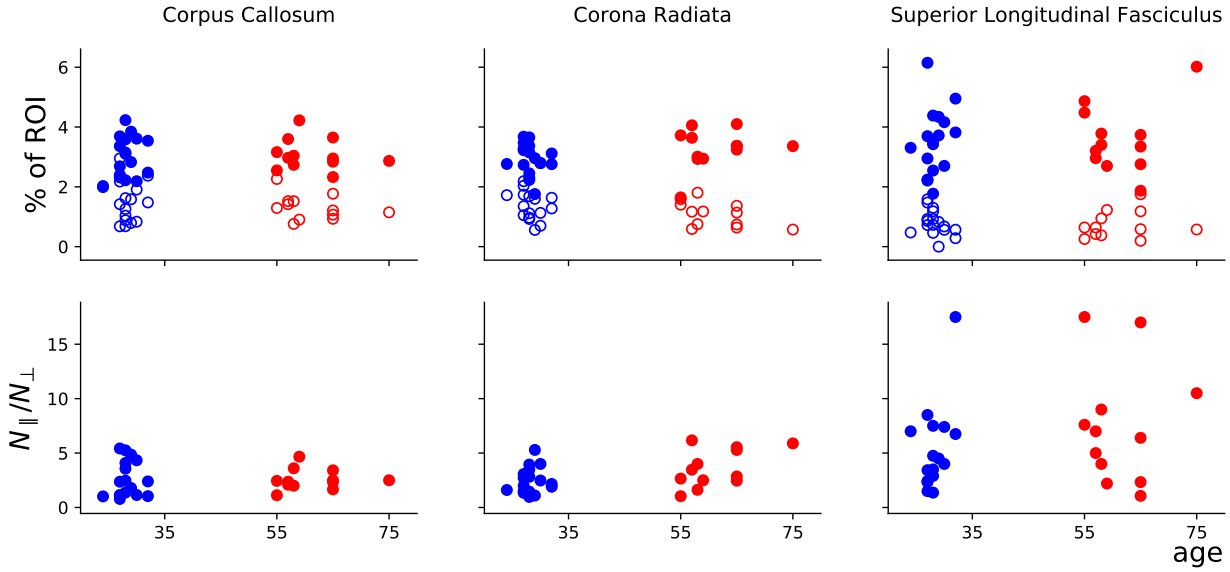

(a) "Classic"

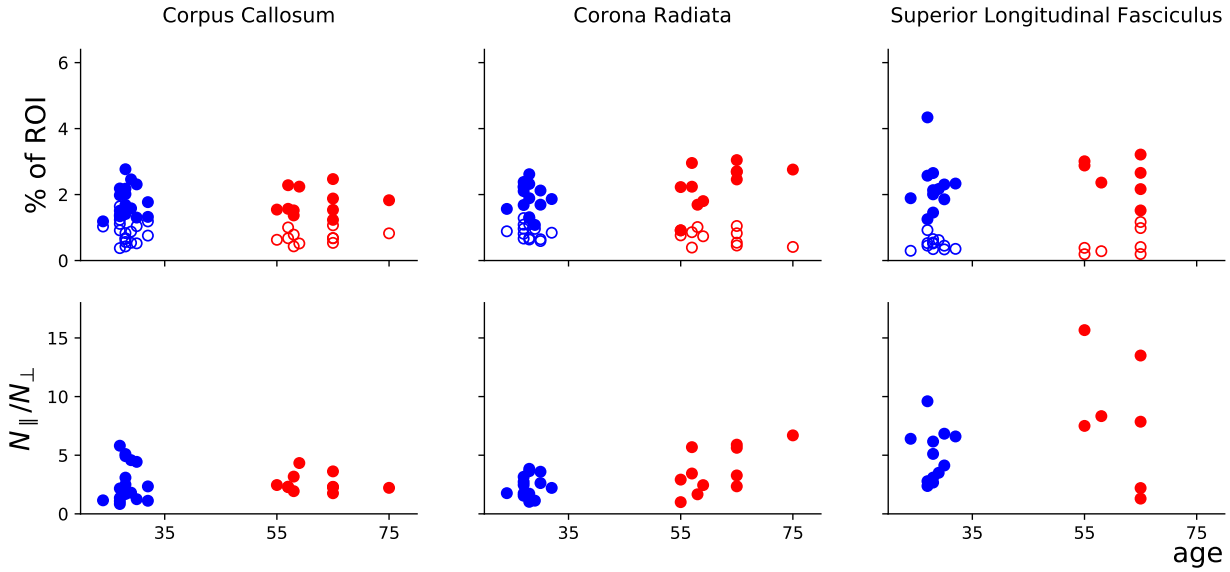

(b) "Converged Cascade"

Figure 5.11: The percentage of voxels within a WM region for voxel-level parallel and perpendicular simple shear with age and the ratio of parallel to perpendicular. Parallel simple shear always out numbers perpendicular shear for all subjects in these three WM regions.

damping ratio throughout the material. NLI does not directly estimate damping ratio but the resultant moduli ratio always gives a value within 5% of the exact value. This could be partial evidence of the reason why damping ratio has proven to be the most sensitive measure across nearly all of the recent NLI-MRE studies applied to a range of populations [13–16,40,41,75].

5.5 Conclusions

The previous single subject multi-excitation experiment was successfully implemented in a larger cohort and at least part of the results were replicated in the young group (i.e. G'' differences in CC and CR). Utilizing the DTI structural information outside of the heterogeneous, isotropic inversion allowed for capturing significant anisotropy in the young group and a decrease in anisotropy in the older group. The young group does have an unusual split in the average storage moduli (G') for all three WM regions of interest. The DTI metrics do not seem to show a similar split in the young subjects but rather a larger overall variance in group-level statistics. Additionally, implementing the understanding of NLI parameters in Chapter 2 and incorporating a new convergence criteria from Chapter 3 generally kept or improved statistical significance of results. Ultimately, this study furthers three important areas underlying all of brain MRE: implementing improved parameters and quality metrics into NLI, characterizing the underlying changes with age, and further characterization of anisotropic tissue properties within WM regions.

Future work will look to expand the number of subjects acquired, capture physiological and behavioral measures, and implement an anisotropic material model. A larger cohort will not only help improve the statistical power but capture a wider sample of the normal variation across the age span and within age groups. The goal is to improve our understanding of human brain material properties such that MRE is capable of quantifying the actual "brain age" instead of relying solely on chronological age [126]. Defining a "material property age" will be aided by adding measures of both physiological and behavior measures which are well

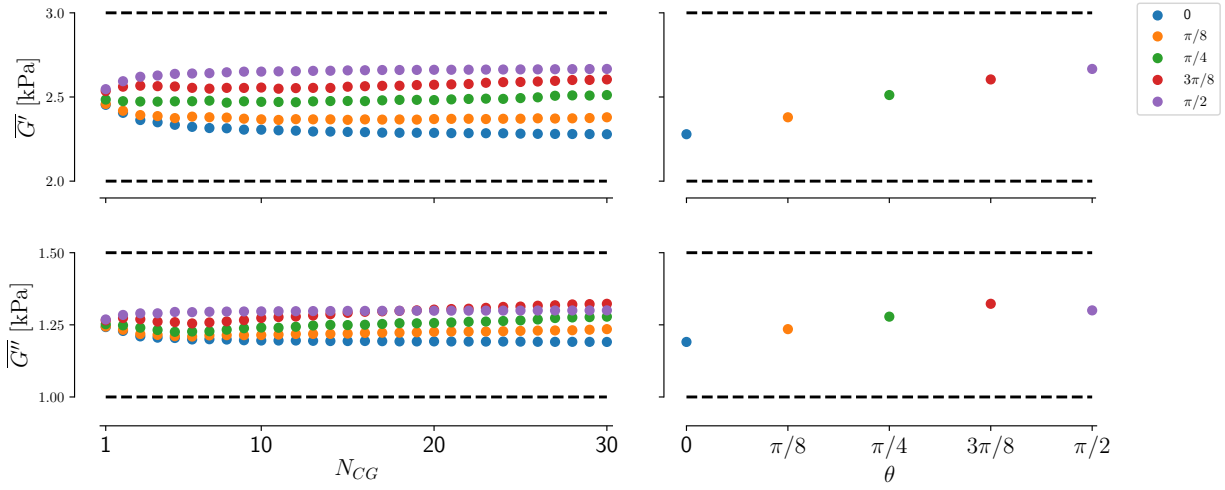

(a)

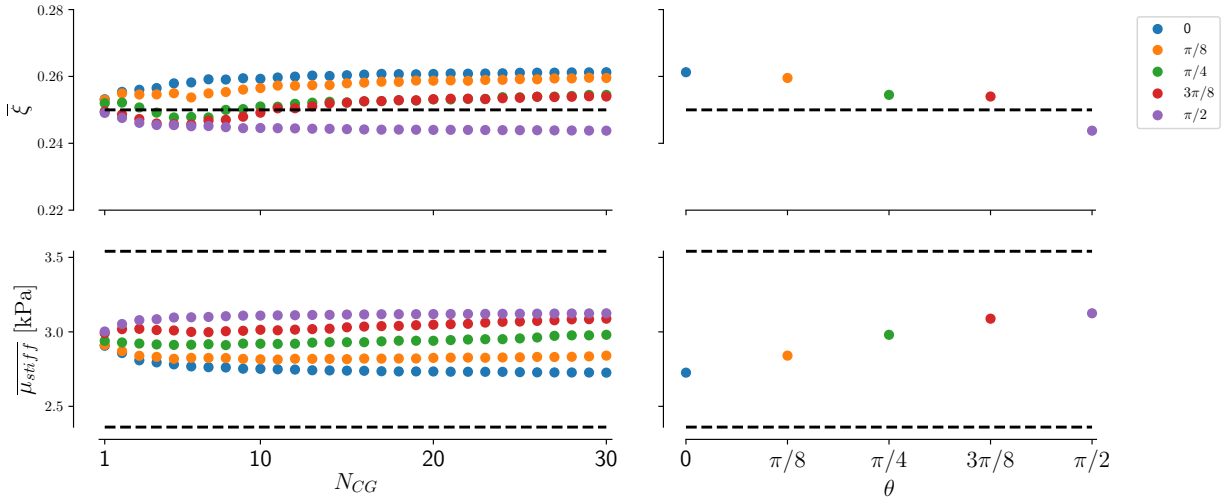

(b)

Figure 5.12: Transversely isotropic analytical solution as the "measured" displacement field for a single subzone inversion. The actuation is applied to the "softer" shear moduli ($G = 2 + i1$ [kPa]) for $\theta = 0$ and rotated until only applied to "stiffer" moduli ($G = 3 + i1.5$ [kPa]) for $\theta = 90$, **fixed** ($\vec{u} = \vec{0}$) opposite the applied shear. (a) G' and G'' are estimated for entire domain (averages reported); (b) summarizes the average computed material properties. NLI under estimates both $\overline{G'}$ and $\overline{G''}$ but is within about 5% for $\overline{\xi}$.

established in the medical and psychology fields. This is not to suggest the goal is to replace cost-effective blood tests with expensive MRIs but rather provide a more comprehensive understanding of the brain to aid in differential diagnosis given a patient specific "normal" properties when diagnosing neurological diseases. As noted in the introduction, anecdotal evidence of subject reported education level and occupation for older adults was varied from no formal education to through advanced degrees (all passed the IRB approved minimum cognitive ability). There is established evidence of structurally different organization in "high-performing" older adults and a way to discern this difference from a material property perspective would aid understanding of structure-function relationships [121]. The evidence suggests "high-performing" adults have more bilateral characteristics than young, as well as "low-performing" adults, resulting in stronger connections between hemispheres through the corpus callosum and are potentially mechanically stiffer. Although there were no cognitive or physiological measures captured in this study, acquiring more quantitative information about subjects will improve specific and general differences of subject and group statistics. Finally, there were discernible differences across the cohort of subjects, regardless of age, for the most disparate material properties for the "simple shear" voxels. The strong correlation with the DTI-frame strain state suggest two things with regards to the need for an anisotropic model: the voxel-level properties are significantly different and capturing more material information will increase understanding while decreasing estimation variance.

Chapter 6

Summary of Contributions and Future Directions of MRE

6.1 Advancing the Field of MR Elastography

The most recent review of MR Elastography applied to the human brain states the two most important areas for development: improving the resolution of techniques (imaging and material estimation) and further investigation "into the biological basis of stiffness and the mechanisms underlying stiffness changes" [127]. The work in this dissertation made important progress into both areas through characterization of material estimation parameters (NLI Parameter Study), defining quality metrics for material estimations (convergence criteria), improvements in experimental design (multi-excitation), and observed the diffuse and specific mechanics of aging on the human brain. Specifically, and in regards to Aim 1, the NLI parameter study tested a number of assumptions central to the NLI estimation framework and provided mechanics-based explanations and solutions. Previously, the octahedral shear strain signal-to-noise ratio (OSS-SNR) was an important contribution for defining a quality measure for the input (MR displacement) into NLI, and this work proposed two convergence criteria for providing a quality metric for the output (material property statistics). In regards to Aim 2, the multi-excitation experiment (ME-MRE) provided a new way to "test" *in vivo* tissue of the human brain which is inherently difficult to access and control. ME-MRE was performed on a larger cohort of young and old adults to assess the effects of aging on the human brain, specifically WM regions. The developments in NLI parameter selection and convergence criteria were compared with the "Classic" version of NLI-MRE. In many cases, the new approach to NLI-MRE improved the statistical significance of results

and, in a few cases, provided significance where there previously was none.

Mechanicians are always looking for innovative ways to characterize materials and understand the limits of their analysis (i.e. isotropic NLI of anisotropic tissue). The combined application of these three areas culminated in advancing our understanding of the complex, yet delicate, tissue governing human life, the brain. Tools developed and applied to the aging brain study afforded researchers new ways to interrogate the domain and improved statistical power of the results. As with all important areas of scientific research, but specifically related to MRE, there are many more questions to ask, and answer, about both areas investigated here and phenomenon at multiple scales: length scales above and below a voxel and timescales from real-time function to longitudinal studies.

6.2 Current and Future Opportunities for MRE

6.2.1 Further Development of Nonlinear Inversion

A major theme underlying the work in this dissertation is the errors from model-data mismatch. Two of the top opportunities, not just NLI, for better understanding of specific and diffuse processes would benefit most from more accurate material models, specifically: anisotropic models [22, 74, 96, 119, 128] and multi-frequency [35, 129].

Anisotropic Model The next major and most important step in the development of NLI-MRE is the implementation of an anisotropic model. The work here has shown both it's necessity for reducing variance in property measures and capturing missed biomarkers from more accurately characterizing the inherent anisotropic material properties of white matter. Given the flexibility of the NLI framework, an orthotropic material model will be

implemented with the form:

$$\begin{bmatrix} \sigma_{11} \\ \sigma_{22} \\ \sigma_{33} \\ \sigma_{23} \\ \sigma_{31} \\ \sigma_{12} \end{bmatrix} = \begin{bmatrix} C_{11} & C_{12} & C_{13} & 0 & 0 & 0 \\ C_{12} & C_{22} & C_{23} & 0 & 0 & 0 \\ C_{13} & C_{23} & C_{33} & 0 & 0 & 0 \\ 0 & 0 & 0 & C_{44} & 0 & 0 \\ 0 & 0 & 0 & 0 & C_{55} & 0 \\ 0 & 0 & 0 & 0 & 0 & C_{66} \end{bmatrix} \begin{bmatrix} \varepsilon_{11} \\ \varepsilon_{22} \\ \varepsilon_{33} \\ 2\varepsilon_{23} \\ 2\varepsilon_{31} \\ 2\varepsilon_{12} \end{bmatrix} \tag{6.1}$$

and DTI vectors will reduce the complexity of the estimation by transforming it into a locally transversely isotropic material model:

$$\underline{\underline{C}} = \begin{bmatrix} C_{11} & C_{12} & C_{13} & 0 & 0 & 0 \\ C_{12} & C_{22} & C_{13} & 0 & 0 & 0 \\ C_{13} & C_{13} & C_{33} & 0 & 0 & 0 \\ 0 & 0 & 0 & C_{44} & 0 & 0 \\ 0 & 0 & 0 & 0 & C_{44} & 0 \\ 0 & 0 & 0 & 0 & 0 & (C_{11} - C_{22})/2 \end{bmatrix} \tag{6.2}$$

This transformation reduces the number of planes/axes of symmetry from three in the orthotropic model to just one for the transversely isotropic model. This is important from an estimation perspective because it reduces the unknown material constants from nine (9) to five (5). The validity of this model will be tested against simulated fields (e.g. analytical solutions, Appendix A) [17,89], *ex vivo* [20,119,130], animal models [131], and *in vivo* [22,74]. An interesting area for cross-validation may come from not using DTI to influence the material model (i.e. general orthotropy) and see if it can estimate properties with similar dominate orientations to DTI (i.e. transverse isotropy). The DTI community would benefit from the quasi-validation of tissue properties mimicking structure, and NLI could show it's framework

can estimate a large range of scales. Ultimately, an anisotropic material model will increase specificity and decrease biases from model-data mismatch.

Multi-Frequency Biological tissues behave mostly like viscoelastic materials which are inherently frequency dependent; however, the majority of NLI-MRE studies are performed and analyzed at a single frequency (50 [Hz]). There has been some initial development of multi-frequency NLI [35], but larger studies need to properly characterize the way one would for benchtop rheometry. The open question for multi-frequency MRE is identifying the most accurate model for frequency-dependent behavior. A common model for linear viscoelastic tissues is the power-law model, relating constant damped parameters to frequency, defined as

$$\mu_R(\omega) = \Theta_{R0}\omega^{\alpha_R} \quad \text{and} \quad \mu_I(\omega) = \Theta_{I0}\omega^{\alpha_I} \tag{6.3}$$

where Θ_{R0} and Θ_{I0} are the elastic and viscous damped parameters, respectively, and α_R and α_I are the storage and loss moduli exponents [12,35]. The practical limitations of imaging a single subject would not lend itself well to clinical practice, but it would instead be important for both "improving resolution" of MRE and enabling more complete studies of stiffness as a biomarker for tissues. Once a tissue is well characterized, the results and understanding can influence the experiments at a single frequency by ensuring any frequency dependence would be less than other experimental and systematic errors.

6.2.2 Clinical Translational MRE

MRE has become an important imaging tool for hepatologists assessing the severity of common liver diseases due to it's quantitative, robust, repeatable, and non-invasive characteristics [132]. At this time, MRE has not found a clinical role outside of the liver, but it has the potential for applications in a number of areas including: hydrocephalus [8, 64], cancerous brain tumors [**?**, 9, 133, 134], multiple sclerosis (MS) [135], Alzheimer's disease, traumatic

brain injury (TBI) [136, 137], and pituitary macroadenomas [138].

Animal Models for Disease Animal models are an ideal way to observe and even induce diseases similar to those experienced in the human body. For example, Jugé et al. induced hydrocephalus in a small group of rats and, with the aid of a high-field MRI scanner, were able to observe changes in microstructure and stiffness using MRE [139]. High-field MRI scanners enable higher resolution which affords MRE researchers closer access to the cellular mechanisms elucidating stiffness changes [140, 141]. Another important case is introducing glioblastomas into mouse brains because it is the most common primary brain tumor and provides an ideal case for developing anisotropic material estimation models [131]. This is useful for anisotropic models because the growth of cancerous tissue can be anisotropic and the displacement of healthy brain tissue, both GM and WM, alters isotropic and anisotropic properties differently. Finally, animals can be surrogates for the growth and integration of engineered tissues where MRE can non-invasively measure properties of *in vitro* growth and *in vivo* regeneration identically [141]. This is important specifically for tissue-engineering and regenerative medicine (TERM), because regenerative organs have struggled to move from basic science into clinical translational research and, ultimately, clinical practice [142]. For all animal models of interest, there is the additional benefit of *ex vivo* mechanical testing and histology not available in human subjects [118, 143].

Clinical Populations Techniques in improving the specificity and sensitivity in animal models will greatly aid and accelerate the application of MRE in clinical translational studies. The application of OSS-SNR to the MRE displacement alone has allowed neurosurgeons to assess the adherence of cancerous tumors for pre-operative planning [88,144]. MRE material estimations can then characterize the softness or, conversely, stiffness of the tumor itself for further pre-operative planning [**?**, 9, 133, 134]. Beyond large-scale tissue diseases, MRE also has the sensitivity at much smaller length scales and stiffness variations. NLI-MRE

specifically has already proven its sensitivity in subcortical grey matter structures across normal populations, diseases, and interventions [13–16, 38–41]. This sensitivity will prove invaluable for assessing both focal and diffuse stiffness biomarkers for a range of diseases with the ultimate goal of identifying the earliest possible stages of disease.

6.3 Conclusions

MRE is proven as a clinically relevant imaging modality in detecting direct tissue changes in the liver secondary to disease pathology. The work in this dissertation has contributed to increasing the sensitivity of brain MRE when it is applied to probe pervasive changes in brain mechanical properties, such as those occurring with healthy aging. With these advances and additional studies connecting biology to stiffness, MRE is poised to make the connection from microscopic changes to organ-level dysfunction leading to better clinical outcomes. Specific to white matter tissue, healthy and diseased, continued research into anisotropic material models will improve the ability to distinguish neurons from their supporting cellular components. These developments will transform MRE from a technique used in the homogeneous tissue of the liver into an advanced imaging modality capable of distinguishing salient features in the complex hierarchy of the human brain.

Appendix A

Simple Shear

A.1 Analytical Wave Solutions

An analytical comparison is ideal because the solution is a subset of the governing equation used for experimental estimates, thus removing any three-dimensionality of finite domains. Okamoto et al. [145] used a solution generated by Berry [146] for analytical comparisons with shear rheometry experiments. The one-dimensional (1D) solution (only dependent in one direction) is assumed to be separable and harmonic:

$$\tilde{\mathbf{u}}(x, y, z, t) = \mathbf{u}^*(x, y, z)\mathrm{e}^{i\omega t} = \mathbf{u}\mathrm{e}^{i\omega t} \tag{A.1}$$

where the amplitude $\mathbf{u}^*$ is complex (magnitude and phase). The full three-dimensional (3D) governing equation is Navier's equation, Eq. (1.2):

$$\nabla \cdot (\mu(\nabla \mathbf{u} + \nabla \mathbf{u}^T)) + \nabla(\lambda \nabla \cdot \mathbf{u}) = -\rho\omega^2 \mathbf{u}.$$

where $\mathbf{u}$ is the 3D displacement field, λ and μ are Lamé's properties, and ρ is the density (assumed constant). To obtain the simplest solution in 1D, the domain is assumed to be isotropic and divergence free thus reducing Eq. (1.2) to the Helmholtz equation:

$$\frac{d^2\mathbf{u}_x}{dz^2} = -k^2\mathbf{u}_x, \quad k^2 = \frac{\rho\omega^2}{\mu}. \tag{A.2}$$

General solutions to Eq. (A.1) are defined in the family of solutions given by

$$\mathbf{u}_x(z) = A_1 \cos(kz) + A_2 \sin(kz) \tag{A.3}$$

where A_1 and A_2 are solved for based on particular boundary conditions (BCs). The BCs of interest for this analysis are the cases where shear is applied on one end

$$\begin{cases} \mathbf{u}_x(0) & = u_0 \\ A_1 & = u_0 \end{cases} \tag{A.4}$$

and the following three experimental scenarios for the face opposite the excitation:

$$\text{free} : \begin{cases} \frac{d\mathbf{u}_x}{dz}(h) & = 0 \\ A_2 & = u_0 \tan(kh) \end{cases} \tag{A.5}$$

$$\text{fixed} : \begin{cases} u_x(h) & = 0 \\ A_2 & = -u_0 \cot(kh) \end{cases} \tag{A.6}$$

$$\text{dynamic} : \begin{cases} u_x(h) & = u_h \\ A_2 & = \frac{u_h - u_0 \cos(kh)}{\sin(kh)} \end{cases} \tag{A.7}$$

where u_0 and u_h are defined at the boundary faces and h is the length of domain in the z-direction. The analytical solution is used both for variations of the solution itself and for defining BCs in the finite element forward calculation (FWD) used in the nonlinear inversion (NLI), defined in section 2.1.3 and compared with the analytical solution. The simple shear numerical studies will help understand the effect of the domain decomposition ("subzoning") that is central to the NLI formulation, see section 2.2.3.

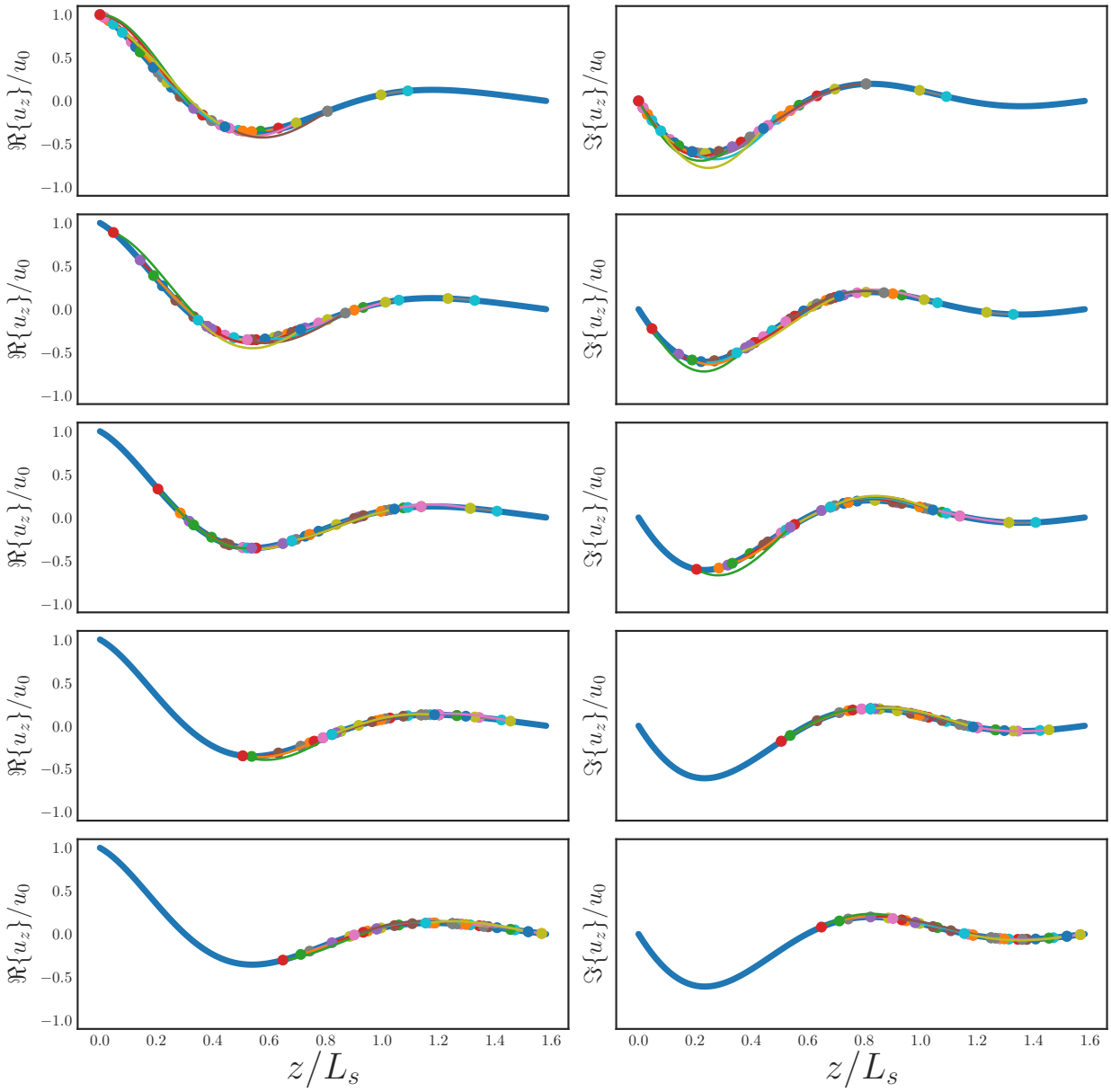

Figure A.1: Twenty of the smallest randomized subdomains used in each case (1 at top, 5 at bottom) Figure 2.9.

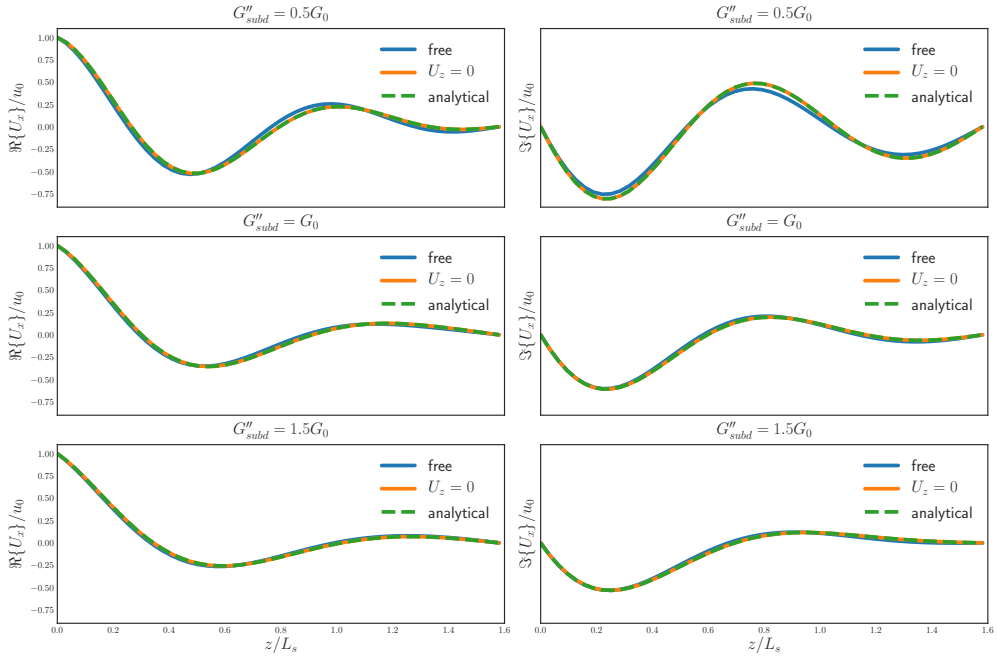

Figure A.2: A simple shear experiment is constructed inside the NLI framework for the finite element forward solution for a set of shear moduli values and compared with the 1D solution. The displacement is for the center of the domain, perpendicular to applied shear, and does not show any finite-domain effects.

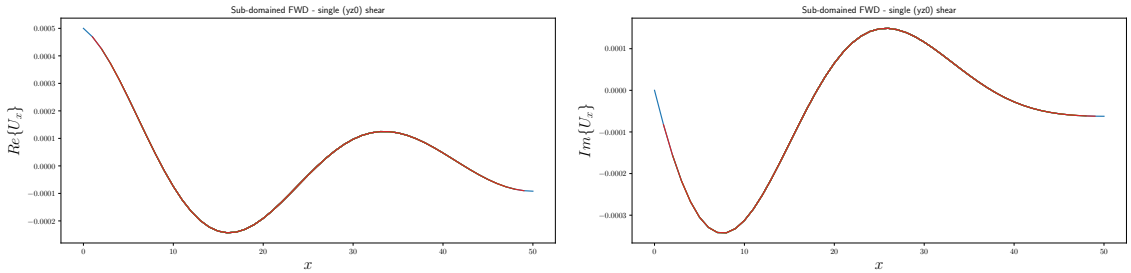

Figure A.3: Analytical simple shear, on the xy-face of a homogeneous isotropic analytical solution is used as the boundary condition for a isotropic NLI finite element forward solution. The FWD solution was then subdomain decomposed to test the effect of size of the domain. No effect was found for the finite domain solution where shear moduli were same as original.

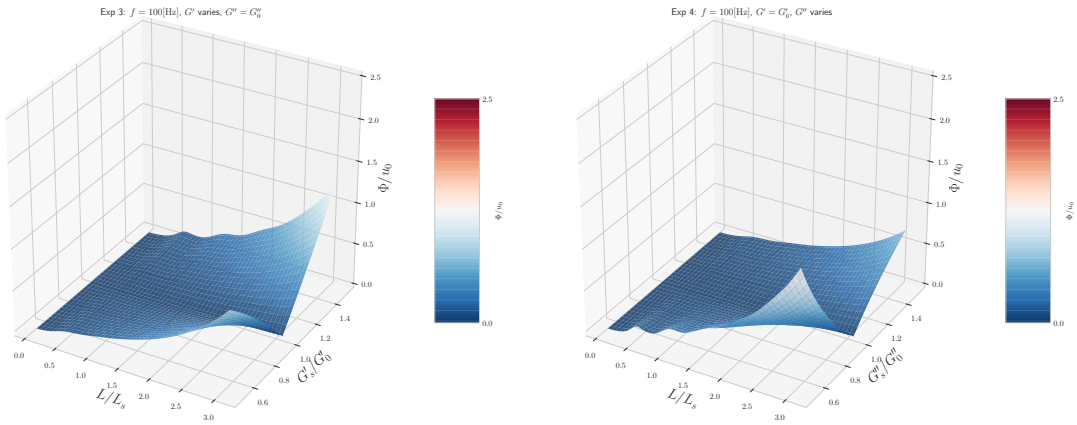

(a) (b)

Figure A.4: For constant domain size from Figure 2.7, the linear regression was computed for $G)subd < G_0$ (left) and $G_{subd} > G_0$ (right; negative for comparison). For small subdomains, the error is relatively insensitive to inaccuracies. For $G_{subd} < G_0$, the cost function is more sensitive to inaccuracies in G'' than G', and the converse is true for $G_{subd} > G_0$.

A.2 Transversely Isotropic

Since the 1D solution is a exact solution to the governing equations and any linear combinations of exact solutions are valid, Eq. (A.3) can be defined along two independent planes of shear for two different moduli resulting in a transversely isotropic (TI) analytical solution. An analytical TI solution provides an easy way to directly understand how the isotropic, but heterogeneous, NLI framework reconciles the wave field of a transversely isotropic material. This is an important simple model for understanding the behavior in highly-anisotropic regions of the human brain, like the corpus callosum (CC).

Using estimations for *in vivo* moduli in regions like CC and their respective ratio of properties (ξ), the two moduli for this study were $G = 2 + i1$ kPa and $G = 3 + i1.5$ kPa, ($\xi = 0.25$ for both) on a domain of size $31 \times 31 \times 31$ mm, with 1 mm^3 resolution. The two experimental cases are where the plane parallel and opposite to the applied shear is either free (Eq. A.5) or fixed (Eq. A.6). The excitation, $u_0 = 0.5$ mm, is applied along five separate angles rotating from only applied to the softer moduli, $\theta = 0°$, to the stiffer

moduli $\theta = 90°$. The results are summarized in Figure 5.12 for fixed case and Figure A.5 for free case. Additionally, the full isotropic reconstructed elastograms of the domain for the fixed case are shown in Figures A.6 for $\theta = 0$ and A.7 for $\theta = 45$. The $\theta = 45$ case shows the effects of two distinct moduli sheared equally in the structure of the estimated heterogeneous, isotropic material properties.

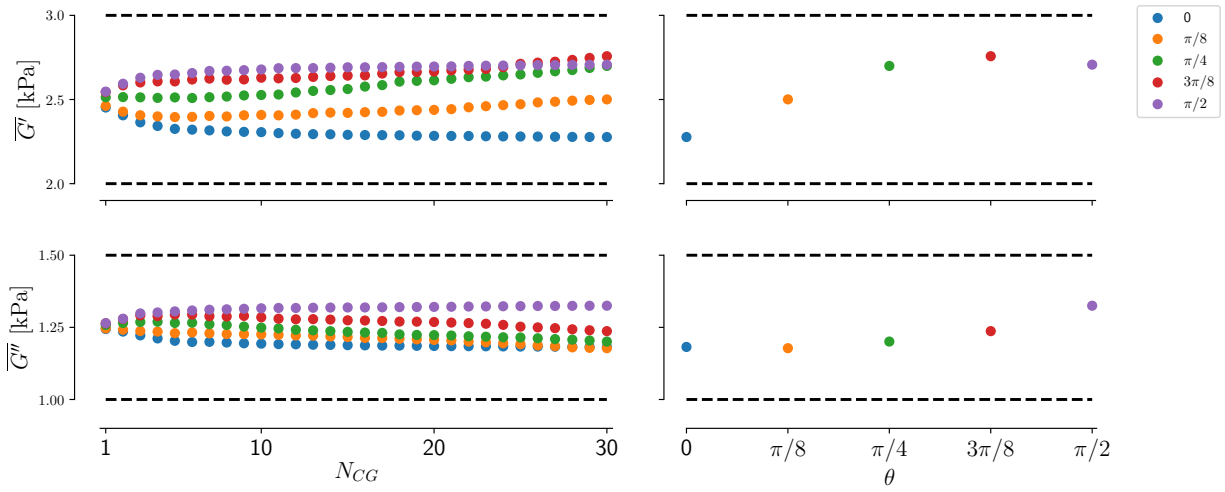

(a)

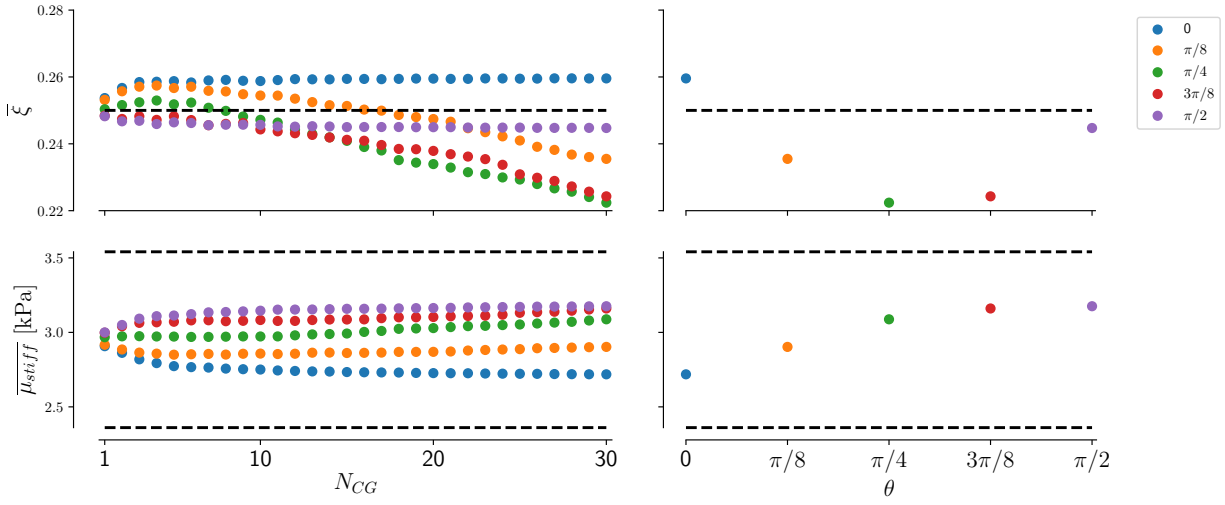

(b)

Figure A.5: Transversely isotropic analytical solution as the "measured" displacement field for a single subzone inversion. The actuation is applied to the lower shear moduli ($G = 2 + i1$ kPa) for $\theta = 0$ and rotated until only applied to stiffer moduli ($G = 3 + i1.5$ kPa) for $\theta = 90$, **free** opposite the applied shear.

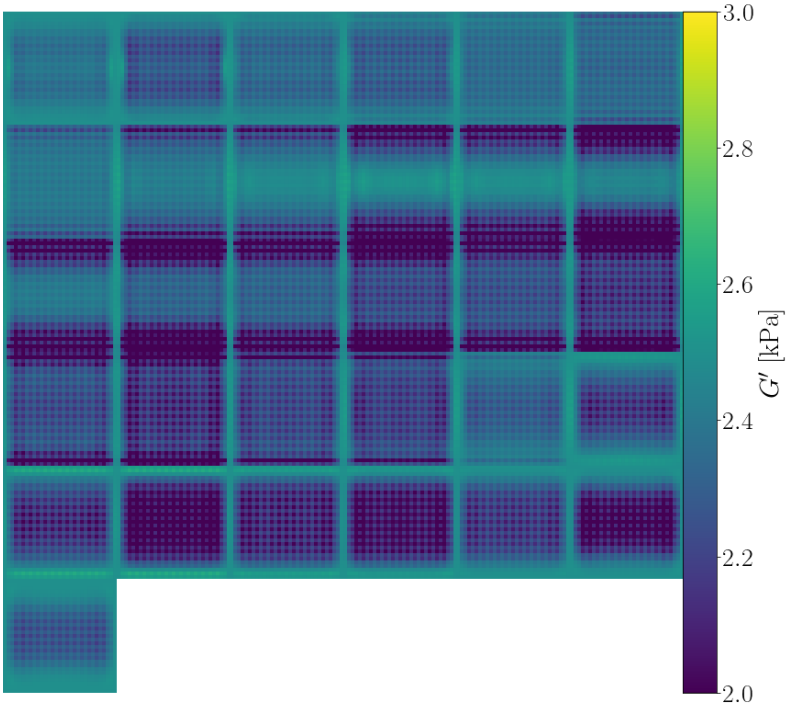

(a)

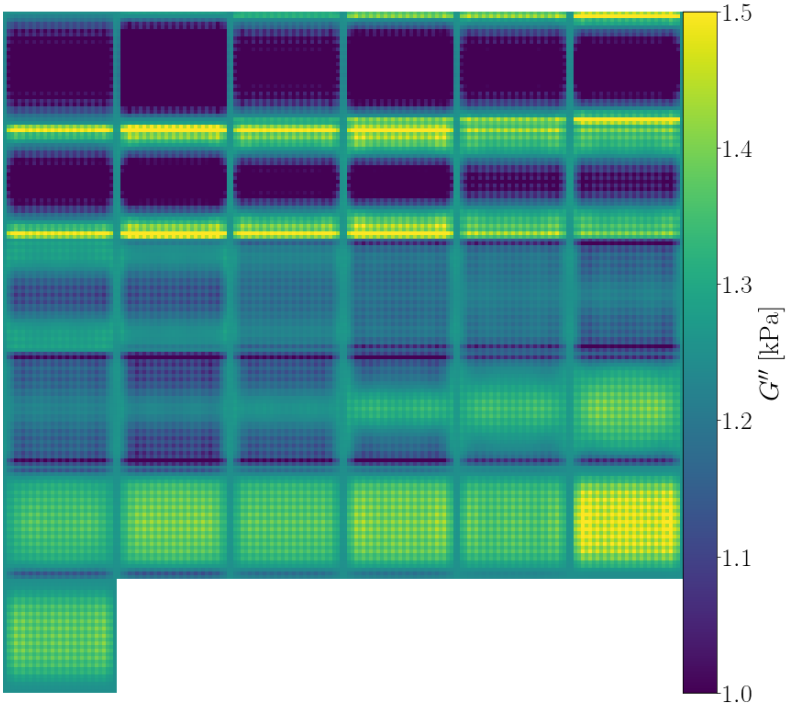

(b)

Figure A.6: For the **fixed** shear case from Figure 5.12 and $\theta = 0$, the full reconstructed elastograms using the isotropic model in NLI: (a) G' and (b) G''.

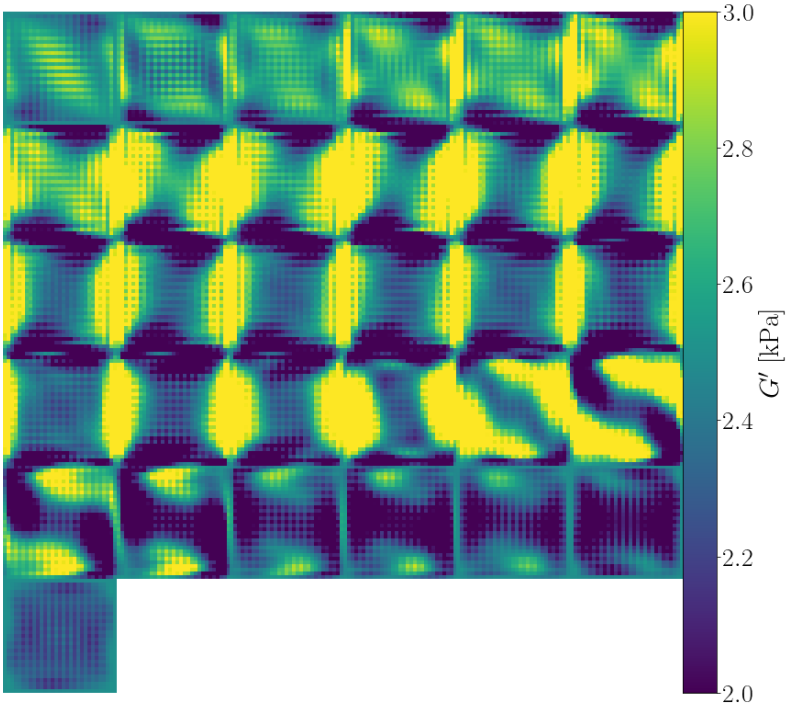

(a)

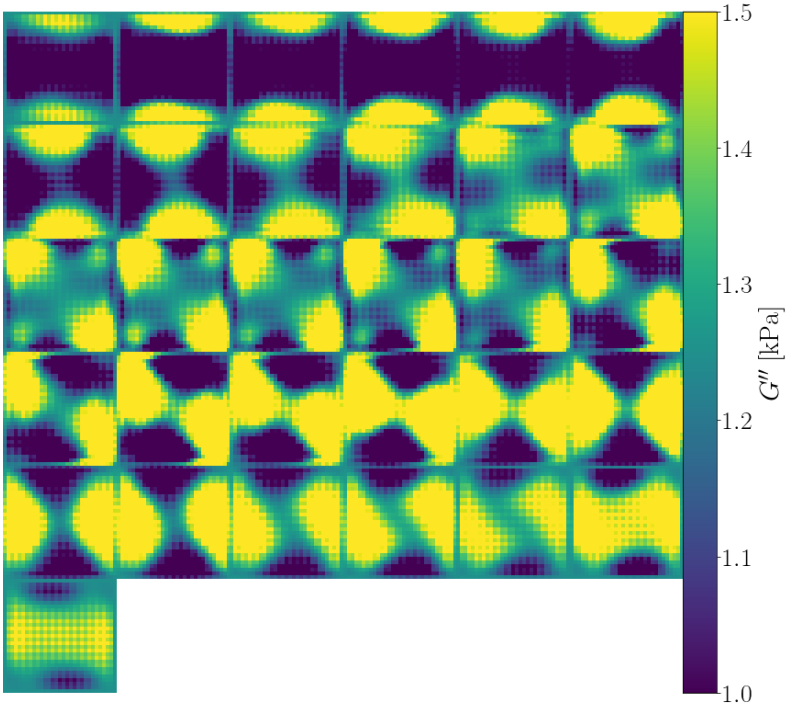

(b)

Figure A.7: For the **fixed** shear case from Figure 5.12 and $\theta = 45$, the full reconstructed elastograms using the isotropic model in NLI: (a) G' and (b) G''.

References

[1] K. Strimbu and J. A. Tavel, "What are biomarkers?" *Current opinion in HIV and AIDS*, vol. 5, no. 6, pp. 463–466, Nov. 2010.

[2] Biomarkers Definitions Working Group., "Biomarkers and surrogate endpoints: preferred definitions and conceptual framework." *Clinical pharmacology and therapeutics*, vol. 69, no. 3, pp. 89–95, Mar. 2001.

[3] R. Muthupillai, D. J. Lomas, P. J. Rossman, J. F. Greenleaf, A. Manduca, and R. L. Ehman, "Magnetic-Resonance Elastography by Direct Visualization of Propagating Acoustic Strain Waves," *Science*, vol. 269, no. 5232, pp. 1854–1857, 1995.

[4] A. Manduca, T. E. Oliphant, M. A. Dresner, J. L. Mahowald, S. A. Kruse, E. Amromin, J. P. Felmlee, J. F. Greenleaf, and R. L. Ehman, "Magnetic resonance elastography: Non-invasive mapping of tissue elasticity," *Medical Image Analysis*, vol. 5, no. 4, pp. 237–254, Dec. 2001.

[5] M. Yin, J. A. Talwalkar, K. J. Glaser, A. Manduca, R. C. Grimm, P. J. Rossman, J. L. Fidler, and R. L. Ehman, "Assessment of Hepatic Fibrosis With Magnetic Resonance Elastography," *Clinical Gastroenterology and Hepatology*, vol. 5, no. 10, pp. 1207–1213.e2, Oct. 2007.

[6] F. B. Freimann, K.-J. Streitberger, D. Klatt, K. Lin, J. McLaughlin, J. Braun, C. Sprung, and I. Sack, "Alteration of brain viscoelasticity after shunt treatment in normal pressure hydrocephalus," *Neuroradiology*, vol. 54, no. 3, pp. 189–196, May 2011.

[7] M. C. Murphy, J. Huston 3rd, C. R. Jack, K. J. Glaser, A. Manduca, J. P. Felmlee, and R. L. Ehman, "Decreased brain stiffness in Alzheimer's disease determined by magnetic resonance elastography." *Journal of Magnetic Resonance Imaging*, vol. 34, no. 3, pp. 494–498, Sep. 2011.

[8] W. C. Olivero, T. Wszalek, H. Wang, A. Farahvar, S. M. Rieth, and C. L. Johnson, "Magnetic Resonance Elastography Demonstrating Low Brain Stiffness in a Patient with Low-Pressure Hydrocephalus: Case Report." *Pediatric Neurosurgery*, vol. 51, no. 5, pp. 257–262, 2016.

[9] K.-J. Streitberger, M. Reiss-Zimmermann, F. B. Freimann, S. Bayerl, J. Guo, F. Arlt, J. Wuerfel, J. Braun, K.-T. Hoffmann, and I. Sack, "High-resolution mechanical imaging of glioblastoma by multifrequency magnetic resonance elastography," *PLoS ONE*, vol. 9, no. 10, p. e110588, Oct. 2014.

[10] K.-J. Streitberger, I. Sack, D. Krefting, C. Pfüller, J. Braun, F. Paul, and J. Wuerfel, "Brain viscoelasticity alteration in chronic-progressive multiple sclerosis," *PLoS ONE*, vol. 7, no. 1, p. e29888, Jan. 2012.

[11] K.-J. Streitberger, E. Wiener, J. Hoffmann, F. B. Freimann, D. Klatt, J. Braun, K. Lin, J. McLaughlin, C. Sprung, R. Klingebiel, and I. Sack, "In vivo viscoelastic properties of the brain in normal pressure hydrocephalus." *NMR in Biomedicine*, vol. 24, no. 4, pp. 385–392, May 2011.

[12] J. Wuerfel, F. Paul, B. Beierbach, U. Hamhaber, D. Klatt, S. Papazoglou, F. Zipp, P. Martus, J. Braun, and I. Sack, "MR-elastography reveals degradation of tissue integrity in multiple sclerosis," *NeuroImage*, vol. 49, no. 3, pp. 2520–2525, Feb. 2010.

[13] C. L. Johnson, H. Schwarb, M. D J McGarry, A. T. Anderson, G. R. Huesmann, B. P. Sutton, and N. J. Cohen, "Viscoelasticity of subcortical gray matter structures," *Human Brain Mapping*, vol. 37, no. 12, pp. 4221–4233, Dec. 2016.

[14] H. Schwarb, C. L. Johnson, M. D. McGarry, and N. J. Cohen, "Medial temporal lobe viscoelasticity and relational memory performance." *NeuroImage*, vol. 132, pp. 534–541, Feb. 2016.

[15] C. L. Johnson, H. Schwarb, K. M. Horecka, M. D. McGarry, C. H. Hillman, A. F. Kramer, N. J. Cohen, and A. K. Barbey, "Double dissociation of structure-function relationships in memory and fluid intelligence observed with magnetic resonance elastography," *NeuroImage*, vol. 171, pp. 99–106, May 2018.

[16] H. Schwarb, C. L. Johnson, A. M. Daugherty, C. H. Hillman, A. F. Kramer, N. J. Cohen, and A. K. Barbey, "Aerobic fitness, hippocampal viscoelasticity, and relational memory performance." *NeuroImage*, vol. 153, pp. 179–188, June 2017.

[17] Y. Feng, R. J. Okamoto, G. M. Genin, and P. V. Bayly, "On the accuracy and fitting of transversely isotropic material models," *Journal of the Mechanical Behavior of Biomedical Materials*, vol. 61, no. C, pp. 554–566, Aug. 2016.

[18] Y. Feng, R. J. Okamoto, R. Namani, G. M. Genin, and P. V. Bayly, "Measurements of mechanical anisotropy in brain tissue and implications for transversely isotropic material models of white matter," *Journal of the Mechanical Behavior of Biomedical Materials*, vol. 23, no. C, pp. 117–132, July 2013.

[19] R. Namani, M. D. Wood, S. E. Sakiyama-Elbert, and P. V. Bayly, "Anisotropic mechanical properties of magnetically aligned fibrin gels measured by magnetic resonance elastography," *Journal of Biomechanics*, vol. 42, no. 13, pp. 2047–2053, Sep. 2009.

[20] J. L. Schmidt, D. J. Tweten, A. N. Benegal, C. H. Walker, T. E. Portnoi, R. J. Okamoto, J. R. Garbow, and P. V. Bayly, "Magnetic resonance elastography of slow and fast shear waves illuminates differences in shear and tensile moduli in anisotropic tissue." *Journal of Biomechanics*, vol. 49, no. 7, pp. 1042–1049, Feb. 2016.

[21] D. J. Tweten, R. J. Okamoto, J. L. Schmidt, J. R. Garbow, and P. V. Bayly, "Estimation of material parameters from slow and fast shear waves in an incompressible, transversely isotropic material," *Journal of Biomechanics*, vol. 48, no. 15, pp. 4002–4009, Nov. 2015.

[22] A. Romano, M. Scheel, S. Hirsch, J. Braun, and I. Sack, "In vivo waveguide elastography of white matter tracts in the human brain." *Magnetic Resonance in Medicine*, vol. 68, no. 5, pp. 1410–1422, Nov. 2012.

[23] A. J. Romano, P. B. Abraham, P. J. Rossman, J. A. Bucaro, and R. L. Ehman, "Determination and analysis of guided wave propagation using magnetic resonance elastography," *Magnetic Resonance in Medicine*, vol. 54, no. 4, pp. 893–900, Oct. 2005.

[24] E. E. W. Van Houten, K. D. Paulsen, M. I. Miga, F. E. Kennedy, and J. B. Weaver, "An overlapping subzone technique for MR-based elastic property reconstruction," *Magnetic Resonance in Medicine*, vol. 42, no. 4, pp. 779–786, 1999.

[25] E. E. W. Van Houten, M. I. Miga, J. B. Weaver, F. E. Kennedy, and K. D. Paulsen, "Three-dimensional subzone-based reconstruction algorithm for MR elastography," *Magnetic Resonance in Medicine*, vol. 45, no. 5, pp. 827–837, 2001.

[26] E. E. W. Van Houten, D. v. Viviers, M. D. J. McGarry, P. R. Perriñez, I. I. Perreard, J. B. Weaver, and K. D. Paulsen, "Subzone based magnetic resonance elastography using a Rayleigh damped material model," *Medical Physics*, vol. 38, no. 4, pp. 1993–2004, 2011.

[27] M. D. J. McGarry, E. E. W. Van Houten, C. L. Johnson, J. G. Georgiadis, B. P. Sutton, J. B. Weaver, and K. D. Paulsen, "Multiresolution MR elastography using nonlinear inversion," *Medical Physics*, vol. 39, no. 10, pp. 6388–6396, Oct. 2012.

[28] A. A. Oberai, N. H. Gokhale, and G. R. Feijóo, "Solution of inverse problems in elasticity imaging using the adjoint method," *Inverse Problems*, vol. 19, no. 2, pp. 297–313, Apr. 2003.

[29] M. D. McGarry, H.-U. Berger, and E. E. W. Van Houten, "Damping models in elastography," in *Progress in Biomedical Optics and Imaging - Proceedings of SPIE*. University of Canterbury, Christchurch, New Zealand, Oct. 2007.

[30] L. Tan, M. D. McGarry, E. E. W. Van Houten, M. Ji, L. Solamen, J. B. Weaver, and K. D. Paulsen, "Gradient-based optimization for poroelastic and viscoelastic MR elastography," *IEEE Transactions on Medical Imaging*, vol. 36, no. 1, pp. 236–250, Jan. 2017.

[31] M. D. McGarry, "Improvement and Evaluation of Nonlinear Inversion MR Elastography," pp. 1–191, Jan. 2013.

[32] I. Sack, K. Jöhrens, J. Würfel, and J. Braun, "Structure-sensitive elastography: on the viscoelastic powerlaw behavior of in vivo human tissue in health and disease," *Soft Matter*, vol. 9, no. 24, p. 5672, 2013.

[33] H. Tzschätzsch, J. Guo, F. Dittmann, S. Hirsch, E. Barnhill, K. Jöhrens, J. Braun, and I. Sack, "Tomoelastography by multifrequency wave number recovery from time-harmonic propagating shear waves." *Medical Image Analysis*, vol. 30, pp. 1–10, May 2016.

[34] F. Dittmann, S. Hirsch, H. Tzschätzsch, J. Guo, J. Braun, and I. Sack, "In vivo wideband multifrequency MR elastography of the human brain and liver." *Magnetic Resonance in Medicine*, vol. 76, no. 4, pp. 1116–1126, Oct. 2016.

[35] J. Testu, M. D. J. McGarry, F. Dittmann, J. B. Weaver, K. D. Paulsen, I. Sack, and E. E. W. Van Houten, "Viscoelastic power law parameters of in vivo human brain estimated by MR elastography," *Journal of the Mechanical Behavior of Biomedical Materials*, vol. 74, pp. 333–341, Oct. 2017.

[36] C. L. Johnson, M. D. McGarry, E. E. W. Van Houten, J. B. Weaver, K. D. Paulsen, B. P. Sutton, and J. G. Georgiadis, "Magnetic resonance elastography of the brain using multishot spiral readouts with self-navigated motion correction," *Magnetic Resonance in Medicine*, vol. 70, no. 2, pp. 404–412, Sep. 2012.

[37] C. L. Johnson, J. L. Holtrop, M. D. McGarry, J. B. Weaver, K. D. Paulsen, J. G. Georgiadis, and B. P. Sutton, "3D multislab, multishot acquisition for fast, whole-brain MR elastography with high signal-to-noise efficiency," *Magnetic Resonance in Medicine*, vol. 71, no. 2, pp. 477–485, Feb. 2014.

[38] C. L. Johnson, M. D. McGarry, A. A. Gharibans, J. B. Weaver, K. D. Paulsen, H. Wang, W. C. Olivero, B. P. Sutton, and J. G. Georgiadis, "Local mechanical properties of white matter structures in the human brain," *NeuroImage*, vol. 79, pp. 145–152, Oct. 2013.

[39] L. V. Hiscox, C. L. Johnson, E. Barnhill, M. D. J. McGarry, J. Huston 3rd, E. J. R. van Beek, J. M. Starr, and N. Roberts, "Magnetic resonance elastography (MRE) of the human brain: Technique, findings and clinical applications," *Physics in Medicine and Biology*, vol. 61, no. 24, pp. R401–R437, Nov. 2016.

[40] B. M. Sandroff, C. L. Johnson, and R. W. Motl, "Exercise training effects on memory and hippocampal viscoelasticity in multiple sclerosis: a novel application of magnetic resonance elastography," *Neuroradiology*, vol. 59, no. 1, pp. 61–67, Jan. 2017.

[41] C. L. Johnson and E. H. Telzer, "Magnetic Resonance Elastography for Examining Developmental Changes in the Mechanical Properties of the Brain," *Developmental Cognitive Neuroscience*, Sep. 2017.

[42] R. S. Lakes, *Viscoelastic Materials*. Cambridge University Press, Apr. 2009.

[43] T. E. Oliphant, A. Manduca, R. L. Ehman, and J. F. Greenleaf, "Complex-valued stiffness reconstruction for magnetic resonance elastography by algebraic inversion of the differential equation," *Magnetic Resonance in Medicine*, vol. 45, no. 2, pp. 299–310, Feb. 2001.

[44] K. Franze, P. A. Janmey, and J. Guck, "Mechanics in neuronal development and repair." *Annual Review of Biomedical Engineering*, vol. 15, no. 1, pp. 227–251, 2013.

[45] X. Tang, T. B. Kuhlenschmidt, Q. Li, S. Ali, S. Lezmi, H. Chen, M. Pires-Alves, W. W. Laegreid, T. A. Saif, and M. S. Kuhlenschmidt, "A mechanically-induced colon cancer cell population shows increased metastatic potential," *Molecular Cancer*, vol. 13, no. 1, p. 131, May 2014.

[46] J.-W. E. Chen, S. Pedron, and B. A. C. Harley, "The Combined Influence of Hydrogel Stiffness and Matrix-Bound Hyaluronic Acid Content on Glioblastoma Invasion," *Macromolecular Bioscience*, vol. 17, no. 8, Aug. 2017.

[47] S. Pedron, H. Polishetty, A. M. Pritchard, B. P. Mahadik, J. N. Sarkaria, and B. A. C. Harley, "Spatially graded hydrogels for preclinical testing of glioblastoma anticancer therapeutics." *MRS communications*, vol. 7, no. 3, pp. 442–449, Sep. 2017.

[48] C. Werner and K. Engelhard, "Pathophysiology of traumatic brain injury," *BJA: British Journal of Anaesthesia*, vol. 99, no. 1, pp. 4–9, July 2007.

[49] Y. Zhou, "Small world properties changes in mild traumatic brain injury," *Journal of Magnetic Resonance Imaging*, vol. 46, no. 2, pp. 518–527, Nov. 2016.

[50] S. Siechen, S. Yang, A. Chiba, and T. Saif, "Mechanical tension contributes to clustering of neurotransmitter vesicles at presynaptic terminals," *Proceedings of the National Academy of Sciences of the United States of America*, vol. 106, no. 31, pp. 12 611–12 616, Aug. 2009.

[51] X. Tang, A. Tofangchi, S. V. Anand, and T. A. Saif, "A novel cell traction force microscopy to study multi-cellular system." *PLoS Computational Biology*, vol. 10, no. 6, p. e1003631, June 2014.

[52] W. W. Ahmed and T. A. Saif, "Active transport of vesicles in neurons is modulated by mechanical tension." *Scientific Reports*, vol. 4, no. 1, p. 4481, Mar. 2014.

[53] D. E. Discher, P. Janmey, and Y.-L. Wang, "Tissue cells feel and respond to the stiffness of their substrate." *Science*, vol. 310, no. 5751, pp. 1139–1143, Nov. 2005.

[54] M. G. Mendez and P. A. Janmey, "Transcription factor regulation by mechanical stress." *The international journal of biochemistry & cell biology*, vol. 44, no. 5, pp. 728–732, May 2012.

[55] K. Pogoda, L. Chin, P. C. Georges, F. J. Byfield, R. Bucki, R. Kim, M. Weaver, R. G. Wells, C. Marcinkiewicz, and P. A. Janmey, "Compression stiffening of brain and its effect on mechanosensing by glioma cells," *New Journal of Physics*, vol. 16, no. 7, p. 075002, July 2014.

[56] A. W. Holle, J. L. Young, K. J. Van Vliet, R. D. Kamm, D. Discher, P. Janmey, J. P. Spatz, and T. Saif, "Cell-Extracellular Matrix Mechanobiology: Forceful Tools and Emerging Needs for Basic and Translational Research." *Nano letters*, vol. 18, no. 1, pp. 1–8, Jan. 2018.

[57] S. W. Davis, N. A. Dennis, N. G. Buchler, L. E. White, D. J. Madden, and R. Cabeza, "Assessing the effects of age on long white matter tracts using diffusion tensor tractography," *NeuroImage*, vol. 46, no. 2, pp. 530–541, June 2009.

[58] E. V. Sullivan, T. Rohlfing, and A. Pfefferbaum, "Quantitative fiber tracking of lateral and interhemispheric white matter systems in normal aging: relations to timed performance." *Neurobiology of Aging*, vol. 31, no. 3, pp. 464–481, Mar. 2010.

[59] F. Branzoli, E. Ercan, R. Valabrègue, E. T. Wood, M. Buijs, A. Webb, and I. Ronen, "Differentiating between axonal damage and demyelination in healthy aging by combining diffusion-tensor imaging and diffusion-weighted spectroscopy in the human corpus callosum at 7 T." *Neurobiology of Aging*, vol. 47, pp. 210–217, Nov. 2016.

[60] S. R. Cox, S. J. Ritchie, E. M. Tucker-Drob, D. C. Liewald, S. P. Hagenaars, G. Davies, J. M. Wardlaw, C. R. Gale, M. E. Bastin, and I. J. Deary, "Ageing and brain white matter structure in 3,513 UK Biobank participants," *Nature Communications*, vol. 7, p. 13629, Dec. 2016.

[61] K. L. Spalding, O. Bergmann, K. Alkass, S. Bernard, M. Salehpour, H. B. Huttner, E. Boström, I. Westerlund, C. Vial, B. A. Buchholz, G. Possnert, D. C. Mash, H. Druid, and J. Frisén, "Dynamics of Hippocampal Neurogenesis in Adult Humans," *Cell*, vol. 153, no. 6, pp. 1219–1227, June 2013.

[62] S. F. Sorrells, M. F. Paredes, A. Cebrian-Silla, K. Sandoval, D. Qi, K. W. Kelley, D. James, S. Mayer, J. Chang, K. I. Auguste, E. F. Chang, A. J. Gutierrez, A. R. Kriegstein, G. W. Mathern, M. C. Oldham, E. J. Huang, J. M. Garcia-Verdugo, Z. Yang, and A. Alvarez-Buylla, "Human hippocampal neurogenesis drops sharply in children to undetectable levels in adults." *Nature*, vol. 555, no. 7696, pp. 377–381, Mar. 2018.

[63] A. Arani, H.-K. Min, N. Fattahi, N. M. Wetjen, J. D. Trzasko, A. Manduca, C. R. Jack, K. H. Lee, R. L. Ehman, and J. Huston 3rd, "Acute pressure changes in the brain are correlated with MR elastography stiffness measurements: initial feasibility in an in vivo large animal model." *Magnetic Resonance in Medicine*, vol. 79, no. 2, pp. 1043–1051, Feb. 2018.

[64] N. Fattahi, A. Arani, A. Perry, F. Meyer, A. Manduca, K. Glaser, M. L. Senjem, R. L. Ehman, and J. Huston, "MR Elastography Demonstrates Increased Brain Stiffness in Normal Pressure Hydrocephalus," *American Journal of Neuroradiology*, vol. 37, no. 3, pp. 462–467, Mar. 2016.

[65] C. Storm, J. J. Pastore, F. C. MacKintosh, T. C. Lubensky, and P. A. Janmey, "Nonlinear elasticity in biological gels," *Nature*, vol. 435, no. 7039, pp. 191–194, 2005.

[66] S. R. Mousavi, A. Fehlner, K.-J. Streitberger, J. Braun, A. Samani, and I. Sack, "Measurement of in vivo cerebral volumetric strain induced by the Valsalva maneuver," *Journal of Biomechanics*, vol. 47, no. 7, pp. 1652–1657, May 2014.

[67] S. Hirsch, F. Beyer, J. Guo, S. Papazoglou, H. Tzschaetzsch, J. Braun, and I. Sack, "Compression-sensitive magnetic resonance elastography," *Physics in Medicine and Biology*, vol. 58, no. 15, pp. 5287–5299, July 2013.

[68] A. Manduca, R. Muthupillai, P. J. Rossman, J. F. Greenleaf, and R. L. Ehman, "Local wavelength estimation for magnetic resonance elastography," in *3rd IEEE International Conference on Image Processing*. IEEE, Sep. 1996, pp. 527–530.

[69] E. H. Clayton, G. M. Genin, and P. V. Bayly, "Transmission, attenuation and reflection of shear waves in the human brain." *Journal of the Royal Society, Interface / the Royal Society*, vol. 9, no. 76, pp. 2899–2910, Nov. 2012.

[70] D. M. McGrath, N. Ravikumar, L. Beltrachini, I. D. Wilkinson, A. F. Frangi, and Z. A. Taylor, "Evaluation of wave delivery methodology for brain MRE: Insights from computational simulations," *Magnetic Resonance in Medicine*, vol. 78, no. 1, pp. 341–356, July 2017.

[71] A. A. Badachhape, R. J. Okamoto, R. S. Durham, B. D. Efron, S. J. Nadell, C. L. Johnson, and P. V. Bayly, "The Relationship of Three-Dimensional Human Skull Motion to Brain Tissue Deformation in Magnetic Resonance Elastography Studies." *Journal of Biomechanical Engineering*, vol. 139, no. 5, p. 12, May 2017.

[72] C. Giordano, R. J. H. Cloots, J. A. W. van Dommelen, and S. Kleiven, "The influence of anisotropy on brain injury prediction," *Journal of Biomechanics*, vol. 47, no. 5, pp. 1052–1059, Mar. 2014.

[73] C. Giordano, S. Zappalà, and S. Kleiven, "Anisotropic finite element models for brain injury prediction: the sensitivity of axonal strain to white matter tract inter-subject variability," *Biomechanics and Modeling in Mechanobiology*, vol. 16, no. 4, pp. 1269–1293, Feb. 2017.

[74] A. Romano, J. Guo, T. Prokscha, T. Meyer, S. Hirsch, J. Braun, I. Sack, and M. Scheel, "In vivo waveguide elastography: effects of neurodegeneration in patients with amyotrophic lateral sclerosis." *Magnetic Resonance in Medicine*, vol. 72, no. 6, pp. 1755–1761, Dec. 2014.

[75] L. V. Hiscox, C. L. Johnson, M. D. McGarry, M. Perrins, A. Littlejohn, E. J. R. van Beek, N. Roberts, and J. M. Starr, "High-resolution magnetic resonance elastography reveals differences in subcortical gray matter viscoelasticity between young and healthy older adults." *Neurobiology of Aging*, vol. 65, pp. 158–167, May 2018.

[76] A. Arani, M. C. Murphy, K. J. Glaser, A. Manduca, D. S. Lake, S. A. Kruse, C. R. Jack, R. L. Ehman, and J. Huston 3rd, "Measuring the effects of aging and sex on regional brain stiffness with MR elastography in healthy older adults." *NeuroImage*, vol. 111, pp. 59–64, May 2015.

[77] M. T. Prange and S. S. Margulies, "Regional, directional, and age-dependent properties of the brain undergoing large deformation," *Journal of Biomechanical Engineering*, vol. 124, no. 2, pp. 244–252, Apr. 2002.

[78] I. Sack, B. Beierbach, J. Wuerfel, D. Klatt, U. Hamhaber, S. Papazoglou, P. Martus, and J. Braun, "The impact of aging and gender on brain viscoelasticity," *NeuroImage*, vol. 46, no. 3, pp. 652–657, July 2009.

[79] C. L. Johnson and J. G. Georgiadis, "Imaging the local mechanical properties of the brain with high-resolution magnetic resonance elastography," Ph.D. dissertation, Urbana, IL, July 2013.

[80] M. M. Doyley, P. M. Meaney, and J. C. Bamber, "Evaluation of an iterative reconstruction method for quantitative elastography," *Physics in Medicine and Biology*, vol. 45, no. 6, pp. 1521–1540, June 2000.

[81] E. Van Houten, "Mechanical Property Reconstruction from MR Detected Harmonic Displacement Data," Ph.D. dissertation, Hanover, Aug. 2001.

[82] M. M. Doyley, Q. Feng, J. B. Weaver, and K. D. Paulsen, "Performance analysis of steady-state harmonic elastography," *Physics in Medicine and Biology*, vol. 52, no. 10, pp. 2657–2674, Apr. 2007.

[83] K. P. McGee, D. Lake, Y. Mariappan, R. D. Hubmayr, A. Manduca, K. Ansell, and R. L. Ehman, "Calculation of shear stiffness in noise dominated magnetic resonance elastography data based on principal frequency estimation," *Physics in Medicine and Biology*, vol. 56, no. 14, pp. 4291–4309, June 2011.

[84] T. E. J. Behrens, M. W. Woolrich, M. Jenkinson, H. Johansen-Berg, R. G. Nunes, S. Clare, P. M. Matthews, J. M. Brady, and S. M. Smith, "Characterization and propagation of uncertainty in diffusion-weighted MR imaging," *Magnetic Resonance in Medicine*, vol. 50, no. 5, pp. 1077–1088, Nov. 2003.

[85] K. Oishi, A. V. Faria, P. C. M. van Zijl, and S. Mori, *MRI Atlas of Human White Matter*. Academic Press, Nov. 2010.

[86] M. Yin, K. J. Glaser, J. A. Talwalkar, J. Chen, A. Manduca, and R. L. Ehman, "Hepatic MR elastography: Clinical performance in a series of 1377 consecutive examinations," *Radiology*, vol. 278, no. 1, pp. 114–124, Jan. 2016.

[87] M. D. J. McGarry, E. E. W. Van Houten, P. R. Perriñez, A. J. Pattison, J. B. Weaver, and K. D. Paulsen, "An octahedral shear strain-based measure of SNR for 3D MR elastography," *Physics in Medicine and Biology*, vol. 56, no. 13, pp. N153–N164, June 2011.

[88] Z. Yin, J. D. Hughes, K. J. Glaser, A. Manduca, J. Van Gompel, M. J. Link, A. Romano, R. L. Ehman, and J. Huston 3rd, "Slip interface imaging based on MR-elastography preoperatively predicts meningioma-brain adhesion." *Journal of Magnetic Resonance Imaging*, vol. 46, no. 4, pp. 1007–1016, Oct. 2017.

[89] D. J. Tweten, R. J. Okamoto, and P. V. Bayly, "Requirements for accurate estimation of anisotropic material parameters by magnetic resonance elastography: A computational study," *Magnetic Resonance in Medicine*, vol. 78, no. 6, pp. 2360–2372, Jan. 2017.

[90] S. K. Venkatesh, M. Yin, and R. L. Ehman, "Magnetic resonance elastography of liver: technique, analysis, and clinical applications." *Journal of Magnetic Resonance Imaging*, vol. 37, no. 3, pp. 544–555, Mar. 2013.

[91] A. Lipp, R. Trbojevic, F. Paul, A. Fehlner, S. Hirsch, M. Scheel, C. Noack, J. Braun, and I. Sack, "Cerebral magnetic resonance elastography in supranuclear palsy and idiopathic Parkinson's disease," *NeuroImage : Clinical*, vol. 3, pp. 381–387, 2013.

[92] J. Huston 3rd, M. C. Murphy, B. F. Boeve, N. Fattahi, A. Arani, K. J. Glaser, A. Manduca, D. T. Jones, and R. L. Ehman, "Magnetic resonance elastography of frontotemporal dementia," *Journal of Magnetic Resonance Imaging*, vol. 43, no. 2, pp. 474–478, 2015.

[93] R. Sinkus, M. Tanter, S. Catheline, J. Lorenzen, C. Kuhl, E. Sondermann, and M. Fink, "Imaging anisotropic and viscous properties of breast tissue by magnetic resonance-elastography," *Magnetic Resonance in Medicine*, vol. 53, no. 2, pp. 372–387, Feb. 2005.

[94] E. C. Qin, R. Sinkus, G. Geng, S. Cheng, M. Green, C. D. Rae, and L. E. Bilston, "Combining MR elastography and diffusion tensor imaging for the assessment of anisotropic mechanical properties: A phantom study," *Journal of Magnetic Resonance Imaging*, vol. 37, no. 1, pp. 217–226, Jan. 2013.

[95] E. C. Qin, L. Jugé, S. A. Lambert, V. Paradis, R. Sinkus, and L. E. Bilston, "In vivo anisotropic mechanical properties of dystrophic skeletal muscles measured by anisotropic MR elastographic imaging: the mdx mouse model of muscular dystrophy," *Radiology*, vol. 273, no. 3, pp. 726–735, Dec. 2014.

[96] F. Velardi, F. Fraternali, and M. Angelillo, "Anisotropic constitutive equations and experimental tensile behavior of brain tissue." *Biomechanics and Modeling in Mechanobiology*, vol. 5, no. 1, pp. 53–61, Mar. 2006.

[97] J. Guo, S. Hirsch, M. Scheel, J. Braun, and I. Sack, "Three-parameter shear wave inversion in MR elastography of incompressible transverse isotropic media: application to in vivo lower leg muscles," *Magnetic Resonance in Medicine*, vol. 75, no. 4, pp. 1537–1545, 2015.

[98] S. Ipek-Ugay, T. Driessle, M. Ledwig, J. Guo, S. Hirsch, I. Sack, and J. Braun, "Table-top magnetic resonance elastography for the measurement of viscoelastic parameters of small tissue samples," *Journal of Magnetic Resonance*, vol. 251, pp. 13–18, Feb. 2015.

[99] S. A. Kruse, J. A. Smith, A. J. Lawrence, M. A. Dresner, A. Manduca, J. F. Greenleaf, and R. L. Ehman, "Tissue characterization using magnetic resonance elastography: Preliminary results," *Physics in Medicine and Biology*, vol. 45, no. 6, pp. 1579–1590, June 2000.

[100] J. B. Weaver, T. B. Miller, P. R. Perrinez, M. M. Doyley, H. Wang, Y. Y. Cheung, J. S. Wrobel, R. J. Comi, F. E. Kennedy, and K. D. Paulsen, "MR elastographic methods for the evaluation of plantar fat pads: Preliminary comparison of the shear modulus for shearing deformation and compressive deformation in normal subjects," in *Progress in Biomedical Optics and Imaging - Proceedings of SPIE*, A. Manduca and A. A. Amini, Eds. Dartmouth Hitchcock Medical Center, Lebanon, United States, June 2006.

[101] G. Geng, M. Green, C. Rae, R. Sinkus, R. G. Henry, and L. E. Bilston, "Diffusion Tensor Imaging Enhanced Anisotropic MRE of the Brain," in *23rd Annual Meeting of ISMRM*, 2013.

[102] A. T. Anderson, C. L. Johnson, J. L. Holtrop, M. D. McGarry, E. E. W. Van Houten, K. D. Paulsen, B. P. Sutton, and J. G. Georgiadis, "Property Differences in White Matter Structures due to Distinct Wave Propagation Directions in MR Elastography," in *23rd Annual Meeting of ISMRM*, 2015.

[103] S. Mori, K. Oishi, H. Jiang, L. Jiang, X. Li, K. Akhter, K. Hua, A. V. Faria, A. Mahmood, R. Woods, A. W. Toga, G. B. Pike, P. R. Neto, A. Evans, J. Zhang, H. Huang, M. I. Miller, P. van Zijl, and J. Mazziotta, "Stereotaxic white matter atlas based on diffusion tensor imaging in an ICBM template." *NeuroImage*, vol. 40, no. 2, pp. 570–582, Apr. 2008.

[104] S. M. Smith, M. Jenkinson, H. Johansen-Berg, D. Rueckert, T. E. Nichols, C. E. Mackay, K. E. Watkins, O. Ciccarelli, M. Z. Cader, P. M. Matthews, and T. E. J. Behrens, "Tract-based spatial statistics: voxelwise analysis of multi-subject diffusion data." *NeuroImage*, vol. 31, no. 4, pp. 1487–1505, July 2006.

[105] Y. Zhang, M. Brady, and S. Smith, "Segmentation of brain MR images through a hidden Markov random field model and the expectation-maximization algorithm," *IEEE Transactions on Medical Imaging*, vol. 20, no. 1, pp. 45–57, 2001.

[106] C. L. Johnson, H. Schwarb, M. D. McGarry, B. P. Sutton, and N. J. Cohen, "Viscoelasticity of Subcortical Gray Matter Structures," in *23rd Annual Meeting of ISMRM*, 2015.

[107] F. Aboitiz and J. Montiel, "One hundred million years of interhemispheric communication: the history of the corpus callosum," *Braz J Med Biol Res*, vol. 36, no. 4, pp. 409–420, Apr. 2003.

[108] E. Mace, I. Cohen, G. Montaldo, R. Miles, M. Fink, and M. Tanter, "In Vivo Mapping of Brain Elasticity in Small Animals Using Shear Wave Imaging," *IEEE Transactions on Medical Imaging*, vol. 30, no. 3, pp. 550–558, Mar. 2011.

[109] I. M. Perreard, A. J. Pattison, M. Doyley, M. D. J. McGarry, Z. Barani, E. E. Van Houten, J. B. Weaver, and K. D. Paulsen, "Effects of frequency- and direction-dependent elastic materials on linearly elastic MRE image reconstructions." *Physics in Medicine and Biology*, vol. 55, no. 22, pp. 6801–6815, Nov. 2010.

[110] M. A. Green, G. Geng, E. Qin, R. Sinkus, S. C. Gandevia, and L. E. Bilston, "Measuring anisotropic muscle stiffness properties using elastography." *NMR in Biomedicine*, vol. 26, no. 11, pp. 1387–1394, Nov. 2013.

[111] D. Klatt, C. L. Johnson, and R. L. Magin, "Simultaneous, multidirectional acquisition of displacement fields in magnetic resonance elastography of the in vivo human brain," *Journal of Magnetic Resonance Imaging*, vol. 42, no. 2, pp. 297–304, Aug. 2015.

[112] I. Sack, B. Beierbach, U. Hamhaber, D. Klatt, and J. Braun, "Non-invasive measurement of brain viscoelasticity using magnetic resonance elastography," *NMR in Biomedicine*, vol. 21, no. 3, pp. 265–271, Apr. 2008.

[113] S. A. Kruse, G. H. Rose, K. J. Glaser, A. Manduca, J. P. Felmlee, C. R. Jack, and R. L. Ehman, "Magnetic resonance elastography of the brain," *NeuroImage*, vol. 39, no. 1, pp. 231–237, Jan. 2008.

[114] M. A. Green, L. E. Bilston, and R. Sinkus, "In vivo brain viscoelastic properties measured by magnetic resonance elastography," *NMR in Biomedicine*, vol. 21, no. 7, pp. 755–764, Aug. 2008.

[115] U. Hamhaber, D. Klatt, S. Papazoglou, M. Hollmann, J. Stadler, I. Sack, J. Bernarding, and J. Braun, "In vivo magnetic resonance elastography of human brain at 7 T and 1.5 T," *Journal of Magnetic Resonance Imaging*, vol. 32, no. 3, pp. 577–583, Sep. 2010.

[116] P. Latta, M. L. H. Gruwel, P. Debergue, B. Matwiy, U. N. Sboto-Frankenstein, and B. Tomanek, "Convertible pneumatic actuator for magnetic resonance elastography of the brain," *Magnetic Resonance Imaging*, vol. 29, no. 1, pp. 147–152, Jan. 2011.

[117] D. Gallichan, M. D. Robson, A. Bartsch, and K. L. Miller, "TREMR: Table-resonance elastography with MR," *Magnetic Resonance in Medicine*, vol. 62, no. 3, pp. 815–821, Sep. 2009.

[118] J. L. Schmidt, D. J. Tweten, A. A. Badachhape, A. J. Reiter, R. J. Okamoto, J. R. Garbow, and P. V. Bayly, "Measurement of anisotropic mechanical properties in porcine brain white matter ex vivo using magnetic resonance elastography," *Journal of the Mechanical Behavior of Biomedical Materials*, vol. 79, pp. 30–37, Dec. 2017.

[119] C. A. Guertler, R. J. Okamoto, J. L. Schmidt, A. A. Badachhape, C. L. Johnson, and P. V. Bayly, "Mechanical Properties of Porcine Brain Tissue In Vivo and Ex Vivo Estimated by MR Elastography," *Journal of Biomechanics*, pp. 1–37, Jan. 2018.

[120] K. Wu, Y. Taki, K. Sato, S. Kinomura, R. Goto, K. Okada, R. Kawashima, Y. He, A. C. Evans, and H. Fukuda, "Age-related changes in topological organization of structural brain networks in healthy individuals." *Human Brain Mapping*, vol. 33, no. 3, pp. 552–568, Mar. 2012.

[121] R. Cabeza, N. D. Anderson, J. K. Locantore, and A. R. McIntosh, "Aging gracefully: Compensatory brain activity in high-performing older adults," *NeuroImage*, vol. 17, no. 3, pp. 1394–1402, Nov. 2002.

[122] A. T. Anderson, E. E. W. Van Houten, M. D. McGarry, K. D. Paulsen, J. L. Holtrop, B. P. Sutton, J. G. Georgiadis, and C. L. Johnson, "Observation of direction-dependent mechanical properties in the human brain with multi-excitation MR elastography," *Journal of the Mechanical Behavior of Biomedical Materials*, vol. 59, pp. 538–546, June 2016.

[123] K. Hua, J. Zhang, S. Wakana, H. Jiang, X. Li, D. S. Reich, P. A. Calabresi, J. J. Pekar, P. C. M. van Zijl, and S. Mori, "Tract probability maps in stereotaxic spaces: Analyses of white matter anatomy and tract-specific quantification," *NeuroImage*, vol. 39, no. 1, pp. 336–347, Jan. 2008.

[124] K. B. Arbogast and S. S. Margulies, "Material characterization of the brainstem from oscillatory shear tests," *Journal of Biomechanics*, vol. 31, no. 9, pp. 801–807, Sep. 1998.

[125] M. Hrapko, J. A. W. van Dommelen, G. W. M. Peters, and J. S. H. M. Wismans, "Characterisation of the mechanical behaviour of brain tissue in compression and shear," *Biorheology*, vol. 45, no. 6, pp. 663–676, 2008.

[126] J. Steffener, C. Habeck, D. O'Shea, Q. Razlighi, L. Bherer, and Y. Stern, "Differences between chronological and brain age are related to education and self-reported physical activity," *Neurobiology of Aging*, vol. 40, no. C, pp. 138–144, Apr. 2016.

[127] M. C. Murphy, J. Huston 3rd, and R. L. Ehman, "MR elastography of the brain and its application in neurological diseases." *NeuroImage*, Oct. 2017.

[128] R. Miller, A. Kolipaka, M. P. Nash, and A. A. Young, "Identification of Transversely Isotropic Properties from Magnetic Resonance Elastography Using the Optimised Virtual Fields Method," in *Functional Imaging and Modelling of the Heart*. Cham: Springer International Publishing, May 2017, pp. 421–431.

[129] E. H. Clayton, J. R. Garbow, and P. V. Bayly, "Frequency-dependent viscoelastic parameters of mouse brain tissue estimated by MR elastography," *Physics in Medicine and Biology*, vol. 56, no. 8, pp. 2391–2406, 2011.

[130] J. L. Schmidt, "Characterizing Anisotropy in Fibrous Soft Materials by MR Elastography of Slow and Fast Shear Waves," Ph.D. dissertation, ProQuest Dissertations and Theses, 2017.

[131] K. Schregel, N. Nazari, M. O. Nowicki, M. Palotai, S. E. Lawler, R. Sinkus, P. E. Barbone, and S. Patz, "Characterization of glioblastoma in an orthotopic mouse model with magnetic resonance elastography," *NMR in Biomedicine*, pp. 1–11, Jan. 2017.

[132] P. Kennedy, M. Wagner, L. Castéra, C. W. Hong, C. L. Johnson, C. B. Sirlin, and B. Taouli, "Quantitative Elastography Methods in Liver Disease: Current Evidence and Future Directions," *Radiology*, vol. 286, no. 3, pp. 738–763, Mar. 2018.

[133] J. D. Hughes, N. Fattahi, J. Van Gompel, A. Arani, F. Meyer, G. Lanzino, M. J. Link, R. Ehman, and J. Huston 3rd, "Higher-Resolution Magnetic Resonance Elastography in Meningiomas to Determine Intratumoral Consistency," *Neurosurgery*, vol. 77, no. 4, pp. 653–659, Oct. 2015.

[134] N. Sakai, Y. Takehara, S. Yamashita, N. Ohishi, H. Kawaji, T. Sameshima, S. Baba, H. Sakahara, and H. Namba, "Shear Stiffness of 4 Common Intracranial Tumors Measured Using MR Elastography: Comparison with Intraoperative Consistency Grading," *American Journal of Neuroradiology*, vol. 37, no. 10, pp. 1851–1859, Oct. 2016.

[135] B. M. Sandroff, G. R. Wylie, B. P. Sutton, C. L. Johnson, J. DeLuca, and R. W. Motl, "Treadmill walking exercise training and brain function in multiple sclerosis: Preliminary evidence setting the stage for a network-based approach to rehabilitation," *Multiple Sclerosis Journal - Experimental, Translational and Clinical*, vol. 4, no. 1, pp. 1–5, 2018.

[136] D. F. Moore, A. Jérusalem, M. Nyein, L. Noels, M. S. Jaffee, and R. A. Radovitzky, "Computational biology — Modeling of primary blast effects on the central nervous system," *NeuroImage*, vol. 47, pp. T10–T20, Aug. 2009.

[137] A. Romano, W. Szymczak, Z. Yin, and J. Huston III, "Mild Traumatic Brain Injury Studies using Magnetic Resonance Elastography, Diffusion Tensor Imaging, and MIxed Isotropic and Anisotropic Inversions on a Compact 3T Scanner," in *NCA TBI Research Symposium*, Bethesda, Mar. 2017.

[138] J. D. Hughes, N. Fattahi, J. Van Gompel, A. Arani, R. Ehman, and J. Huston 3rd, "Magnetic resonance elastography detects tumoral consistency in pituitary macroadenomas," *Pituitary*, vol. 19, no. 3, pp. 286–292, Jan. 2016.

[139] L. Jugé, A. C. Pong, A. Bongers, R. Sinkus, L. E. Bilston, and S. Cheng, "Changes in Rat Brain Tissue Microstructure and Stiffness during the Development of Experimental Obstructive Hydrocephalus," *PLoS ONE*, vol. 11, no. 2, pp. 1–24, Feb. 2016.

[140] S. F. Othman, H. H. Xu, T. J. Royston, and R. L. Magin, "Microscopic magnetic resonance elastography (mu MRE)," *Magnetic Resonance in Medicine*, vol. 54, no. 3, pp. 605–615, Sep. 2005.

[141] S. F. Othman, E. T. Curtis, S. A. Plautz, A. K. Pannier, S. D. Butler, and H. Xu, "MR elastography monitoring of tissue-engineered constructs." *NMR in Biomedicine*, vol. 25, no. 3, pp. 452–463, Mar. 2012.

[142] S. F. Othman, H. Xu, and J. J. Mao, "Future role of MR elastography in tissue engineering and regenerative medicine," *Journal of Tissue Engineering and Regenerative Medicine*, vol. 9, no. 5, pp. 481–487, Aug. 2013.

[143] M. Destrade, M. D. Gilchrist, J. G. Murphy, B. Rashid, and G. Saccomandi, "Extreme softness of brain matter in simple shear," *International Journal of Non-Linear Mechanics*, vol. 75, no. C, pp. 54–58, Oct. 2015.

[144] Z. Yin, K. J. Glaser, A. Manduca, J. J. Van Gompel, M. J. Link, J. D. Hughes, A. Romano, R. L. Ehman, and J. Huston 3rd, "Slip Interface Imaging Predicts Tumor-Brain Adhesion in Vestibular Schwannomas," *Radiology*, vol. 277, no. 2, pp. 507–517, Nov. 2015.

[145] R. J. Okamoto, E. H. Clayton, and P. V. Bayly, "Viscoelastic properties of soft gels: comparison of magnetic resonance elastography and dynamic shear testing in the shear wave regime," *Physics in Medicine and Biology*, vol. 56, no. 19, pp. 6379–6400, Sep. 2011.

[146] D. S. Berry, "Stress Propagation in Visco-Elastic Bodies," *Journal of the Mechanics and Physics of Solids*, vol. 6, no. 3, pp. 177–185, 1958.